THE APPLICATION OF STIMULUS RESPONSE TECHNIQUES TO THE MODELLING OF HIGH INTENSITY SPRAY COMBUSTION CHAMBERS

Errata

page	
40	line 11; delete 'as' at end of line
54	line 18; instead of 'provision for allowing' read 'allowance has been made'.
60	equation 4.25; for '$\overline{D}_{31}$' in denominator read '$\overline{D}_{31}{}^{2}$'.
61	units of $\overline{D}_{31}$ are μm.
62	line 8; for 'forms' read 'terms'.
66	section 4.6 (i) insert ϕ before = sign.
67	section 4.6.2: line 3; change 'K' to 'κ'
83	line 1; delete 'drop size'.
89	sixth line from bottom; delete "that".
133	line 14; for 'great' read 'greater'.
146	line 9; for '2.31' read '2.3b'.
157	paragraph 3, line 3; for 'value' read 'valve'

THE APPLICATION OF STIMULUS RESPONSE TECHNIQUES TO THE MODELLING OF HIGH INTENSITY SPRAY COMBUSTION CHAMBERS

by

Nathan Munz B.E.(Monash), M.Sc.(Technion)

A thesis submitted for the degree of Doctor of Philosophy of the University of London and for the Diploma of Imperial College

Department of Chemical Engineering
and Chemical Technology,
Imperial College,
London, S.W.7.

November, 1975.

TO

MIRIAM

A woman of valour who can find
For her worth is far above rubies ...

Proverbs xxxi. 10

אשת חיל מי ימצא
ורחק מפנינים מכרה...

משלי לייא.יי

ABSTRACT

The aim of this work is to demonstrate how stimulus response techniques may be used to identify the reactor flow configuration of high intensity spray combustion chambers, and to show how such configurations, when combined with models of spray combustion in stirred and plug flow reactor elements, are used to predict combustion performance. The performance parameters predicted are efficiency, temperature, product composition, including nitrogen oxides and stability.

A novel dynamic sampling technique is developed and used to measure accurately the residence time distribution of a 100 kW high intensity spray combustion chamber for a number of operating conditions. The results are used to identify a flow configuration of stirred and plug flow reactor elements, each of which corresponds functionally with a specific part of the chamber.

A model is developed for the evaporation and combustion of a polysize fuel spray in stirred and plug flow reactor elements. The model assumes that the rate of spray evaporation controls the fuel available for homogeneous pyrolysis and subsequent reaction. Pyrolysis of the evaporated fuel to carbon monoxide and hydrogen is assumed to be instantaneous and the subsequent reactions are modelled by a 22 step kinetic mechanism. Predictions of efficiency, temperature, product composition and stability are presented as a function of mean residence time, equivalence ratio and inlet temperature for a stirred reactor burning gas oil spray.

Combination of the derived flow configuration with the combustion model leads to prediction of the above parameters for the chamber, together with a detailed knowledge of the significant factors which determine performance. Predicted trends of nitrogen oxide emissions with variations in overall equivalence ratio and inlet air distribution agree with those measured. These trends are shown by the model to be accounted for by the equivalence ratios and residence times of the reactor elements, as determined by the chamber aerodynamics and feed distribution.

As a result of this work, the application of a systems engineering approach to combustion chamber modelling in terms of design parameters has been considerably advanced.

LIST OF CONTENTS

LIST OF FIGURES

List of Tables

ACKNOWLEDGEMENTS

It is a privilege to have worked under the stimulating supervision of Dr. Paul Eisenklam; his ability to enthuse brings the best out of his students. He has made the period of this work both rewarding and memorable.

Acknowledgement is made of informal discussions with Mr. Brian Fine, one of which led to the concept of dynamic sampling; also to Professor D.T. Pratt of Washington State University for advice on implementation of his chemical kinetics computer program.

The continued support and co-operation of the academic, technical and administrative staff of the Department in which this work was carried out has been invaluable; the names are too many to list, but mention must be made of the contributions of Mr. W. Geal of the Workshop and Mr. R. Wood of the Electronics Section for their respective contributions to mechanical and electronic aspects of the design and construction of the sampling valve. Thanks are also extended to my colleagues C.E. Davies and D. Rodriguez who assisted in the preparations for and execution of the experimental work on the pilot plant combustion system.

Financial assistance with College fees at different stages of this work from the Anglo-Jewish Association, The Bernard J. Lustig Memorial Scholarship and The Old Centralians Trust is gratefully acknowledged.

Last but not least is the support and encouragement received from my family, especially my wife. I hope to prove worthy of their patience and understanding.

NOTATION

Symbol	Significance	Units
A	parameter of reaction rate constant equation	
b	parameter of spray drop size distribution	m^{-2}
B_1, B_2, B_3	ratio of mean residence times	
B_{ev}	transfer number for evaporation $= \frac{\overline{C}_p (T_g - T_\ell)}{L_f}$	
c_{in}	concentration of inlet pulse	mol/m^3
c_{out}	concentration of outlet pulse	mol/m^3
c_m	concentration of outlet pulse as indicated by dynamic measurement	mol/m^3
$\overline{C}_p$	mean specific heat at constant pressure	J/kg K
C_1, C_2, C_3	ratio of mean residence times	
CSTR	continuous stirred tank reactor	
D	drop diameter	m
$\overline{D}$	dimensionless drop diameter ($= D/D^*$)	
$\overline{D}_{31}$	mean evaporative diameter (defined in equation 4.17)	m
D^*	reference diameter	m
E	activation energy	J/kg K
F_1, F_2, F_3	ratio of mean residence times	
g(t)	system time domain response to an impulse input	mol/m^3
G	number size distribution function	m^{-1}
$\overline{G}$	dimensionless number size distribution function ($= D^*G$)	
G(s)	system transfer function	
$G'_\ell(s)$	transfer function of ℓ CSTRs in series	
$G_m(s)$	transfer function of measurement system	
k	reaction rate constant	$m^3/mol\ s$
ℓ	number of CSTRs in series	
L	Laplace transform (operator)	s
L_f	latent heat of vaporisation	J/mol
Le	Lewis number (= thermal diffusivity/molecular diffusivity)	

LTI	Laplace transformed input	
LTI_{eff}	effective LTI	
LTO	Laplace transformed output	
LTO_m	Laplace transform of measured output	
m	total mass of fluid in a reactor	kg
$\dot{m}$	mass throughput of a reactor	kg/s
M	any molecule acting as a gas phase catalyst in three body reactions	
n	parameter of spray number size distribution function given in equation 3.4	
N	number of drops per mass of fluid in a reactor	kg^{-1}
$\overline{N}$	fractional number of drops whose diameter is less than or equal to D	
N_0	number of drops per mass of fluid in the feed stream	kg^{-1}
N_k	parameter of reaction rate constant equation	
PFR	plug flow reactor	
R	recycle ratio	
R_u	universal gas constant	J/mol K
s	Laplace transform parameter	s^{-1}
s_0	mixing parameter in segregated reactor model	
Sens	sensitivity of Laplace transform to error in pulse spread measurement as defined in equation 2.11	
t	time	s
t_i	injection period	s
t_{sd}	sampling delay time	s
t_p	pulse spread ($= 2\overline{t}_p$)	s
$\overline{t}_p$	mean time of a pulse ($= \int_0^\infty ctdt / \int_0^\infty cdt$)	s
$t_{p,eff}$	effective pulse spread	s
T	temperature	K
T_ℓ	liquid temperature	K
T_g	gas temperature	K
V	reactor volume	m^3
w	parameter of reactor flow configuration, indicating fraction of flow through parallel sections	

Y	parameter of equation 3.5	
Δ	increment of symbol appearing immediately following	
ε	evaporative efficiency = fraction of spray volume evaporated	
ε_0	reference ε	
ε_{cum}	cumulative ε, fraction of total spray volume so far evaporated	
ε_{rel}	relative efficiency = $\varepsilon/\varepsilon_0$	
η	fuel conversion efficiency	
η_I	η at ignition	
η_B	η at extinction	
θ	dimensionless temperature (= $R_u T/E$)	
θ_0	θ of feed	
$\theta_{0,I}$	θ_0 for ignition	
$\theta_{0,B}$	θ_0 for extinction	
κ	drop evaporation constant	m^2/s
$\bar{\lambda}$	mean thermal conductivity	W/m K
ρ_ℓ	density of liquid	kg/m^3
τ	mean residence time	s
$\tau_A, \tau_B, \tau_C, \tau_D$	mean residence time of reactors A, B, C, D	s
τ_{ABC}	mean residence time of configuration of reactors A, B and C	s
ϕ	equivalence ratio = $\dfrac{(\text{fuel/air})_{\text{actual}}}{(\text{fuel/air})_{\text{stoichiometric}}}$	

CHAPTER 1: INTRODUCTION

For many applications, high intensity combustion chambers offer significant advantages over traditional chambers (furnaces), in which the combustion process usually occupies a small fraction of the volume. The increased volumetric heat release rate in high intensity combustion allows a reduction in size (and capital cost) of a chamber designed for a given duty.

Other advantages of suitably designed high intensity chambers include:-

(a) The ability to exercise close control over the combustion process. This allows such chambers to be used not only as a means of burning fuels to supply heat, but also as chemical reactors per se to convert (fuel) reactants to specific products as dictated by process requirements. For example a chamber may be designed to burn liquid and/or gaseous fuels to one or more of the following specifications:-

(i) Complete combustion at overall stoichiometric or reducing conditions.

(ii) Controlled distribution of combustion products including pollutants.

(iii) Very high or very low flame radiation.

(iv) Complete product freedom from soot.

(b) The possibility of producing a high velocity exit stream, which may be used to enhance convective heat transfer rates in process heating or to convey the products to a desired location.

(c) The capability of working against unusually high or fluctuating back pressures.

(d) The rapid response to changes in load, fuel type or other process requirements due to small thermal inertia relative to output.

(e) Stable combustion over a wide range of firing rates (i.e. good turndown capability).

High intensity spray combustion of low grade liquid fuels (such as residual fuel oil) is of particular importance due to their availability and competitive price. The close control of combustion allows such fuels to be efficiently burnt at stoichiometric or fuel rich conditions, with reduced formation or elimination of corrosive sulfur and/or vanadium oxides, and low soot emission. Accordingly, these

fuels may be partially burnt at fuel rich conditions (gasified) to produce a combustible gas for process use.

R.P. Fraser (1) has described the characteristics and applications of various high intensity combustion chamber designs, and discussed the factors which determine combustion intensity. For spray systems, the combustion intensity is determined by three main factors: the evaporation rate of the spray, the rate of mixing of fuel vapour with oxidant, and the rate of chemical reaction.

In general the factor which limits combustion intensity and to which particular attention is given in the design of high intensity chambers is mixing rate. The additional price paid for the advantages of such chambers is therefore mainly in the requirement to supply mixing energy, either in the form of high velocity air jets or pressure loss due to baffles or flame holders.

The use of high velocity air jets to induce mixing may be combined with their geometrical disposition in a manner designed to produce a chamber flow configuration conducive to efficient and stable combustion at high throughputs. Furthermore, the flow configuration and the distribution of local reactant concentrations and mixing rates may be designed to achieve reaction rates, product compositions and pollutant emission levels dictated by rigorous process requirements.

In the present work, the modelling of high intensity spray combustion chambers in terms of a combination of basic chemical reactor elements is undertaken to ascertain how different factors affect the combustion process, with a view to predicting design and operating parameters which will achieve optimum performance.

The derivation of reactor element flow configuration from experimental stimulus response experiments by model identification in the Laplace domain is described. A new approach to the estimation of the effects of errors in pulse shape measurement on the accuracy of transfer functions is presented. This approach allows calculation of criteria for input pulse duration that minimise transfer function sensitivity to errors in input pulse shape measurement or that make such measurement completely unnecessary. Furthermore, the application of the sensitivity concept to estimation of the reliability of parameters of a flow model is demonstrated.

A model for combustion of a polysize spray in stirred and plug flow reactors was developed, based on those physical and chemical processes which are important

in a high intensity combustion environment. In particular, the model assumed that the spray evaporation rate in the reactor limited the rate of fuel addition for the subsequent homogeneous chemical reactions.

The mass and energy balances for a perfectly stirred reactor burning vaporised fuel in air were solved to predict the temperature, spray evaporation efficiency, product composition (including pollutants) and combustion stability as a function of reactor mean residence time and equivalence ratio. The reaction was modelled as instantaneous fuel pyrolysis to carbon monoxide and hydrogen, followed by a 22 step kinetic mechanism, which accounts for the subsequent combustion of the pyrolysis products and also for the formation of nitrogen oxide pollutants by a number of routes.

To model a chamber in terms of basic reactor elements, it is necessary to know the reactor flow configuration. A novel experimental method which allows accurate determination of residence time distribution in high intensity chambers under operating conditions was developed. This method was used to carry out stimulus response experiments on a chamber rated at 10 MW/m^3, burning gas oil spray in air at various equivalence ratios and secondary air feed distributions. The results of these experiments were used to identify the reactor flow configuration in each case, from feasible alternatives related to the aerodynamics of the chamber.

Those configurations indicating stable combustion consisted of two stirred tanks (CSTRs) in series with plug flow bypass of the first, followed by another plug flow element. The physical interpretation is based on the great influence of the high fuel spray momentum on the chamber aerodynamics. In the forward half of the chamber the high momentum fuel spray is represented by the plug flow bypass element, with a CSTR corresponding to recirculation in the atomiser region. By the downstream half of the chamber, most of the fuel spray momentum has been dissipated, and recirculation is predominant, being represented by the second CSTR. The tubular exit portion of the chamber is represented by a second plug flow reactor element.

The spray combustion model was used (for the configurations derived for each experimental condition) to estimate the temperature, efficiency and composition for each reactor element, and for the chamber exit stream.

The criterion used for evaluation of the model was agreement between predicted and measured nitric oxide emissions. The reason for this choice is the strong

dependence of these emissions on the temperature/composition/time history of the combustion gases. This complex dependence provides a single criterion which is related to the main features of both the aerodynamics and the combustion processes, so that if it is satisfied in a number of cases it would indicate overall adequacy of the model.

Agreement was obtained between predicted and measured trends of nitric oxide emissions with variations in overall equivalence ratio and secondary air feed distribution. Furthermore, these trends were accounted for in terms of the equivalence ratios and residence times of the reactor elements of the flow configuration, as determined by the chamber geometry and aerodynamics. The model showed that a change in the air feed distribution does not bring about a change in the configuration of reactor elements, but only in the characteristics of these elements such as equivalence ratio, temperature, etc. This concurs with the expectation that the chamber aerodynamics is largely determined by the fuel spray momentum, with only minor modifications being induced by changes in the relatively low momentum secondary air jets.

In addition to the above elucidation of chamber characteristics, the model predicted absolute values of nitric oxide emissions within a factor of about two, a result which is very gratifying in this type of investigation. Possible reasons were given for this consistent overestimation, and these might be considered further with a view to modifying the model to allow it to be used for quantitative prediction.

It should be pointed out here that the flow configuration derived for some conditions incorrectly predicted instability. It is felt that only a further sophistication of the identification technique, possibly involving stimulus response experiments on the secondary air streams, would extend application of the model to a wider range of conditions.

CHAPTER 2: FLOW MODEL IDENTIFICATION

The dynamic response of physical systems has been widely used for the identification of system characteristics. These characteristics may be used directly in the design of controllers to modify undesirable system behaviour resulting from disturbances in inputs or operating conditions and, in addition, to identify the basic components of a system and how they are combined. Model identification is the science of selecting a model for a system on the basis of its dynamic response as determined by experimental stimulus response techniques. These techniques involve measurement of the system response to a known or measured stimulus. A comprehensive review of process identification and parameter estimation techniques was published by Nieman et al. (2).

This chapter will discuss the identification of the flow configuration of chemical reactors in terms of a configuration of stirred and plug flow reactor elements. The flow characteristics of a particular reactor defines the residence time distribution (RTD, see below), which may be used to determine the reactor performance, either directly, or through an appropriate model identified on the basis of the measured RTD.

Various methods are available for deriving the reactor flow configuration from stimulus response experimental data. These are referred to as methods of system identification and are based on comparing the characteristics of input/output experimental results with those of theoretical models.

These comparisons may be carried out in the time domain by comparing the experimental output with that which would be obtained from various models. Alternatively, Laplace domain (transfer function) and Fourier domain analysis have been used extensively, each having particular advantages for certain types of system identification problems. Examples of the application of these methods and comparison of their relative merits for specific applications have been given by Anderssen and White (3), Michelsen and Østergaard (4) and Johnson et al. (5).

Laplace domain systems identification was selected to derive the reactor configuration of the combustion chamber. It was not only the simplest to use in view of the non-ideal pulse input, but it was also suitable to discriminate between the various feasible models.

2.1: Residence Time Distribution from Stimulus Response Experiments

The use of stimulus response experiments to determine residence time distribution (RTD) in a vessel was first proposed by Danckwerts (6) and has since become a standard tool of process analysis.

The technique is discussed at length in the chemical engineering literature; its basis and general application have been adequately described by Danckwerts (6) and Levenspiel (7). The details covered here will be restricted to aspects of the technique specifically related to its application to combustion systems.

Three types of input are most commonly used as a stimulus, viz. pulse, step and sinusoidal. It was decided that a pulse input is preferable to the others for the following reasons:

(i) Sinusoidal and step input experiments use excessive amounts of tracer, especially in view of the number of tests required by the sampling technique used. (See chapter 6).

(ii) Sinusoidal inputs require a relatively complex system for their generation.

(iii) For the calculation of transfer functions (see section 2.2) the pulse response is required. For step input experiments this may be obtained by differentiation of the experimental results, which is an inherently inaccurate procedure.

A novel experimental method for accurately carrying out pulse input stimulus response tests on combustion chambers is described in chapter 6.

The following sections show how Laplace transformed stimulus response experimental results are used to derive reactor flow configurations.

2.2: Laplace Transformation of Input/Output Data to Obtain System Transfer Function

The response of a system to an input is a function of both the input and the system characteristics, hence the use of stimulus response experiments for the purposes of system identification. The following analysis of system identification in the Laplace domain applies to linear systems only.

In the time domain, an input to a system, $c_{in}(t)$, will result in an output, $c_{out}(t)$, which are related by the convolution integral,

$$c_{out}(t) = \int_0^t g(t - t').c_{in}(t')dt' \qquad (2.1)$$

where g(t) represents the system characteristics in the time domain, and may be interpreted as either the inverse Laplace transform of G(s) (see below), or the system time domain response to an impulse input.

t = time

t' = a dummy time variable.

In the Laplace domain, the input (LTI) is the Laplace transform of $c_{in}(t)$ and the output (LTO) is the Laplace transform of $c_{out}(t)$, given by, respectively

$$LTI = \int_0^\infty c_{in}(t).\exp(-st)dt \qquad (2.2)$$

and

$$LTO = \int_0^\infty c_{out}(t).\exp(-st)dt \qquad (2.3)$$

where s = Laplace transform parameter and these are related to one another by

$$G(s) = \frac{LTO}{LTI} \qquad (2.4)$$

where G(s) is the transfer function of the system and represents the system characteristics in the Laplace (or 's') domain. The relationships between the above inputs, outputs and describing (or characteristic) functions are illustrated in figure 2.1.

Equation 2.4 is the definition of the transfer function, and together with the two previous equations, is used to calculate G(s) from input/output experimental data.

2.3: Examples of Transfer Functions for Reactor Element Configurations

A number of configurations using continuous stirred and plug flow reactors (CSTR and PFR's) as basic elements are described, and the method of calculating the transfer function of such configurations demonstrated.

The transfer functions of the basic elements are

$$G_{CSTR}(s) = \frac{1}{\tau s + 1} \qquad (2.5)$$

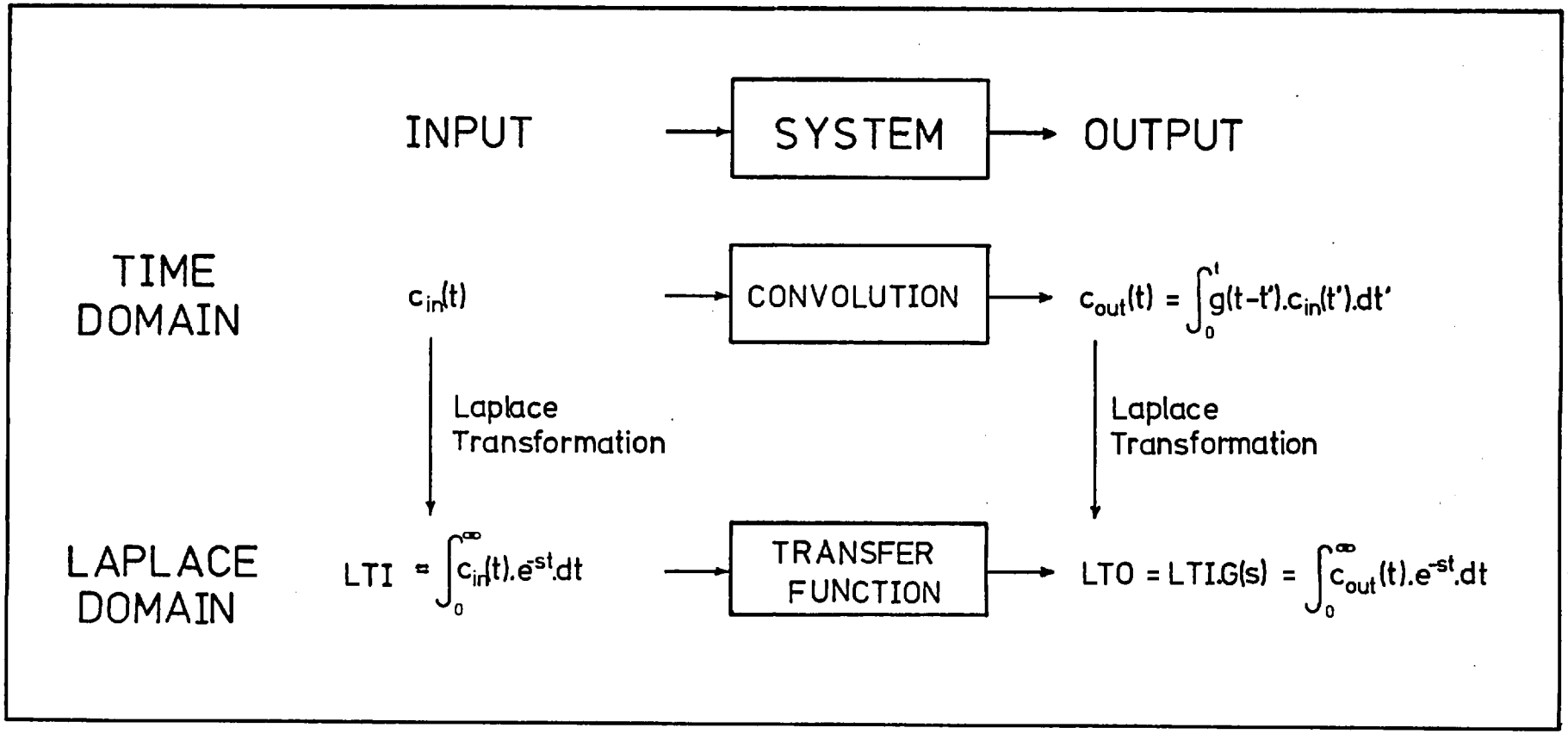

FIGURE 2.1 Relationship between system input and output in the time and Laplace domains.

and $$G_{PFR}(s) = \exp(-\tau s) \tag{2.6}$$

where τ = mean residence time of the reactor element.

The transfer functions of combinations of the basic reactor elements are calculated using simple rules arising directly from the properties of the Laplace transform of linear systems. These rules are shown in figure 2.2. The transfer function of a reactor configuration will be expressed as a function of τs, where τ is the mean residence time of the reactor configuration.

The transfer function for the first two configurations shown in figure 2.3 are calculated in Appendix A by way of example. The result for each is as follows:

(a) Two CSTR's in recycle (figure 2.3(a))

$$G_1(s) = \frac{\tau_B s + 1}{(1 + R)(\tau_B s + 1)(\tau_A s + 1) - R} \tag{2.7}$$

or, in terms of τ, the overall mean residence time

$$G_1(s) = \frac{B_1 F_1 \tau s + 1}{(1 + R)(B_1 F_1 \tau s + 1)(F_1 \tau s + 1) - R} \tag{2.8}$$

where $$B_1 = \frac{\tau_B}{\tau_A} \tag{2.8a}$$

$$F_1 = \frac{1}{1 + R(B_1 + 1)} \tag{2.8b}$$

(b) Two CSTR's in series with plug flow bypass of first CSTR. (figure 2.3(b))

$$G_2(s) = [w_2(\frac{1}{F_2 \tau s + 1}) + (1 - w_2)\exp(-B_2 C_2 F_2 \tau s)] . \frac{1}{B_2 F_2 \tau s + 1} \tag{2.9}$$

where $$B_2 = \frac{\tau_B}{\tau_A} \tag{2.9a}$$

$$C_2 = \frac{\tau_C}{\tau_B} \tag{2.9b}$$

w_2 = fraction of flow passing through first CSTR

$$F_2 = \frac{1}{w_2 + (1 - w_2)B_2 C_2 + B_2} \tag{2.9c}$$

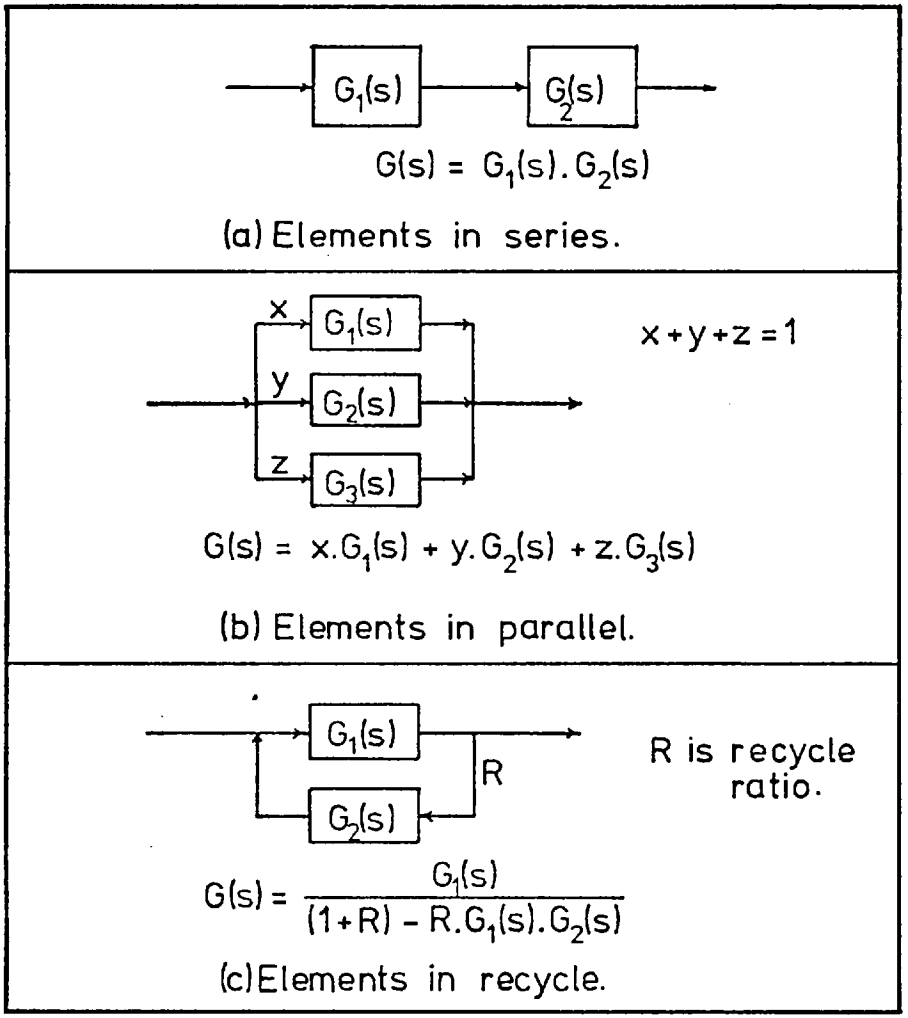

FIGURE 2.2 Rules for calculating the transfer function of simple combinations of reactor elements.

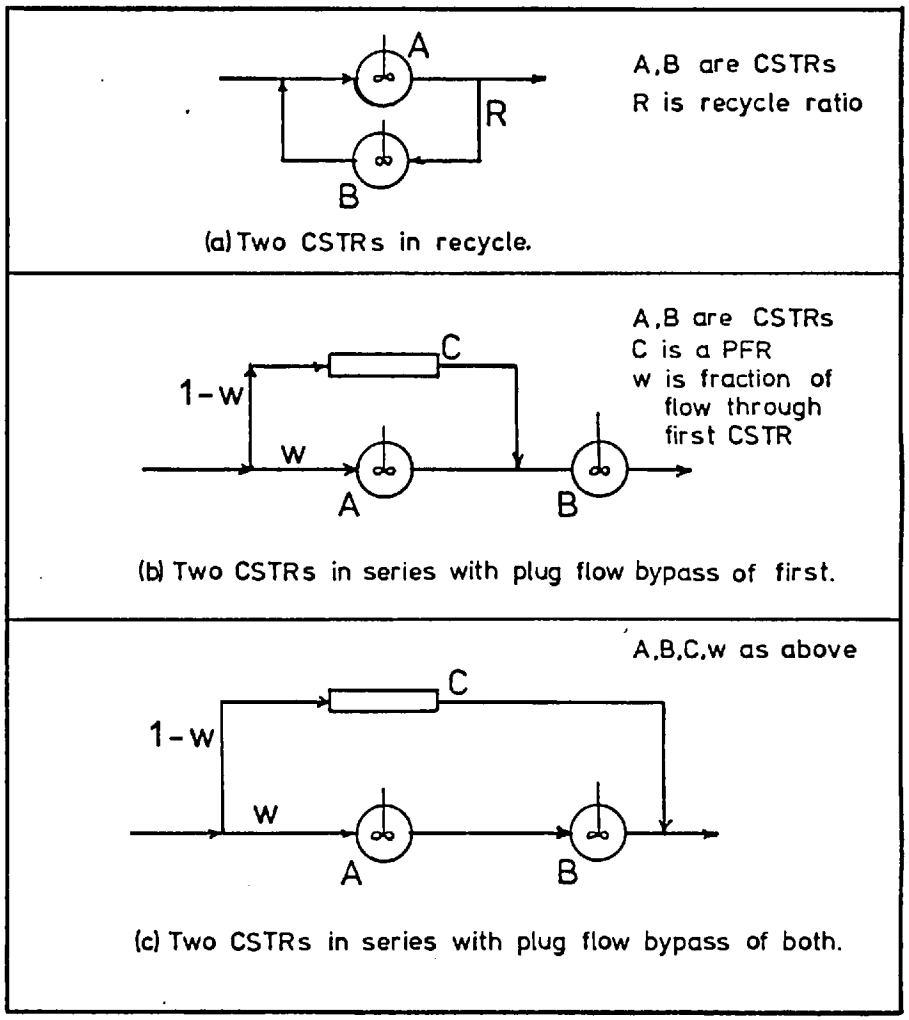

FIGURE 2.3 Examples of reactor element configurations.

(c) Two CSTR's in series with plug flow bypass of both (figure 2.3c)

$$G_3(s) = w_3\left(\frac{1}{F_3\tau s + 1}\right)\left(\frac{1}{B_3F_3\tau s + 1}\right) + (1 - w_3)\exp(-B_3C_3F_3\tau s) \qquad (2.10)$$

where

$$B_3 = \frac{\tau_B}{\tau_A} \qquad (2.10a)$$

$$C_3 = \frac{\tau_C}{\tau_B} \qquad (2.10b)$$

w_3 = fraction of flow through CSTRs

$$F_3 = \frac{1}{w_3(1 + B_3) + (1 - w_3)B_3C_3} \qquad (2.10c)$$

The transfer functions of each of the above reactor configurations are functions of the parameters as well as of the model structure. Graphs of equations 2.9 and 2.10 for a number of combinations of parameters are shown in figures 2.4 and 2.5 respectively. It is worth noting that the value of a transfer function at a single value, or even at two values of τs does not uniquely define the configuration or its parameters as some of the transfer functions may cross at two points.

2.4: Model Discrimination in the Laplace Domain

Once the input/output experimental results have been obtained, G(s) may be calculated from the equations in section 2.2. The experimentally determined transfer function is then compared with the transfer functions of feasible models (calculated as shown in section 2.3). The model whose transfer function is the best fit to the experimental G(s) is then considered to be the best model of the process.

If the feasible models are such that their transfer functions have different values over a range of τs that is suitable for matching (see below), it would be possible to determine the best model by comparing the experimental G(s) with the theoretical at only one value of τs in the range.

The range of τs over which the transfer functions may usefully be compared is limited as follows. As $\tau s \Rightarrow 0$ all transfer functions approach unity, so that for small τs it is difficult to differentiate between those of different models. At large values of τs, s is large (τ is fixed by the system) and the weighting factor of the Laplace transform ($\exp\{-ts\}$) becomes relatively very large at small values of

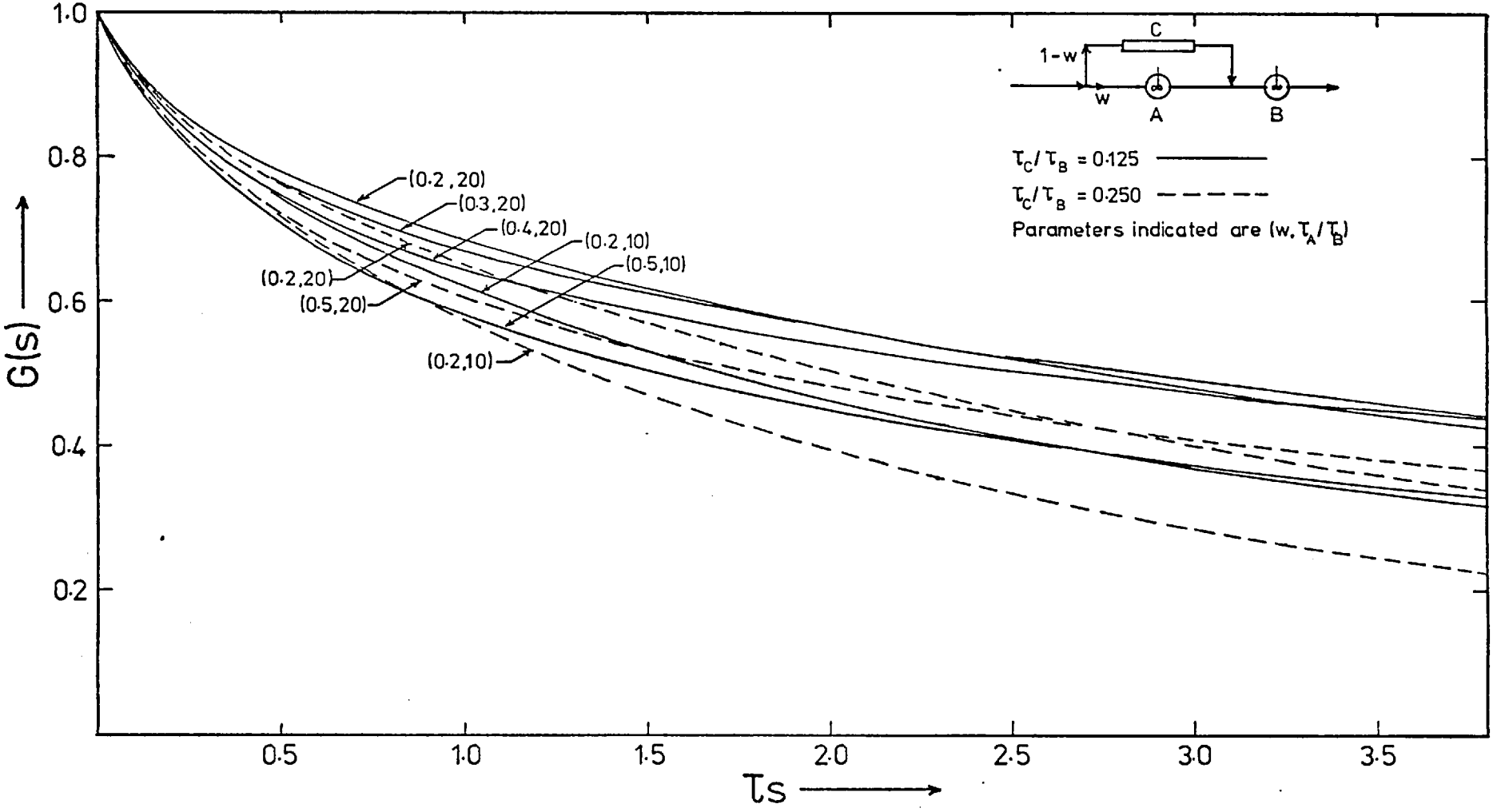

FIGURE 2·4 Transfer function for configuration of figure 2·3(b).

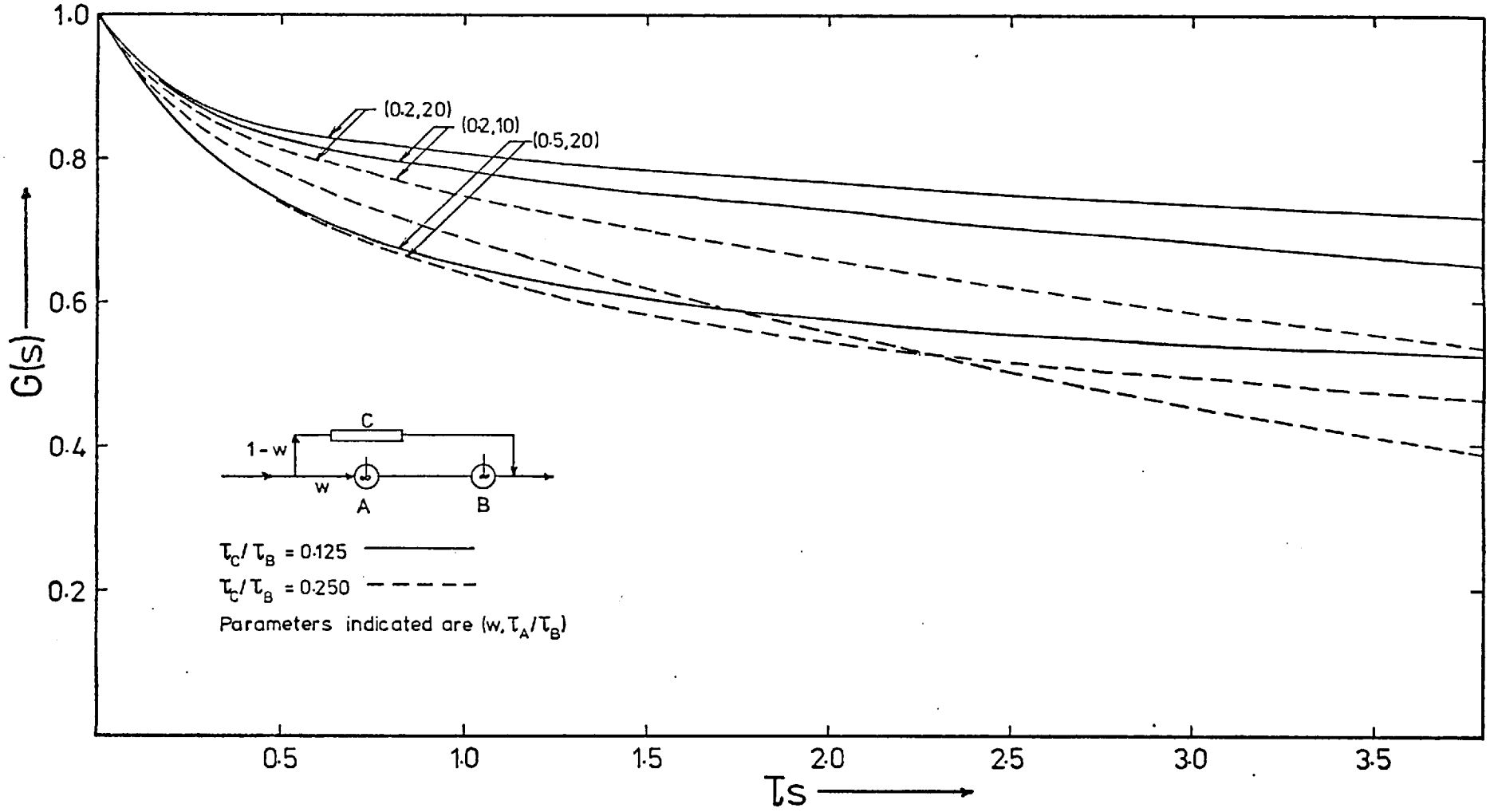

FIGURE 2·5 Transfer function for configuration of figure 2·3(c)

time, so that effectively only the initial part of the response affects the transform. This leads to increased error as only part of the available experimental data is, in effect, being utilized. Consequently, there is an optimum range of τs, dependent on the particular models and experimental system being considered. Hopkins et al (8) give an example of the calculation of the optimum range of τs for a dispersion model of flow through packed beds.

An alternative approach to selection of the best range of τs for discrimination between alternative models is to choose that range over which there is a maximum difference between the transfer functions of the models. An example of this approach is given in Appendix B.

In line with the latter approach, and on inspection of the transfer function curves of the feasible models (for examples see figures 2.4 and 2.5) the range $1.0 < \tau s < 3.0$ was considered optimum. To simplify the matching procedure in view of the number of parameter and model combinations, the best match at three values of τs (τs = 1.0, 2.0 and 3.0) was sought for, rather than carrying out minimization of deviations throughout the range. The combination of three values of τs was found adequate to discriminate between the feasible models.

2.5: The Effect of Pulse Shape and Duration on Accuracy of Model Identification in the Laplace Domain

For the planning and evaluation of stimulus response experiments, it is desirable to know how errors in the measurement of pulse shape affect the transfer function, and whether the shape and duration of the input pulse need to be accurately measured.

The transfer function G(s) was defined in equation 2.4 as

$$G(s) = \frac{LTO}{LTI} \qquad (2.4)$$

so that any effect on G(s) will be transmitted through the Laplace transform of the output and/or input pulses. The sensitivity of the Laplace transform of a pulse to errors in its measurement will therefore be investigated.

The pulse shapes considered are rectangular, half sine, displaced cosine and asymmetrical exponentially decaying as defined in Table 2.1, and are shown in fig. 2.6. The first three pulse shapes were chosen to provide a variety of symmetrical

TABLE 2.1: Equation, Laplace Transform and Sensitivity of Various Pulse Shapes.

PULSE SHAPE	EQUATION OF PULSE $c(t)$	LAPLACE TRANSFORM $L[c(t)] = \int_0^\infty c(t)e^{-st}dt$	SENSITIVITY OF TRANSFORM $\text{Sens} = -\frac{dL}{d(st_p)} \cdot \frac{(st_p)}{L}$
rectangular	$c_r(t) = {}^1/_{t_p}$ $0<t<t_p$ $= 0$ $t\leq 0,\ t\geq t_p$	$L[c_r] = \frac{1-e^{-st_p}}{st_p}$	$\text{Sens}_r = 1 - \frac{st_p.e^{-st_p}}{1-e^{-st_p}}$
half sine	$c_s(t) = \frac{\pi}{2t_p} \sin(\frac{\pi t}{t_p})$ $0<t<t_p$ $= 0$ $t\leq 0,\ t\geq t_p$	$L[c_s] = (\frac{1+e^{-st_p}}{2}).[\frac{1}{1+(st_p/\pi)^2}]$	$\text{Sens}_s = \frac{2.(st_p/\pi)^2}{1+(st_p/\pi)^2} + \frac{st_p.e^{-st_p}}{1+e^{-st_p}}$
displaced cosine	$c_c(t) = \frac{1}{t_p}(1 - \cos[\frac{2\pi t}{t_p}])$ $0<t<t_p$ $= 0$ $t<0,\ t\geq t_p$	$L[c_c] = (\frac{1-e^{-st_p}}{st_p}).\frac{1}{1+(st_p/2\pi)^2}$	$\text{Sens}_c = 1 - \frac{st_p.e^{-st_p}}{1-e^{-st_p}} + \frac{(st_p)^2}{2\pi^2[1+(st_p/2\pi)^2]}$
asymmetrical, exponentially decaying	$c_a(t) = \frac{t}{(t_p/4)^2} \cdot \exp[\frac{-t}{(t_p/4)}]$ $0\leq t<\infty$	$L[c_a] = \frac{1}{\frac{st_p}{4}+1)^2}$	$\text{Sens}_a = \frac{st_p}{2(\frac{st_p}{4}+1)}$

Note: For each pulse shape, $t_p = 2\bar{t}_p = 2\int_0^\infty t.c(t)dt$; $\int_0^\infty c(t)dt = 1$

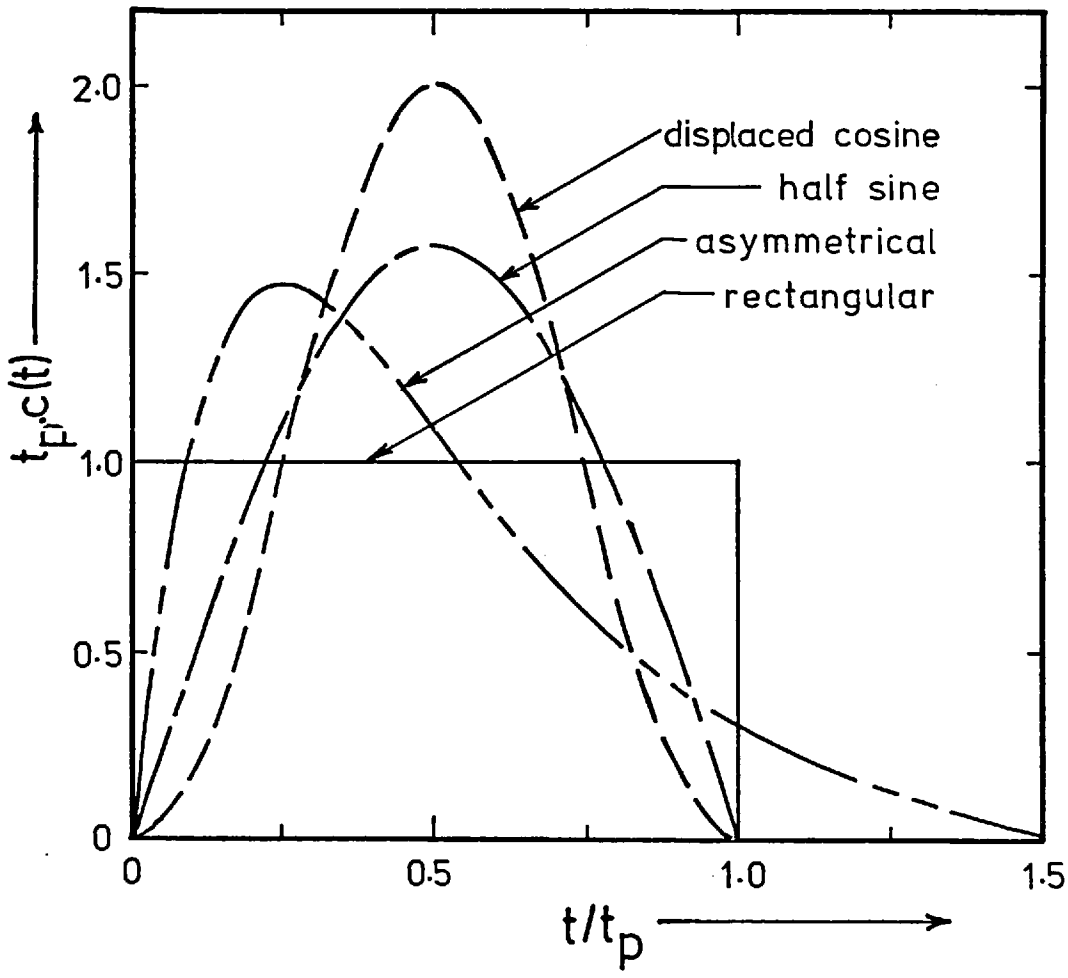

FIGURE 2.6 Pulse shapes considered in error analysis

shapes while the fourth is typical of pulses encountered in practice and differs from the first three in that it is asymmetrical and decays exponentially instead of having a finite duration. Each shape is a function of only one parameter, t_p which is defined as twice the mean time of the pulse, $\bar{t}_p$, and for the first three pulses is equivalent to the duration. t_p will be referred to as the pulse spread.

The Laplace transform of each of these pulses is given in the second column of Table 2.1, in each case being a function of (st_p), the dimensionless product of the Laplace parameter and the pulse spread.

The effect of errors in experimental measurement of a pulse on its Laplace transform may be ascertained by considering (a) the effect of pulse shape on Laplace transform, and (b) the sensitivity of the Laplace transform of a given pulse shape to error in measurement of its spread, t_p.

Figure 2.7 shows the effect of pulse shape on its Laplace transform for a range of st_p. The half-sine shape transform is not shown as its value is between those of the rectangular and displaced cosine for all st_p. This figure shows that for st_p less than about 1.0, there is virtually no difference between the Laplace transforms of the various shapes. For larger values of st_p, the differences become significant, and it becomes necessary to measure the shape accurately; the larger the value of st_p, the more accurately the shape should be measured for a given allowable error.

As the input pulse shape is more difficult to measure (due to its shorter duration), the effect of its duration relative to the system mean residence time on the sensitivity of its Laplace transform will be considered first. The error in measurement of a given pulse shape is effectively the error in its spread, t_p. The effect of errors in measurement of the pulse spread may be expressed as the sensitivity, defined as

$$\text{Sens} = -\frac{\text{(fractional change in L)}}{\text{(fractional error in pulse spread)}} \tag{2.11}$$

for the input pulse,

$$\text{Sens} = -\frac{d(\text{LTI})/\text{LTI}}{d(t_p)/t_p} \tag{2.12}$$

$$= -\frac{d(\text{LTI})/\text{LTI}}{d(st_p)/(st_p)} \tag{2.13}$$

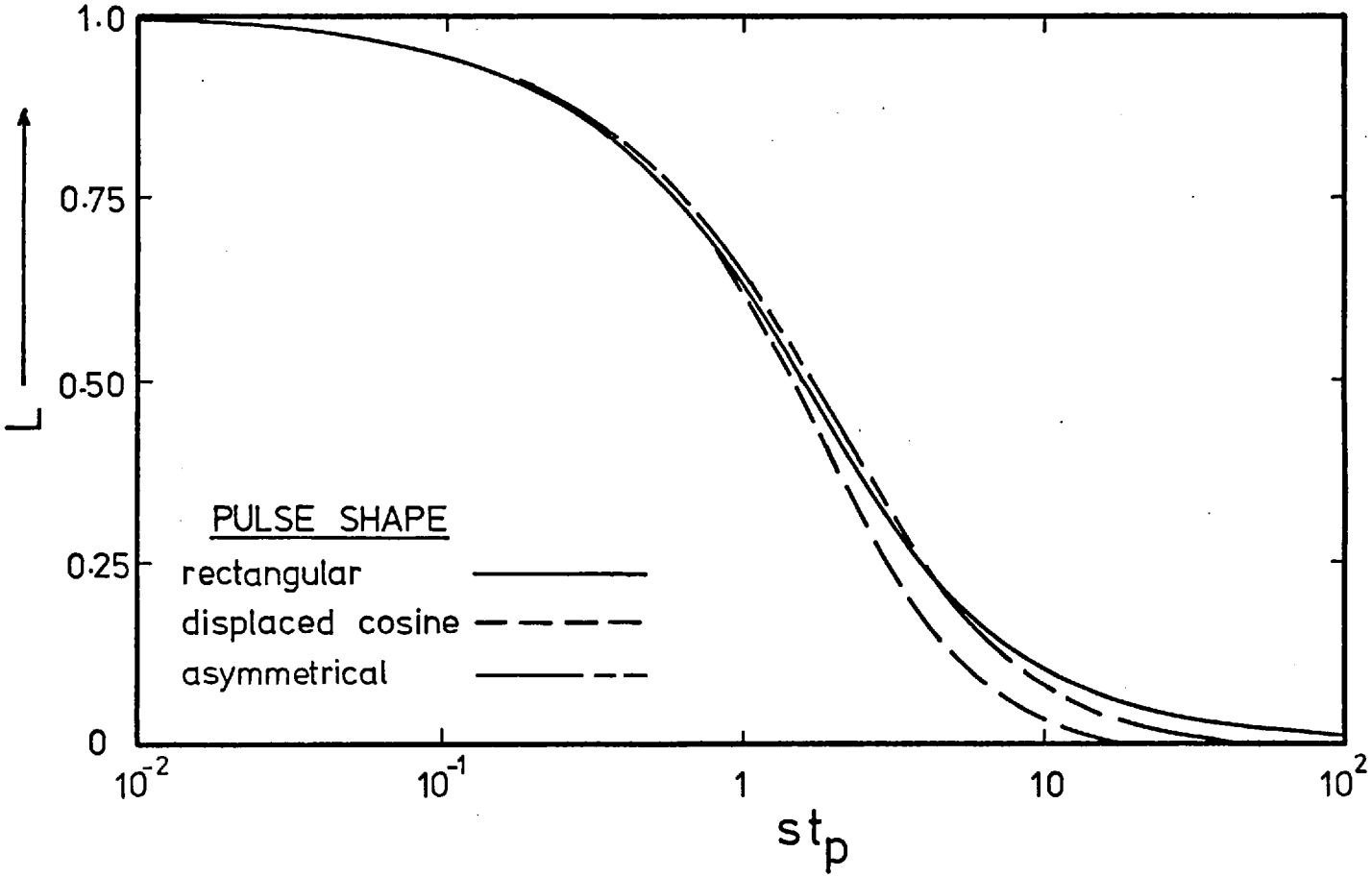

FIGURE 2.7 Laplace transform of pulse shapes.

From figure 2.7 it can be seen that the sensitivity as defined is always positive because an overestimation of st_p results in a lower value of L (and vice versa) for all pulse shapes.

The sensitivity for each pulse shape may be derived directly using equation 2.13 and the appropriate expression for the pulse shape. The resulting relations appear in column 3 of Table 2.1, and these are shown on figure 2.8.

Figure 2.8 indicates that for all pulse shapes the sensitivity is negligible for values of st_p given by

$$st_p \leq 0.1 \tag{2.14}$$

For increasing st_p the sensitivity increases at different rates for each pulse shape until it approaches its respective limiting value. For example, the asymmetrical pulse has a limiting sensitivity of 2.0 for large st_p, which means that at such st_p a 10% error in determination of t_p would lead to a 20% error in the Laplace transform.

In order to minimise the amount of experimental work, it is often assumed that the pulse input used is so short in duration (compared to the residence time of the system being tested), that it may be assumed to be an impulse input, and hence need not be measured. The above analysis allows estimation of the conditions necessary for the accuracy of this assumption, as follows.

In section 2.4 it was concluded that for the identification of a system with a mean residence time of τ, the best value of τs for model discrimination is of the order of

$$\tau s = 2.0 \tag{2.15}$$

so that the value of the Laplace parameter is given by

$$s = \frac{2}{\tau} \tag{2.16}$$

Substituting 2.16 into 2.14

$$\frac{2}{\tau} . t_p \leq 0.1 \tag{2.17}$$

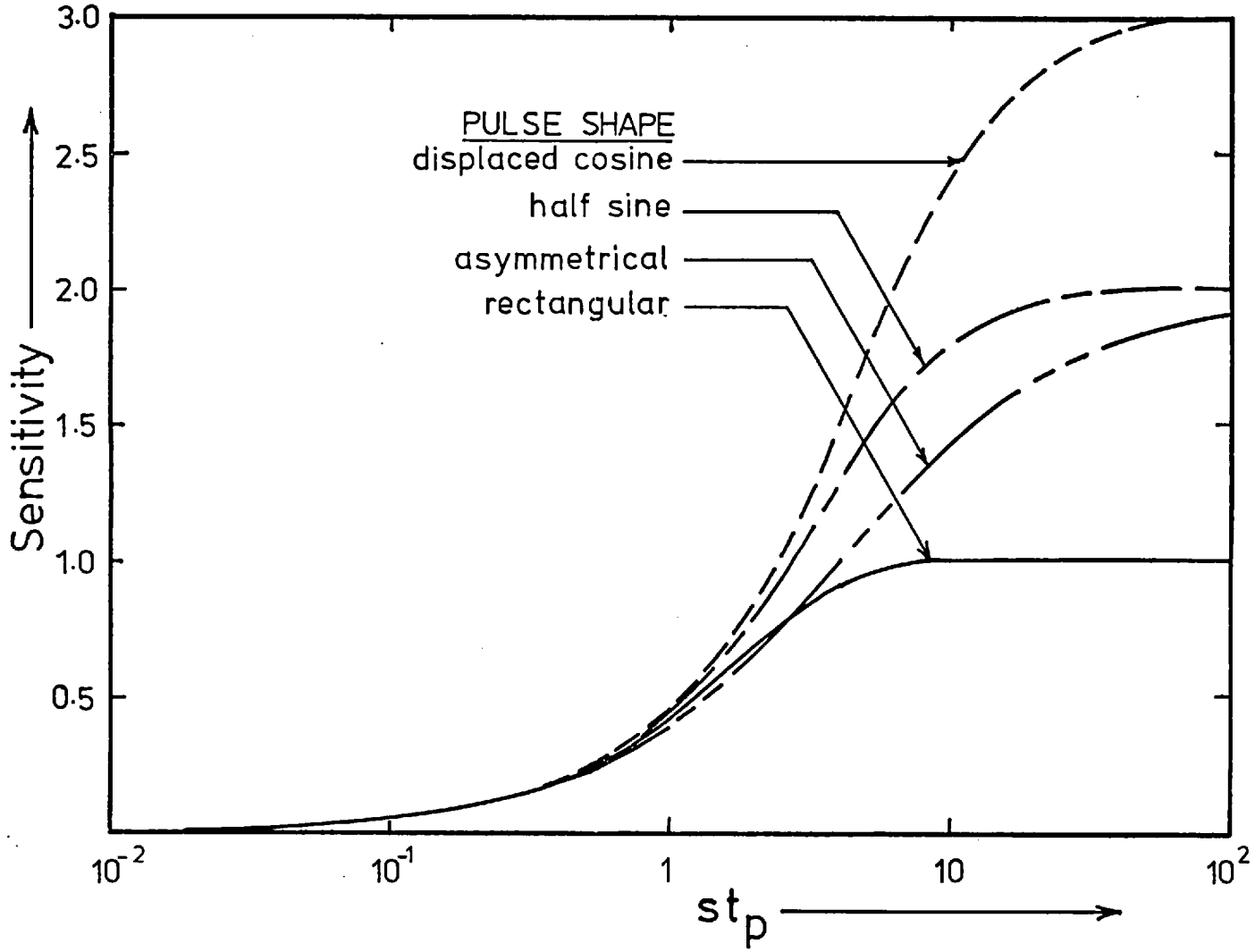

FIGURE 2·8 Sensitivity of Laplace transform for different pulse shapes.

i.e.

$$\frac{t_p}{\tau} \leq 0.05 \tag{2.18}$$

If we define the mean time of the pulse as $\bar{t}_p$,

$$\bar{t}_p = \frac{1}{2} t_p \tag{2.19}$$

equation 2.18 may be expressed in the form

$$\frac{\bar{t}_p}{\tau} \leq 0.025 \tag{2.20}$$

i.e. when the mean time of the pulse is less than about 2.5% that of the system, it is to all intents and purposes an impulse and need not be measured.

The situation may arise in practice that the duration (and approximate mean time) of a pulse input is easily estimated, while its precise shape is difficult to measure. In such cases the LTI may be accurately estimated independently of the shape for values of st_p up to about 1.0 (see fig. 2.7) the sensitivity at this level of st_p being of the order of 0.4 (see figure 2.8) which may be adequate for some purposes, especially when the output pulse can be accurately measured. For these conditions the criterion becomes

$$\frac{\bar{t}_p}{\tau} \leq 0.25 \tag{2.21}$$

The penalty for using high values of st_p is increased sensitivity of the LTI to error in the pulse spread as determined from the experimentally measured shape.

Another observation that may be made relates to the amplification of errors due to large values of s. As mentioned in section 2.4, excessive values of s lead to increased error as this causes only the initial part of the experimental response curve to affect the Laplace transform. The above analysis confirms that for a given pulse duration, the smaller the value of s, the less sensitive the Laplace transform is to experimental errors. The value of s chosen however also has a lower limit as discussed in section 2.4, the optimum value depending on the actual models being considered.

Consideration of the sensitivity of the LTO on the above basis indicates that its sensitivity will always be greater than that of the LTI, as its duration is longer (the value of s chosen is the same). However, as shown in figure 2.8, the sensitivity has a maximum value for a particular shape. The increase in sensitivity to measurement errors should be less than the decrease in the measurement errors due to the greater ease in measuring the longer duration output pulse. The problems of accurately measuring short pulse shapes are discussed at length in section 6.3.

The error in G(s) is obtained from the expected error in both the LTI and LTO as derived from the accuracy of the experimentally measured input and output pulses and the respective sensitivities estimated in the same way as shown above. The estimate of error in the Laplace domain may be used to define, for a given confidence level, a band of values for G(s). This may be interpreted in terms of a fiducial range for one or more model parameters. An example of such an analysis is given in Appendix C.

3. HIGH INTENSITY SPRAY COMBUSTION

This chapter will consider the parameters and processes important in determining the performance of high intensity spray combustion reactors, with a view to describing them adequately for use in a model. Each parameter or process will be discussed in turn, and theoretical and experimental evidence for the description to be used will be presented.

The processes considered (and some of the assumptions made) are those that will allow the model to predict

(i) ε, the evaporative efficiency, defined as the fraction of entering fuel spray which has evaporated

and (ii) the temperature and composition of the reactor products, including nitric oxide pollutants.

3.1: Spray Drop Size Distribution

The drop size distribution of a spray depends on the atomiser type and loading as well as the properties of the fuel, and for twin fluid atomisers the relative amount of secondary atomising fluid. These factors are discussed in detail in the papers of Fraser (9) and Fraser and Eisenklam (10).

Distributions are usually represented by one of a number of empirically developed equations, the best known being (11),

(i) the Nukiyama-Tanasawa equation

(ii) the Rosin-Rammler equation

(iii) the log-normal equation

and (iv) the upper limit equation.

As there is no theoretical basis for preferring any equation, the most convenient form may be chosen provided that it adequately describes the actual drop size distribution.

The equation used to represent the spray in the present analysis is

$$G(D) = \frac{d\bar{N}}{dD} = 2bD \exp(-bD^2) \qquad (3.1)$$

where G = number size distribution function.

$\bar{N}$ = the fractional number of drops whose diameter is less than or equal to D.

D = drop diameter

b = a parameter of the distribution.

This equation will be shown in section 5.3 to adequately describe the spray used.

3.2: Drop Evaporation

The factors affecting drop evaporation rates in a high intensity combustion environment are discussed at length in the reviews of Williams (12, 13) and Hedley et al. (14) and in the report of Faeth et al. (15).

In high intensity combustion chambers the combustion process is homogeneous throughout the active volume with the drops evaporating to provide the fuel vapour for the combustion reaction. This has been borne out by a number of observations which indicate that individual drop combustion with a diffusion flame surrounding each drop does not, in general, take place.

In the experimental work described later it was observed that the flame zone was transparent, not luminous and no soot was measurable in the product stream. Soot formation is believed to be mostly due to diffusion flame burning around drops [Sjogren (16)] or combustion at equivalence ratios greater than 1.4 [Khan (17)], and any subsequent soot combustion is a much slower heterogeneous process than its homogeneous formation.

The fact that no soot is formed would therefore indicate that drops do not support individual diffusion flames.

The other observation supporting the assumption of drop evaporation followed by homogeneous combustion is the relatively low nitric oxide concentrations produced in the chamber (see Chapter 8). Bracco (18) showed that drop supported diffusion flames burn at or near stoichiometric mixture strengths with correspondingly high local temperature and nitric oxide production. Mellor (19, 20) uses similar arguments to explain the effects of heterogeneous processes on emissions from gas turbines.

The following assumptions relating to drop evaporation rates in a high intensity chamber will be applied in the current analysis.

(i) The heating-up period of each drop is negligible. This will cause overestimation of the true amount evaporated, but Williams (21) indicates the heating up time to be negligible at the conditions being considered.

(ii) The drop surface temperature is assumed to be the boiling point of the fuel (21). In the case of fuels with a boiling range, the temperature is assumed to be that at which 50% of the liquid has been boiled off, [50% distillation point] (22). If the assumed drop temperature is increased, the evaporation rate is decreased as the process of heat transfer to the drop is a function of the temperature difference between the ambient gas and the drop surface. Although studies of binary fuel mixtures [Wood, Rosser and Inami (23)] suggest that the composition of a multi-component fuel drop changes by batch distillation, narrow cut hydrocarbon drops whose components do not have widely differing thermodynamic properties exhibit the same evaporation characteristics as single component fuel drops (14).

(iii) The drops are assumed to have zero velocity relative to the gas. This is not strictly true in a turbulent system even if the mean relative velocity of each drop is zero, but the assumption is made due to the difficulty in estimating actual relative velocities in a highly turbulent flow situation. Furthermore this assumption is necessary for the interpretation of the residence time distribution experiments described in Chapter 6 to be valid for drop as well as gas phase. The effect of this assumption is to reduce the estimated drop evaporation rates somewhat. However, this effect is minor as evaporation rate enhancement due to convective effects is a function of Reynolds number (24), and will remain negligible for the small (52 μm evaporative mean diameter) drops present in the systems being considered.

(iv) The heat transfer to the drop by radiation is assumed to be negligible. This is based on the observations of Wolfhard and Parker (25) that hydrocarbon drops are almost transparent to the wavelengths radiated, and also on the calculations of Hottel et al. (26).

Using the above assumptions together with the assumption that Le ≈ 1, (where Le is the Lewis number), Spalding (27) arrived at the following equation for the evaporation of a single drop in a hot combustion environment.

$$\frac{dD^2}{dt} = -\kappa \qquad (3.2)$$

where $\kappa = \frac{8\bar{\lambda}}{\rho_\ell \bar{C}_p} \ln(1 + B_{ev}) \qquad (3.3).$

$\bar{\lambda}$ = 'mean' thermal conductivity, calculated as thermal conductivity of the surrounding gas at the arithmetic mean of Tg and T_ℓ (24)

$\bar{C}_p$ = 'mean' specific heat of surroundings calculated at the same temperature as $\bar{\lambda}$, above

ρ_ℓ = density of liquid drop.

$B_{ev} = \frac{\bar{C}_p(T_g - T_\ell)}{L_f}$ = transfer number for evaporation

T_g = temperature of surroundings.

T_ℓ = wet bulb temperature of drop (='boiling point in combustion environment).

L_f = latent heat of vaporisation at T_ℓ.

3.3: Spray Evaporation

Considering its importance in spray combustion and other systems, a theory of spray evaporation has been infrequently applied to the solution of combustion problems. The classical paper of Shapiro and Erickson (28) is the basis of the analysis of spray evaporation in one dimensional flow by F.A. Williams (29, chapter 11).

Hopkins and Eisenklam (30) applied the above analysis to the evaporation of a spray in both plug flow and continuous stirred tank reactors. They considered a spray whose drop size distribution was fitted by an equation of the form

$$G = bnD^{n-1}\exp\{-bD^n\} \qquad (3.4)$$

This is a more general form of equation (3.1), in which n is taken as 2.

They considered that each drop in the spray was burning rather than evaporating. Using the equations of mass transfer from a single burning drop given by Eisenklam et al. (24), together with an approximation relevant to the conditions in the combustion system, arrived at a drop evaporation law of the form

$$\frac{dD}{dt} = -\frac{1}{n\gamma} D^{1-n} \qquad (3.5)$$

where γ is a function of the properties of the fuel and the gas environment in the combustion space, the temperature, and the relative velocity between the drop and the gas.

n is taken as a constant equal to 1.55.

The combustion of the spray was modelled as the evaporation of a one dimensional spray cloud moving along a plug flow reactor. The differential equation governing the history of the particle spray size distribution as developed by Shapiro and Erickson (28) was combined with the initial drop size distribution (equation 3.4) and the drop evaporation equation (equation 3.5) to give the

incremental efficiency $\Delta\varepsilon$ of a plug flow reactor element as a function of the time spent in the element, and the parameters b and γ. The equation obtained was

$$\Delta\varepsilon = 1 - \exp(-\frac{b}{\gamma}\Delta t) \qquad (3.6)$$

where Δt = the incremental time spent in the plug flow reactor element.

This equation allows the evaporative efficiency in a plug flow reactor to be calculated directly by considering short increments in turn, over which the values of b and γ remain constant.

The efficiency of a perfectly stirred reactor was calculated by considering a plug flow reactor in infinite recycle.

An important assumption which was made in the analysis, but not specifically stated, is that the total number of drops in the spray remains constant. This as assumption would seem to be without any basis, as the rate of decrease of drop diameter due to evaporation increases as the drop becomes smaller. In other words, the smaller the drop the faster is the rate of decrease of its size. This is a direct result of the form of the drop evaporation equation (equation 3.5). In practice for a drop size distribution such as that present in sprays the smaller drops would completely disappear in relatively short time compared with that required to evaporate a substantial proportion of the complete spray volume, and therefore the total number of drops would decrease considerably.

In Chapter 4 models will be presented for the evaporation of a polysize spray in both CSTR and PFR reactors.

3.4: Mixing

The mixing characteristics of a combustion chamber may be described by two related concepts, developed in the chemical engineering literature.

The first concept is that of the gross flow pattern which determines the so called macromixing parameters of the flow field, which are defined by the residence time distribution of fluid elements passing through a reactor. The two macromixing extremes are represented by the continuously stirred tank reactor (CSTR) and the plug flow reactor (PFR) respectively, and in general the actual situation is somewhere between.

The second mixing concept is that of micromixing (or segregation), which determines the mixing history of each fluid element during its stay in the reactor. The one extreme on this micro-scale is represented by complete segregation, in which entering fluid elements pass through the system acting as integral batch reactors, without mixing with other fluid elements entering at different times. This extreme is necessarily the case for plug flow macromixing, but may also occur to a greater or lesser extent for any other macromixing situation. The other micromixing extreme assumes that mixing is complete on a molecular scale; that is, each molecule has access to each other molecule irrespective of whether they were in the same fluid element entering the reactor. This concept was developed by Danckwerts (31) and Zwietering (32).

In his review paper, Pratt (33) discussed the techniques available for analytical modelling of mixing processes, and their applicability to the modelling of continuous combustion systems. The following sections will describe the main approaches applicable to high intensity chambers.

3.4.1: Macromixing

Macromixing models of combustion systems which have been used in the past vary from the CSTR to the PFR extremes, with a number of analyses (30, 34, 35, 36) using combinations of these reactors to depict the flow pattern and residence time distribution which was assumed for a given system. No case of an experimentally determined residence time distribution for a high intensity chamber was found in the literature, hence the necessity for the above workers to assume a reactor configuration. Pratt (33; p.1344) ascribes this necessity to the inability of the available experimental methods to discriminate between various macromixing models in high intensity combustors, due to their insufficient accuracy.

3.4.2: Micromixing

The approaches that have been taken to the modelling of micromixing effects in combustion reactors may be divided into a number of categories:

(i) Models which assume a continuous distribution of mixing non-uniformities throughout a reactor.

The model of Fletcher and Heywood (35) represents a combustion zone as a completely segregated CSTR, in which the distribution of fuel-air ratio of the entering fluid elements is assumed to be Gaussian about the mean overall fuel-air ratio. The

standard deviation of the Gaussian distribution is used to characterize the degree of non-uniformity (unmixedness) in the system. Each individual element is assumed to instantaneously achieve the adiabatic flame temperature corresponding to its local fuel-air ratio and then proceeds through the reactor without heat or mass exchange with other elements. The reactor products are calculated by the standard method used for segregated CSTR's. This model is not entirely predictive as the micromixing parameter (the standard deviation of the equivalence ratio distribution) is not estimated a priori, but fixed to give best agreement between predicted and experimental results.

Also within this category of models is that of Gouldin (37) which assumed a Gaussian distribution for the degree of reaction in a well stirred reactor. This allowed him to estimate the influence of mixing of gas turbine emissions without actually estimating the mixing intensity.

(ii) Deterministic models, which are based on the work of Corrsin (38) have been used by Swithenbank (39), Vranos (40) and Evangelista et al. (41).

These models relate the rate of dissipation of local concentration fluctuations by turbulence to the power input per mass of fluid, the dimensions of the system and an empirical constant involving estimates of the efficiency of conversion of power into turbulent kinetic energy and of the Taylor microscale of the turbulent velocity field. Evangelista et al. (41) quote a value of the empirical constant for certain conditions and indicate the variables which would affect its magnitude.

Swithenbank (42) has successfully calculated the net turbulence generated by energy originating from pressure loss over baffles. This may be used directly to calculate the characteristic decay time of the local concentration fluctuations [called turbulent mixing time by Vranos (40)].

(iii) Stochastic models have been derived which apply probability concepts to proposed micromixing mechanisms.

Spielman and Levenspiel (43) applied these concepts to the coalescence and dispersion mixing model proposed by Curl (44). This model simulates transfer of material from a segregated to a maximally mixed phase. The random nature of the Monte Carlo simulation would appear to be particularly suited to the properties of homogeneous turbulent fields which are often assumed to exist in the combustion environment. The way in which this approach may be applied to combustion systems

using micromixing parameters taken from turbulence theory has been described by Sonnichsen and Pratt (45).

3.4.3: Mixing Analysis Used

In the present analysis the macromixing characteristics of a combustion chamber will be ascertained by carrying out stimulus response tests under operating conditions. The data from these tests will be analysed as shown in Chapter 2 to identify the flow configuration in terms of a combination of stirred and plug flow reactor elements. The configurations considered feasible are based on the physical and aerodynamic factors known to play a key role in determining the macromixing in the chamber.

The high intensity chamber is assumed to be in a state of maximum mixedness (32), so that the CSTRs in the flow configuration are micromixed. This assumption is considered a reasonable first approximation in view of the high intensity turbulence levels which the chamber aerodynamics was designed to generate, and is made in the absence of more accurate information that could be readily obtained.

3.5: Pyrolysis

Pyrolysis is the process of breakdown of hydrocarbon molecules by heat to form, ultimately, carbon monoxide and water and/or hydrogen. In some combustion systems, particularly where there is insufficient local oxygen present, the hydrocarbon molecule is subjected to intense heating and pyrolyses faster than oxygen can diffuse to it. This results in soot and char formation, especially from fuels containing long-chain hydrocarbons.

The mechanism of pyrolysis is as yet poorly understood for the most commonly used fuels, and a number of approaches have been taken where this process is included as part of an overall combustion model. The approach taken usually reflects the complexity of the fuel (as mechanism and rate information are available only for the simpler fuels) and the importance of the pyrolysis kinetics to the predictions being made.

Detailed pyrolysis mechanisms and rate data have been used for methane (46) and ethane (47) combustion systems. Chinitz and Baurer (48) have developed complex chemical kinetic mechanisms for a number of straight chain hydrocarbons, aldehydes, alcohols and other partially oxidised species, but application of this or similar data to combustion system modelling has not yet been reported in the open literature.

Mosier et al. (49) accounted for the pyrolysis process by an empirical approach. The JP-5 fuel was said to be adequately represented, both chemically and thermodynamically (specific heat, heat of formation) by the formulation C_8H_{16}. The combustion process was modelled as taking place in three broad stages. The first stage produced "light, unburned and partially oxidised" hydrocarbons and would correspond roughly to the pyrolysis concept. The three reactions in stage one were:

(i) $C_8H_{16} + O_2 \rightarrow 2C_4H_8O$

(ii) $C_4H_8O + O_2 \rightarrow HO_2 + CO + CH_3 + C_2H_4$

(iii) $C_8H_{16} + OH \rightarrow H_2CO + CH_3 + 3C_2H_4$

However, to be entirely consistent, the second stage (which includes the principal exothermic reactions) producing large amounts of carbon monoxide and water would be included in the definition of pyrolysis at the beginning of this section.

The factor that seems to differentiate stage one from stage two is the necessity to estimate rate constants for global reactions used to represent the unknown mechanism of stage one. These rate constants were determined by fitting a rate equation to experimental ignition delay data. The mechanism and rate data for the subsequent reactions of the stage one products are, with one exception, available from the literature. Furthermore, as an illustration of how little understood the pyrolysis mechanism of even the C_8H_{16} formulation is, the aldehyde intermediate is stated to be purely hypothetical, being introduced only for computational convenience. The complex system of equations developed was subsequently replaced by a reduced kinetic-partial equilibrium system said to be capable of predicting those aspects of system behaviour that are important to the determination of exhaust emissions. On inspection this reduced scheme is more empirical than the overall scheme arrived at by assuming global pyrolysis to carbon monoxide and hydrogen followed by a detailed mechanism such as those discussed in section 3.6.

Estimates may be made of global pyrolysis rates without reference to any mechanism. Such an estimate has been given by Edelman et al. (50) for the reaction

$$C_nH_m + \frac{n}{2} O_2 \rightarrow \frac{m}{2} H_2 + nCO$$

and this was combined with detailed hydrogen, carbon monoxide and nitric oxide kinetics in a model predicting nitric oxide formation described by Engelman et al.

(51). This model was found to give good agreement with experiments for carbon monoxide/air and for hydrogen/air combustion, but to underpredict nitric oxide formation for propane/air combustion. This was attributed to inaccuracy in the quasi-global hydrocarbon combustion mechanism and/or rate.

The simplest pyrolysis assumption is that the fuel molecules pyrolyse instantaneously to carbon monoxide and hydrogen. This assumption was used by Hammond and Mellor (52) and would be expected to lead to an overestimation of the combustion temperature, heat release rate, nitric oxide production and reactor loading at blowout. The extent of the overestimation would depend on the rate of pyrolysis relative to the other processes occurring.

In view of the underprediction of nitric oxide formation in the highly stirred system used by Engleman et al. (51) due to probable underestimation of the global pyrolysis rate, and in the absence of any reliable data applicable to the gas oil fuel used, an infinite pyrolysis rate was assumed for the present analysis.

3.6: Reaction Mechanism and Kinetics

This section will discuss the mechanism and kinetics of the gas phase reactions involving oxidation of the carbon monoxide and hydrogen fuel pyrolysis products as well as formation of nitric oxide pollutants.

If combustion modelling is concerned primarily with prediction of combustion efficiency (or intensity), only the temperature and main constituents of the products are required to be estimated, and global rate equations for the overall kinetics of the hydrocarbon oxidation may be used. A global rate equation proposed by Kretschmer and Odgers (53) has been used in analysis of the above type (54). In some cases the kinetics of the water-gas reaction is sufficiently fast relative to the residence time, that equilibrium for this reaction may be used to calculate the composition of the major combustion products (55).

However, when a model is required to predict the pollutant emissions (viz. unburnt hydrocarbons, carbon monoxide and nitric oxides) a more detailed kinetic model is necessary.

The simplest approach involves an assumption that the hydrocarbon chemistry may be decoupled from the nitric oxide chemistry. This assumption is based on the relatively slow nitric oxide formation kinetics compared with the hydrocarbon combustion rate, as shown by Marteney (56). An equilibrium hydrocarbon combustion

model is used to calculate equilibrium concentrations of O, OH, H, N, etc. which are subsequently used as input to the nitric oxide formation kinetic model. This can lead to errors, as it has been found that in some circumstances the actual concentrations of some of the key species in the nitric oxide formation mechanism are significantly in excess of their equilibrium values. Bowman (57) gives an example of O atom concentrations one hundred times in excess of the equilibrium values, but states that the simplified approach is still valid provided the key atomic species concentrations are correctly estimated. This approach, which "decouples" the hydrocarbon and the nitric oxide mechanisms is mainly applicable to one dimensional flames where nitric oxide formation has been found to occur in the post flame zone. Lavoie et al. (58) made this observation for an internal combustion engine. In their analysis all the species entering the NO kinetic mechanism were assumed present in their local equilibrium proportions, except for N atoms whose concentration was calculated from an approximation that it was in equilibrium with NO. Appleton and Heywood (59) and Fletcher (60) have applied the same "decoupled" approach to models based on combustion in gas eddies, apparently on the grounds that the assumption considerably simplified the calculations, while at the same time enabling the model to retain some valuable predictive capacity. Fletcher (60) indicates that the use of decoupled kinetics would limit the application of the resulting model, but does not specify the limitations.

In highly stirred regions of high intensity combustion chambers, the mixing process is effectively instantaneous, so that these regions are modelled as micromixed CSTRs. The combustion reactions in a micromixed CSTR take place throughout the volume at uniform reactor conditions, and the concept of a flame front is not valid. Thus, processes which may be decoupled in one dimensional systems due to their occurring subsequent to one another must occur simultaneously in CSTRs (zero-dimensional reactors). In such cases the nitric oxide kinetics will be affected by super-equilibrium levels of reaction intermediates present throughout the burning volume where all reactions occur simultaneously.

In the present analysis it will be assumed that the fuel pyrolyses instantaneously (see section 3.5) to carbon monoxide and hydrogen, with the subsequent heat releasing and nitric oxide pollutant forming reactions occurring simultaneously. The kinetic mechanism used to model these reactions is that proposed by Malte and Pratt (61), and may be divided up into a number of separate but interrelated sections as shown in Table 3.1. Also given in Table 3.1 are the parameters of the rate

TABLE 3.1 REACTION MECHANISMS AND RATE DATA FOR FORWARD REACTIONS

(After Malte and Pratt (61))

REACTION	RATE EQUATION †: $k = 10^A T^{N_k} \exp(-E/R_u T)$ RATE CONSTANT PARAMETERS FOR EQUATION		
	A	N_k	E (kcal/mol)
ZELDOVICH MECHANISM			
$O + N_2 = NO + N$	14.133	0.0	75.400
$N + O_2 = NO + O$	9.810	1.0	6.250
$N + OH = NO + H$	13.600	0.0	0.0
NITROUS OXIDE MECHANISM			
$N_2 + O + M = N_2O + M$	11.210	0.0	3.180
$N_2O + O = NO + NO$	13.661	0.0	24.100
$N_2O + O = N_2 + O_2$	13.581	0.0	24.100
$N_2O + H = N_2 + OH$	13.470	0.0	10.770
NITROGEN DIOXIDE MECHANISM			
$NO + O + M = NO_2 + M$	10.593	1.0	-9.540
$O + NO_2 = NO + O_2$	13.000	0.0	0.600
$H + NO_2 = NO + OH$	14.858	0.0	1.930
HYDROGEN COMBUSTION MECHANISM			
$O_2 + H_2 = OH + OH$	14.903	0.0	45.000
$OH + H_2 = H_2O + H$	14.439	0.0	10.300
$O_2 + H = OH + O$	14.677	0.0	17.300
$O + H_2 = OH + H$	12.352	0.0	7.750
$O + H_2O = OH + OH$	14.095	0.0	18.100
$H + H + M = H_2 + M$	18.699	-1.150	0.0
$O + O + M = O_2 + M$	15.672	-0.280	0.0
$O + H + M = OH + M$	16.627	0.0	-2.780
$H + OH + M = H_2O + M$	16.778	0.0	-0.500
CARBON MONOXIDE COMBUSTION MECHANISM			
$CO + OH = H + CO_2$	11.336	0.0	0.596
$CO + O + M = CO_2 + M$	14.000	0.0	2.500
$CO_2 + O = CO + O_2$	13.279	0.0	54.150

†Notes 1) Values quoted for E are in the units quoted in the original reference and used in the calculations. To convert to SI units multiply kcal/mol by 4186.8 to obtain J/mol.

2) M denotes any molecule acting as a gas phase catalyst in three-body reactions.

3) Values of k calculated from the above parameters are in $cm^3/mol\ s$. To obtain the value of k in $m^3/mol\ s$ multiply by 10^{-6}.

constant equation for each forward reaction. The rate constant is expressed by

$$k = 10^{A} T^{N_k} \{\exp -E/R_u T\} \qquad (3.7)$$

where k = rate constant for forward reaction

E = activation energy

R_u = universal gas constant

T = temperature

A, N_k = parameters of rate constant equation.

It is assumed that there is no nitrogen in the fuel, so that a 'fuel nitric oxide' mechanism is not considered.

The reasons for choosing the particular mechanism and the sources of the rate constants are discussed at length by Malte and Pratt (61) and will not be repeated here. It is felt that the mechanism is applicable to the system being studied as it includes all the reactions considered important by Caretto (62). Also included is a nitrous oxide mechanism which was found to be important relative to the Zeldovich kinetics at temperatures below approximately 1800°K (61) which may occur in some of the fuel lean reactor elements corresponding to recirculation zones in the chamber. For most of the reactor elements of the model which will be used, (and correspondingly in most parts of a spray combustion chamber), the reacting mixture will be fuel lean due to the staged addition of fuel controlled by the rate of spray evaporation. Only when the final part of the spray is evaporating does the environment become fuel rich. For fuel rich combustion where H and OH concentrations become substantial, Engleman et al. (51) recommend that the reaction

$$N + OH = NO + H$$

be included. This reaction is also present and the scheme should therefore be applicable to all regions of the chamber. The relative rate constants of each reaction at the temperature and the species concentrations in each reactor element will determine which reactions are important, and calculate the products accordingly.

4: MODELLING OF SPRAY COMBUSTION SYSTEMS

After reviewing some basic concepts important in combustion chamber design and previous modelling work, this chapter will describe a proposed approach for comprehensive modelling of high intensity chambers. In particular the use of a configuration of CSTR and PFR elements to describe a chamber in a way directly related to its aerodynamics will be discussed.

Following this, a model will be developed for the evaporation of a polysize spray in both a CSTR and a PFR. The model will be based on physical and chemical processes and parameters whose validity and limitations in a high intensity spray combustion environment (and in particular, in the system used for the experimental work) were discussed in chapter 3.

Finally, the method of calculation for spray combustion in a CSTR will be described, and predictions for the combustion of a gas oil spray under different conditions presented.

4.1: Background and Previous Work

This section will first discuss concepts relevant to combustion chamber design and modelling and then critically review spray combustion models which have been previously developed.

4.1.1: Concepts Applying to Combustion Systems in General. A concept that arises from the application of chemical reactor theory to combustion has been recognised as basic to the design of most types of combustion chamber including those fuelled by liquid sprays. This concept was developed by Bragg (63) and essentially states that for maximum combustion intensity, the total volume of a combustion chamber should be divided into a stirred section for ignition and flame holding, followed by a plug flow section for burn out.

In his original paper Bragg (63) used a bimolecular rate of chemical reaction between fuel and air as determined by the composition of the burning mixture to calculate the optimum conversion in each section of a combustion chamber. In the fuel rich primary zone, air and fuel are supplied to maintain the highest possible reaction rate when mixed together with the recycled products, while in the secondary zone combustion is completed at successively weakening fuel air ratio as fresh air is added. The rate of fuel disappearance in the secondary zone is

approximately exponential (as it depends on an assumed bimolecular reaction). Bragg showed that an optimum value exists for the ratio of the primary to secondary zone volumes.

De Zubay (64) and Hardcastle (65) considered combustion in stirred reactors in series, using the same rate equation as Bragg (63) and calculated the effects of different air and fuel feed strategies. They concluded that:

(i) For high combustion efficiency it is advantageous to carry out the process in more than one stage.

(ii) For minimum reactor volume all the fuel should be introduced in the first stage

and (iii) For a reactor operating air rich, combustion should be carried out stoichiometrically in the first stage, with the excess air added subsequently.

Beer and Lee (66) carried out tracer experiments on a pulverized fuel furnace and showed that the furnace could be divided into two sections; a stirred followed by a plug flow section, corresponding to the two zones shown to be desirable by Bragg (63). They found that the relative proportions of the two sections was dependent on the degree of swirl in the furnace, and found theoretically that there was an optimum ratio of mixed to plug flow volumes for maximum combustion efficiency.

Even though the above analyses are for simplified models, it may be safely concluded that some combination of reactors will lead to a higher combustion intensity and efficiency than a single plug flow or stirred reactor. The optimum arrangement will be a function of the rate controlling steps and the required fuel combustion efficiency.

The desirability of a stirred section in a combustion chamber stems from stability considerations. This requires that heat be supplied to raise the temperature of the fresh feed sufficiently to cause ignition and is often achieved by recycling back a proportion of the hot products, and mixing these with the feed. The recirculation zone present in many practical combustors near the feed inlet achieves the above effect and allows stable combustion to proceed for a wide range of conditions (turndown). Such recirculation zones are effectively CSTRs, and their characteristics may be studied by modelling them as such.

Vulis (67) has shown how the equations of heat release and heat removal may be used to calculate the conditions required for stability of exothermic CSTRs, and how

these conditions are affected by various parameters. In view of the relevance of these considerations to high intensity combustion chambers, some of the basic elements of Vulis' approach and conclusions are presented here.

The heat release rate per unit mass throughput (used as the basis for all calculations), as a function of dimensionless temperature, θ ($= R_u T/E$), was calculated for an adiabatic CSTR for different values of the mean residence time, τ, as shown in figure 4.1(a). The completeness of reaction (i.e. fractional conversion of feed to products), η, is directly related to the heat release rate, so that the vertical axis of figure 4.1(a) may be labelled in terms of either. Another relationship which holds for the system is that determined by the heat removal rate, which relates the heat carried away by the reaction products to the conversion. For a given feed temperature and feed composition, this relationship is given by the straight line shown in figure 4.1(a). The intersection of the heat release and heat removal curves indicate possible steady states, the stability of each of which is determined by whether a perturbation in the system causes it to return to or digress further from the particular steady state. Vulis (67) discusses these points at length and shows how various parameters affect the relative positions and shapes of the heat release and removal curves and in turn the operating characteristics of an exothermic CSTR. Some relevant conclusions follow.

For typical systems, figure 4.1(b) shows the effects of changes in τ on conversion (or temperature). The point on the top branch at $1/\tau = 0$ corresponds to the thermodynamic equilibrium conversion and temperature that would be reached in an adiabatic batch reactor ($\tau \to \infty$). As $1/\tau$ is increased along the top (stable combustion) branch, the conversion and temperature decrease steadily until point B is reached, when the system becomes unstable and blow-out occurs, with a sharp drop in conversion and temperature to the lowest branch of the curve. If the value of $1/\tau$ is less than that at point B, the conversion remains at the level given by the lowest branch until some ignition source raises the system temperature (and conversion) to the value given by the central branch (ignition) for that value of τ. As soon as this occurs, the system will rapidly attain the stable combustion condition given by the top curve.

The effect of varying the feed temperature, θ_0, on the heat removal line is shown in figure 4.1(c). Consideration of the stability of intersections with a given heat release curve as θ_0 changes shows an hysteresis effect as follows. As feed temperature is decreased past that for blow-out ($\theta_{0,B}$) the conversion drops

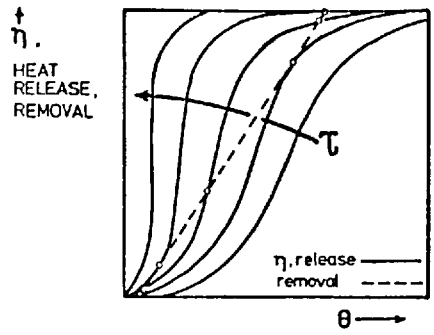

(a) Effect of τ on conversion and heat release.

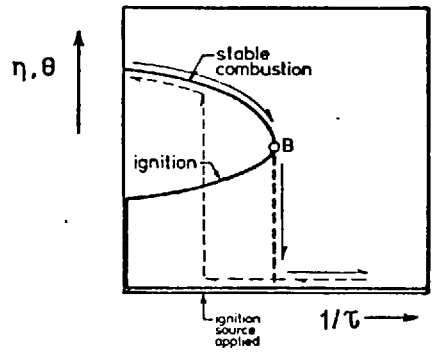

(b) Effect of τ on steady state conversion.

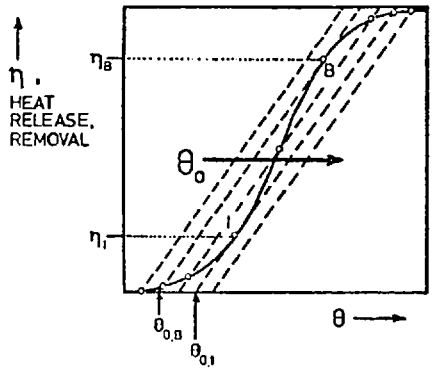

(c) Effect of feed temperature on heat removal.

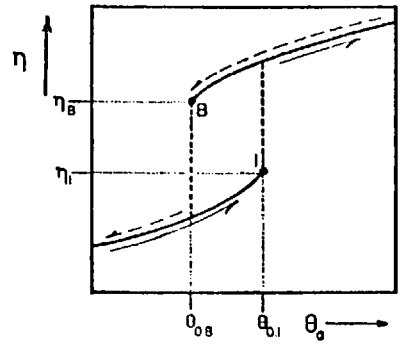

(d) Effect of feed temperature on conversion.

FIGURE 4.1 Stability diagrams for an exothermic CSTR.

suddenly to the lower intersection between the heat release and removal curves. However, as the feed temperature is increased again, a higher feed temperature than $\theta_{0,B}$ is required for ignition. This temperature is shown as $\theta_{0,I}$ on figure 4.1(c). This hysteresis phenomenon is shown in figure 4.1(d), which shows the variation of conversion with feed temperature for both increasing and decreasing θ_0.

Vulis (67) develops many other predictions from his exothermic CSTR model. Only the above are described here as they clarify aspects of the blow-out phenomenon which are relevant to predictions of spray combustion reactor stability presented in later sections of this work.

The prediction of Vulis relevant to this section is that, for maximum combustion intensity, a CSTR should be operated near the blow-out condition with typically 60-70% conversion of fuel to products. This means that, for complete conversion, a subsequent plug-flow 'burn-out' section is required as specified by Bragg.

4.1.2: Spray Combustion Modelling. Early spray combustion models were developed for rocket systems, which were assumed to be one dimensional (plug flow) reactors in which the spray evaporated as it passed along the length of the rocket chamber. Stability was not considered, hence the absence of a stirred section. The combustion rate was assumed to be evaporation controlled with the available amount of fuel at any section determined by summing the vapour produced from each drop size group in the spray. These analyses allowed the combustion efficiency or the minimum chamber length for complete combustion to be estimated. Well known examples of this approach are those of Priem and Heidmann (68), Spalding (69) and Williams (70). A more recent one-dimensional analysis by Nuruzzaman et al. (71) calculated the burn out of a spray with an initial Rosin-Rammler size distribution without dividing the spray up into a number of size groups.

Hopkins and Eisenklam (30) developed a theory of spray combustion which predicted the evaporative efficiency for stirred and plug flow reactors. Their theory has been reviewed in section 3.3.

Courtney (72) derived a theoretical expression for combustion intensity in a stirred spray reactor but due to its complexity and the fact that it was not explicit, it could only be used to indicate qualitative effects which were previously known.

More recently much effort has been invested in the modelling of gas-turbine combustors, with a view to predicting the emission of pollutants at different operating conditions. This requirement has led to the development of complex kinetic models of the chemical reactions taking place in the combustion environment. Reviews of the work in this field were recently published by Mellor (73) and Odgers (74). None of the models presented in these reviews take spray evaporation into account, on the grounds that it is not a rate limiting process for the drop sizes present. Odgers (74) estimates the evaporation time of a fuel drop as a function of drop diameter, combustor pressure and drop Reynolds number and concludes that drops less than 100 μm in diameter should completely evaporate in the time available. Even if this is so, the assumption would lead to some error as the finite evaporation rate would result in a reduction in the rate of fuel addition. Under certain conditions heterogeneous processes are believed to play an important part in determining emissions both of nitric oxides (19, 20), and of unburnt hydrocarbons and carbon monoxide (49) and for this reason it would be desirable that they be considered. Thus, the basis for most current gas turbine combustion modelling is gas phase reaction kinetics, (discussed in section 3.6), combined with a proposed flow model such as those described by Mellor (73). In some cases provision for allowing for mixing nonuniformities, in the form of equivalence ratio distributions (35, 60) or in the form of effective reductions in the reaction rate (54). The last model does not estimate pollutant emissions.

4.2: Development of Models Related to Combustion Chamber Parameters

The approach proposed here for the modelling of high intensity spray combustion chambers requires two distinct inputs.

The first is a detailed knowledge of the aerodynamics of the chamber, expressed in terms of a flow configuration of mixed and plug flow reactor elements (i.e. a flow model). This is derived from stimulus response experiments carried out on the chamber under operating conditions, as described in chapters 5 and 6. An important feature of the flow model is that it should relate to the actual aerodynamics, with each reactor element corresponding qualitatively to an actual part of the chamber with respect to volume, throughput and reactor type. The results of the stimulus response experiments are therefore used to select and determine the parameters of a flow model from feasible alternatives likely to result from the geometry and feed stream momenta in the chamber.

The second input required is a spray combustion model for each type of reactor element. This allows calculation of each reactor element of the flow configuration in turn and hence a knowledge of the conditions, not only in the exit stream but also in each region of the chamber.

The spray combustion model to be used for each reactor element will be based on a number of assumptions as follows.

(i) The processes taking place in each reactor element depend only on the properties of the feed to the reactor and the reactor characteristics. There is no transfer of mass by diffusion or energy by radiation between reactor elements; all transfer is by convective flow of product and feed streams. Each reactor element is adiabatic.

(ii) The reactor elements are restricted to either micromixed perfectly stirred or plug flow reactors. This limitation is based on the following. Firstly most regions in high intensity combustion chambers are well approximated by one of these reactor types due to the inherently intense mixing present ("perfect stirring") being brought about by high momentum (plug flow) feed jets. Secondly, if necessary, a partially mixed region or a chamber may be represented by a combination of the two reactor types.

(iii) The amount of fuel available for combustion in any reactor element is determined by the amount of spray evaporating in the element. Unevaporated spray leaves with the combustion products.

Subsequent sections will present analyses of spray evaporation in stirred and plug flow reactor elements, and derive expressions for the evaporative efficiency of a reactor as a function of parameters of the spray and of the reactor.

The application of these expressions to the analysis of spray combustion reactors will then be demonstrated. Results showing the effects of drop size, equivalence ratio, combustion air temperature and reactor mean residence time on combustion efficiency, temperature, nitric oxide emissions and blow-out in a CSTR will be presented.

4.3: Spray Evaporation in a Continuous Stirred Tank Reactor

An analysis of the evaporation of a polysize spray in a CSTR will be presented in this section. The resulting equation will express the fraction of spray evaporated as a function of the reactor mean residence time, the drop evaporation constant and the parameter of the drop size distribution. The results are obviously only applicable to sprays whose drop size distribution is adequately described by the single parameter equation used.

The drop size distribution of the spray is defined in terms of G, the drop number size distribution function which is given by equation 3.1.

$$G = \frac{d\overline{N}}{dD} = 2bD \exp(-bD^2) \tag{3.1}$$

By defining a reference diameter D* as

$$D^* = \sqrt{\frac{1}{2b}} \tag{4.1}$$

and substituting for b in equation 3.1, one obtains

$$D^*G = \frac{D}{D^*} \exp\{-\frac{1}{2}(\frac{D}{D^*})^2\} \tag{4.2}$$

which is a dimensionless form of equation 3.1, i.e.

$$\overline{G} = \overline{D} \exp(-\frac{1}{2}\overline{D}^2) \tag{4.3}$$

where $\overline{G} = D^*G$, a dimensionless number size distribution function

and $\overline{D} = \frac{D}{D^*}$, a dimensionless diameter.

The evaporation rate of each drop in the spray is given by equation 3.2, and may be expressed in the form

$$\frac{dD}{dt} = -\frac{\kappa}{2D} \tag{4.4}$$

Shapiro and Erickson (28) analysed the evaporation of a spray cloud in a "large medium" (i.e. one whose properties does not change as a result of the evaporation). Their analysis is applicable to stationary or moving spray clouds provided that the residence time distribution of the constituent drops is not a function of their size.

The case of a CSTR in which the residence time distribution of the drops in a spray fed to the reactor is not a function of drop size is a classic case of spray evaporation in a "large medium", as defined above. The reason for this is that the conditions in a CSTR are uniform throughout, with properties undergoing a step change only on entry to the reactor. The conditions inside the reactor are determined partly by the evaporating drops, but these conditions remain constant (at steady state operation) and therefore satisfy the above condition rigorously.

The analysis of Shapiro and Erickson (28; p.781) shows that when a spray cloud with a size distribution given by equation 4.3 evaporates under constant conditions, with each drop evaporating at a rate given by equation 4.4, the drop size distribution remains unchanged. The loss of spray volume due to evaporation is accounted for by an equal fractional reduction in the volumetric concentration of drops of all sizes. Consequently when a spray evaporates in a CSTR (with equations 4.3 and 4.4 satisfied), the step change in spray properties on entering the reactor is restricted to the number of drops per volume of fluid, with the drop size distribution remaining the same as that of the spray feed.

A slight complication is introduced in systems where there is a density difference between the feed and product streams. The balance on which spray evaporation efficiency is calculated for such systems is related not to volumetric but to mass flow rates as only the latter remain the same for both input and output streams. Combustion reactors are examples of systems where extreme density change occurs and the following analysis will therefore be made on the basis of mass throughput rather than volume.

A balance on the drop volume in a CSTR may be made as follows

$$\begin{array}{l}\text{Rate of spray evaporation} \\ \text{in reactor}\end{array} = \begin{array}{l}\text{Rate of entry of} \\ \text{drop volume}\end{array} - \begin{array}{l}\text{Rate of exit} \\ \text{of drop volume}\end{array} \qquad (4.5)$$

Let N = number of drops per unit mass of fluid in the reactor

N_0 = number of drops per unit mass of fluid in the feed stream

$\dot{m}$ = mass throughput of CSTR

m = mass of fluid in the CSTR

V = total volume of drops in the CSTR at any time

G = number size distribution of drops for both inlet and outlet streams

$$V = m.\left(\frac{N\pi}{6}\right) \int_0^\infty GD^3 dD \qquad (4.6)$$

The rate of volume loss from the spray by evaporation is given by

$$-\frac{dV}{dt} = -\frac{d}{dt}\left\{\frac{mN\pi}{6}\int_0^\infty GD^3dD\right\} \tag{4.7}$$

$$= -\frac{mN\pi}{6}\int_0^\infty \{GdD.\frac{dD^3}{dt}\} \tag{4.8}$$

But,
$$\frac{dD^3}{dt} = 3D^2\frac{dD}{dt} \tag{4.9}$$

and, from equations 4.4 and 4.9

$$\frac{dD^3}{dt} = -\frac{3}{2}\kappa D \tag{4.10}$$

$$\therefore \quad -\frac{dV}{dt} = \left(\frac{mN\pi}{6}\right)\left(\frac{3}{2}\kappa\right)\int_0^\infty GDdD \tag{4.11}$$

The feed rate of drop volume to the CSTR is given by

$$\dot{m}\left(\frac{N_o\pi}{6}\right)\int_0^\infty GD^3dD \tag{4.12}$$

and the exit rate is given by

$$\dot{m}\left(\frac{N\pi}{6}\right)\int_0^\infty GD^3dD \tag{4.13}$$

Substituting equations 4.11, 4.12 and 4.13, the balance, equation 4.5 becomes

$$m\left(\frac{N\pi}{6}\right)\left(\frac{3}{2}\kappa\right)\int_0^\infty GDdD = \dot{m}\left(\frac{N_o\pi}{6}\right)\int_0^\infty GD^3dD - \dot{m}\left(\frac{N\pi}{6}\right)\int_0^\infty GD^3dD \tag{4.14}$$

rearranging and substituting $\tau = \frac{m}{\dot{m}}$ (4.15)

= mean residence time of the CSTR,

one obtains

$$\frac{3}{2}\kappa\tau.\ \frac{\int_0^\infty GDdD}{\int_0^\infty GD^3dD} = \frac{N_o}{N} - 1 \tag{4.16}$$

The mean evaporative diameter, $\overline{D}_{31}$, is defined by

$$(\overline{D}_{31})^2 = \frac{\int_0^\infty GD^3 dD}{\int_0^\infty GDdD} \tag{4.17}$$

and for the drop size distribution function of equation 3.1, is shown in Appendix D to be given by

$$\overline{D}_{31}^{\,2} = \frac{1.5}{b} \tag{4.18}$$

Combining equations 4.18, 4.17 and 4.16 one obtains

$$\kappa\tau b = \frac{N_0}{N} - 1 \tag{4.19}$$

The evaporative efficiency of the reactor, ε, is defined as the fraction of the spray volume which is evaporated. When the spray drop size distribution remains the same the evaporative efficiency may be expressed directly in terms of the fractional change in the number of drops per mass of fluid passing through the reactor.

i.e. $$\varepsilon = \frac{N_0 - N}{N_0} \tag{4.20}$$

or $$\varepsilon = 1 - \frac{N}{N_0} \tag{4.21}$$

Combining equations 4.21 and 4.19 leads to

$$\kappa\tau b = \frac{\varepsilon}{1 - \varepsilon} \tag{4.22}$$

or $$\varepsilon = \frac{\kappa\tau b}{1 + \kappa\tau b} \tag{4.23}$$

which expresses the evaporative efficiency of a CSTR explicitly in terms of the parameters of the drop evaporation equation, the spray drop size distribution and the mean residence time of the CSTR.

As b is directly related to the spray mean evaporative diameter by equation 4.18, the effect of changes in $\overline{D}_{31}$ on ε may be easily calculated for constant κ and τ. From equations 4.18 and 4.22

$$\frac{\varepsilon}{1 - \varepsilon} \propto \frac{1}{(\overline{D}_{31})^2} \tag{4.24}$$

so that a change in ε may be related to a change in $\bar{D}_{31}$ as follows.

Let ε and ε_0 be the efficiencies at $\bar{D}_{31}$ and $(\bar{D}_{31})_0$ respectively, for constant K and τ. For a given value of ε_0, a change in the value of mean evaporative diameter from $(\bar{D}_{31})_0$ to $\bar{D}_{31}$ will result, according to equation 4.24, in a new value of ε given by

$$\frac{\varepsilon}{1-\varepsilon} = \frac{\varepsilon_0}{1-\varepsilon_0} \cdot \frac{\{(\bar{D}_{31})_0\}^2}{\bar{D}_{31}} \qquad (4.25)$$

From equations 4.25, 4.22 and 4.23, ε may be easily calculated for any ε_0 and relative change in $(\bar{D}_{31})_0$. The relative change in ε_0 may be expressed by ε_{rel}, given by

$$\varepsilon_{rel} = \frac{\varepsilon}{\varepsilon_0} \qquad (4.26)$$

Figure 4.2 shows the values of ε_{rel} for a range of values of ε_0 and a value of $(\bar{D}_{31})_0$ of 100 μm. The conclusion that may be drawn from this figure is that as the evaporative efficiency of a reactor, ε_0, increases it becomes less sensitive to changes in evaporative mean diameter of the spray feed. Each curve is seen to approach an asymptote for small $\bar{D}_{31}$, which corresponds to an efficiency of 100%. The observation that this asymptote is closely approached at $\bar{D}_{31}$ = 10 μm concurs with experimental observations that sprays in this size range behave as a premixed vapour fuel in combustion systems (75).

4.4: Spray Evaporation in a Plug Flow Reactor

The conditions in a plug flow reactor (PFR) by definition satisfy the conditions of Shapiro and Erickson's (28) spray cloud requirements, as all drops entering a PFR together necessarily remain together, due to the absence of a distribution of residence times.

For sprays adequately described by the drop size distribution of equation 3.1, which evaporate according to equation 3.2, the evaporative efficiency of a PFR is shown by Shapiro and Erickson (28; equation 20c) to be given by

$$\varepsilon_{PFR} = 1 - \exp(-K\tau b) \qquad (4.27)$$

where τ refers to the residence time of the PFR.

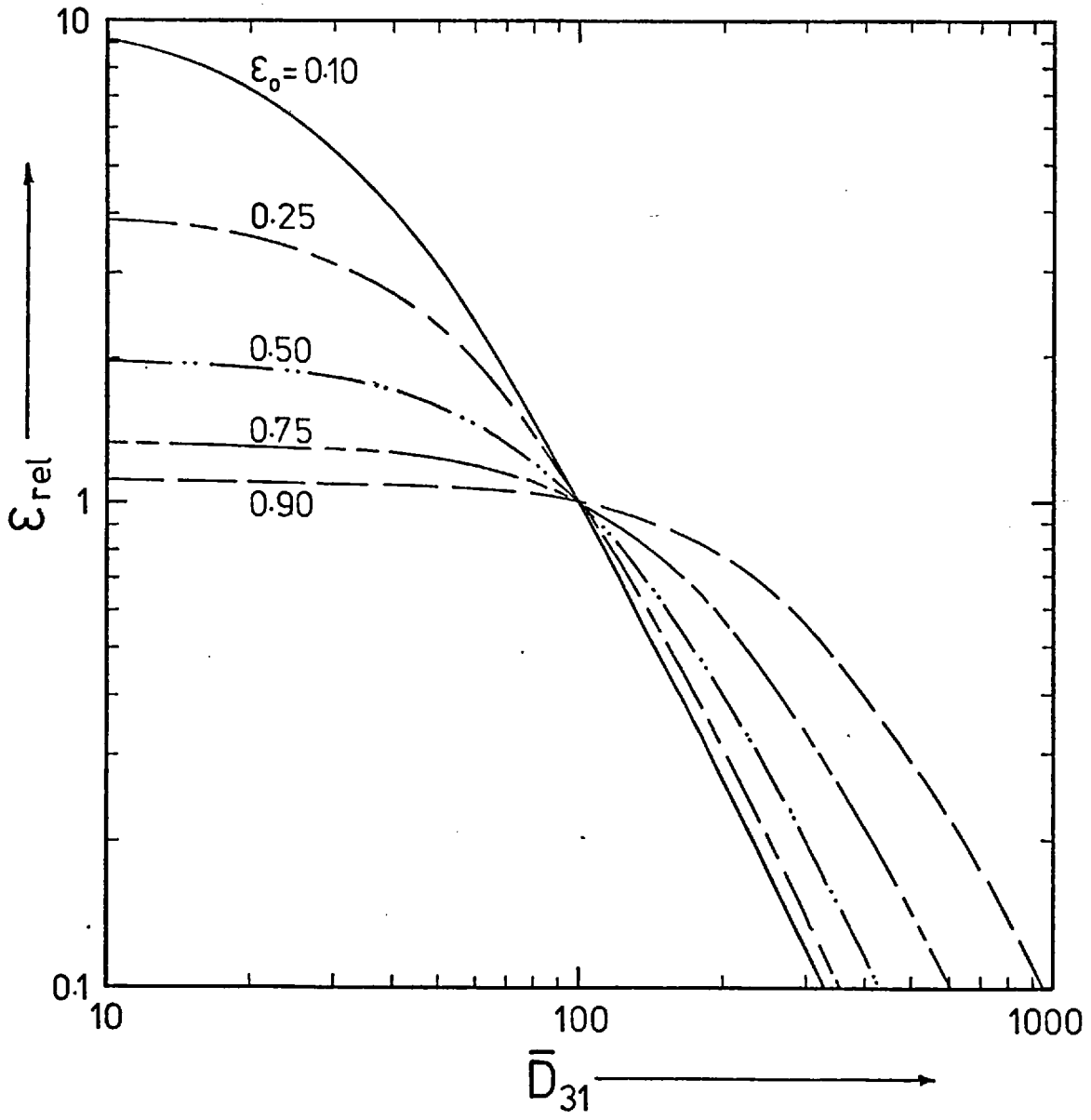

FIGURE 4.2 Relative evaporative efficiency of a CSTR as a function of mean evaporative diameter.

Care must be exercised in the application of equation 4.27. In practice the conditions along a PFR change, and this will affect the value of the drop evaporation constant κ, so that PFR s must be divided up into short increments over which conditions are nearly constant and the efficiency, temperature etc. calculated for each increment in turn.

Under certain conditions, the evaporative efficiency of an increment of PFR will be very nearly the same as that in a CSTR with the same value of $\kappa\tau b$. If this is so, it would allow a combustion chamber to be modelled in forms of CSTRs only, even if some plug flow regions are present.

From equations 4.27 and 4.23

$$\frac{\varepsilon_{CSTR}}{\varepsilon_{PFR}} = \frac{\kappa\tau b}{(1 + \kappa\tau b)} \{1 - \exp(-\kappa\tau b)\}^{-1} \qquad (4.28)$$

and the relative error in using ε_{CSTR} instead of ε_{PFR} for an increment of PFR is given by

$$\frac{\varepsilon_{PFR} - \varepsilon_{CSTR}}{\varepsilon_{PFR}} = 1 - \frac{\varepsilon_{CSTR}}{\varepsilon_{PFR}} \qquad (4.28a)$$

Figure 4.3 shows that for any required accuracy, a value of $\kappa\tau b$ may be selected (by adjusting τ) which is sufficiently small for a CSTR to be used to calculate ε for an incremental volume of a PFR. A maximum relative error of about 20% occurs at $\kappa\tau b \sim 2.0$. For values of $\kappa\tau b$ greater than 1.0 both ε_{PFR} and ε_{CSTR} approach 100%, so that the difference between them diminishes. However, this range of $\kappa\tau b$ is in general unacceptable for use in CSTRs approximating incremental PFRs because at high ε sufficient spray will evaporate to cause varying conditions along the increment, contradicting the assumptions of the model. The exception to this is if the relative amount of spray present is so small that even if it all evaporates, the temperature and composition of the gas remain constant.

4.5: Spray Combustion in a Continuous Stirred Tank Reactor

The method proposed for calculation of spray combustion in a CSTR involves an iterative procedure in which an estimate of the evaporative efficiency of the reactor is used to determine the amount of fuel available for the gaseous reaction mechanism. The iterative procedure is shown in figure 4.4. The unevaporated spray is assumed not to play any part in the mass or energy balances in the reactor, and passes out with the product stream.

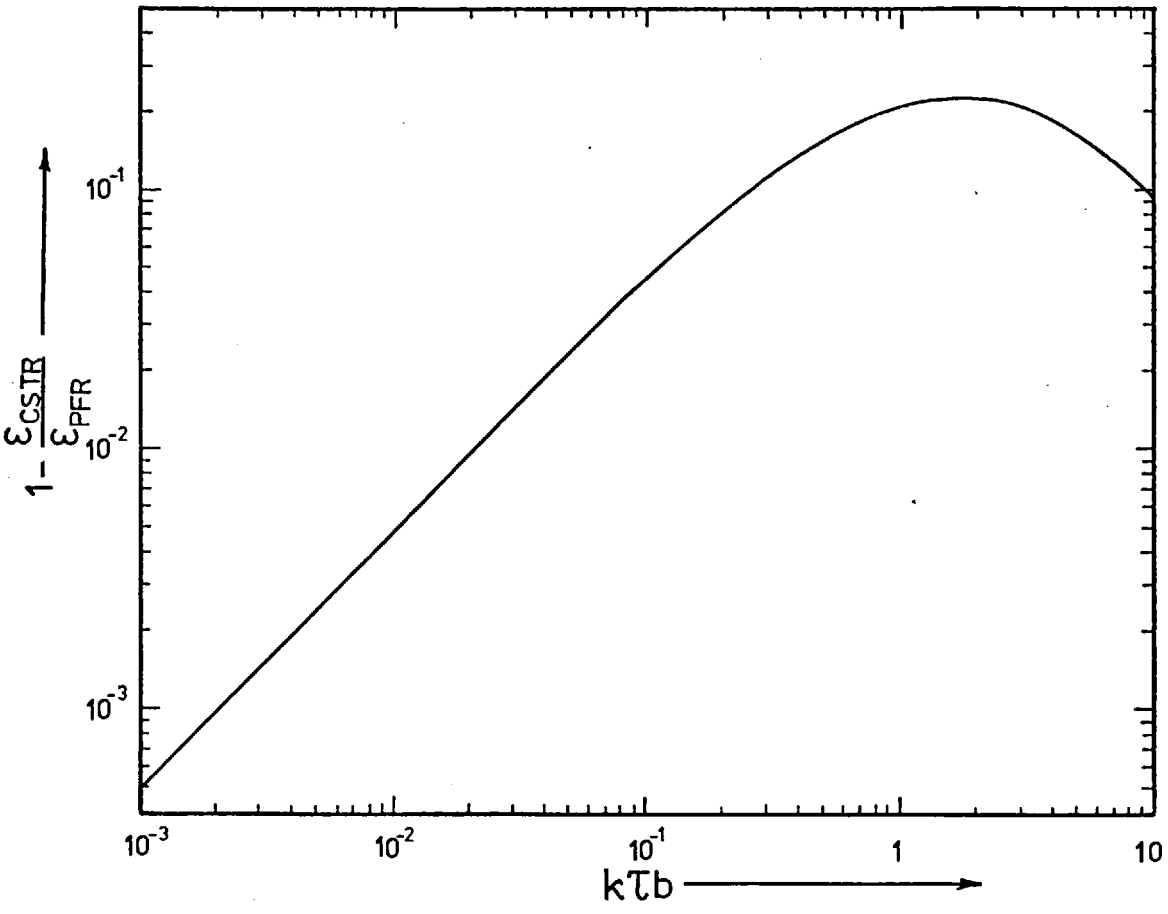

FIGURE 4.3 Fractional difference between evaporative efficiency of CSTR and PFR elements.

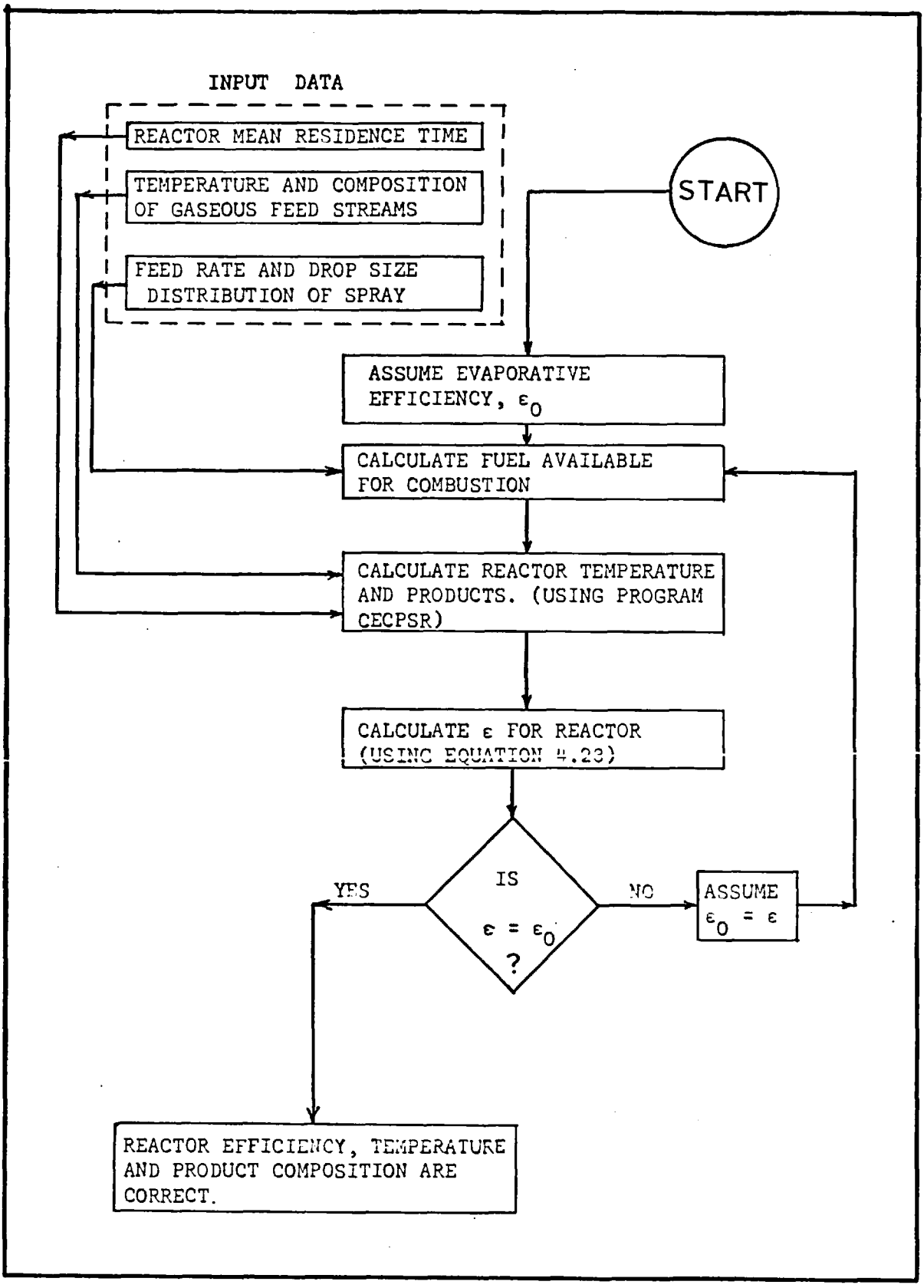

Figure 4.4 Iterative Procedure for Calculation of Spray Combustion in a CSTR

Conservation equations may be written as follows:

For each molecular species considered,

$$\begin{array}{c}\text{net rate of disappearance}\\ \text{of species in CSTR}\end{array} = \begin{array}{c}\text{inflow rate}\\ \text{of species}\end{array} - \begin{array}{c}\text{outflow rate}\\ \text{of species}\end{array} \qquad (4.29)$$

and for energy

$$\begin{array}{c}\text{net rate of heat}\\ \text{loss from CSTR}\end{array} = \begin{array}{c}\text{inlet enthalpy}\\ \text{flow rate}\end{array} - \begin{array}{c}\text{outlet enthalpy}\\ \text{flow rate}\end{array} \qquad (4.30)$$

These equations are non-linear due to the non-linear reaction rate terms which appear in the species equations. A multiple step kinetic mechanism for all the reactions assumed to be taking place together with numerical values of the associated reaction rate constants are required for solution of the equations.

Pratt (76) has published a computer program 'CECPSR' which solves these "non linear algebraic equations describing steady flow, multi-component, chemically rate-limited homogeneous combustion reaction in a micromixed perfectly stirred reactor". A complete write up of the program is presented in Pratt's report (76) and only some or the more important features will be discussed here.

CECPSR solves the equations using a Newton-Raphson iteration technique suggested by Jones and Prothero (77). As an initial estimate for the iteration, the chemical equilibrium solution for the reactor is calculated using the NASA program described by Gordon and McBride (78), this corresponding to the point of zero $1/\tau$ (loading) in figure 4.1(b). Following this a "near equilibrium" solution is calculated for a very small loading before proceeding along the top branch of figure 4.1(b) to the loading (or temperature) specified by the user. The program can be used to calculate the reactor conditions for up to 26 specified values of loading or of temperature at any one specified pressure. Alternatively, a number of points along the top branch (stable combustion) of figure 4.1 may be calculated up to and including the blow-out point. This is sometimes referred to as the blow-out curve.

The first set of input data to program CECPSR specifies the reactor itself in terms of input streams (temperature, enthalpy and relative amount of each component), operating pressure and mean residence time (or loading) for which a solution is required. For calculation of the complete blow-out curve, loading values are internally generated in turn and the solution found for each until blow-out is reached.

Available options which were used include consideration of ionic species and a pyrolysis assumption (see section 3.5) which converts hydrocarbon fuel instantaneously to carbon monoxide and hydrogen, which proceed to react according to the specified kinetic mechanism.

The detailed kinetic mechanism and associated rate constants constitute a second set of input data to be supplied.

A feature of the program is its thermodynamic data file for a comprehensive list of combustion reactants, intermediates and products.

This program was implemented on a CDC 6600 computer and used for calculation of all the combustion reactions in a CSTR reported in this work. The options described above were used, and the mechanism and rate constants used were those given in Table 3.1.

4.6: Theoretical Results for Spray Combustion in a Continuous Stirred Tank Reactor

The effects of some basic parameters on spray combustion in a CSTR will be described. The system used for the example is a gas oil ($CH_{1.83}$) spray whose drop size distribution is described by equation 3.1 (with an evaporative mean diameter of 52 μm) oxidised by air at a pressure of 1 bar. These parameters correspond with those of the experimental system described in chapter 5.

The independent variables varied in the investigation are:

(i) the equivalence ratio, defined as

$$= \frac{(\text{fuel/air})_{\text{actual}}}{(\text{fuel/air})_{\text{stoichiometric}}}$$

(ii) the CSTR mean residence time

and (iii) the inlet air temperature.

The effects of the above on one or more of the following are presented:

(a) Reactor temperature.

(b) Evaporative efficiency.

(c) Reactor products, including nitric oxides.

and (d) Combustion stability.

All the results have been calculated by the method described in section 4.5. Appendix E contains detailed examples of such calculations.

Note that ϕ is calculated on the basis of evaporated fuel in all cases, and that the air feed temperature is 298°K unless otherwise specified, and the spray feed is at 298°K in all cases.

4.6.1: Effect of Equivalence Ratio and Mean Residence Time on Reactor Temperature

The effects of variations in ϕ and τ on temperature are shown in figure 4.5. These follow the trends that would be expected. As residence time increases, the reactants have longer to approach equilibrium and the temperature increases. Once there is sufficient time for equilibrium to be approached, the temperature is not sensitive to any further increase in time. This is shown by the reduced difference between the upper two curves, compared with that between the lower two curves on figure 4.5. The small difference between the upper two curves indicates that equilibrium temperature is approached for mean residence times as low as 0.01 seconds. Maximum temperature for a given value of τ is attained at slightly fuel rich ($\phi > 1$) conditions, the precise value of ϕ varying with τ.

4.6.2: Effect of Equivalence Ratio and Mean Residence Time on Evaporative Efficiency.

The evaporative efficiency of a CSTR, given by equation 4.23 is related explicitly to the mean residence time, τ. Its dependence on ϕ, however, is through the drop evaporation constant K, which is a function of the temperature as determined by τ and ϕ (see previous section).

Figure 4.6 shows the variation of ε with both ϕ and τ. The locus of the blow-out condition as ϕ changes is also shown.

4.6.3: Effect of Equivalence Ratio and Mean Residence Time on Product Composition.

Detailed results of calculations of product composition will be presented for values of ϕ of 0.75, 1.0 and 1.25 (representing fuel lean, stoichiometric and fuel rich conditions, respectively) for values of τ between 0.001s and 1.0s, covering the range relevant to practical high intensity combustion systems.

For a given τ and ϕ, the predicted product composition is determined entirely by the chemistry; i.e. the reaction mechanism and kinetics. The interaction between combustion chemistry and spray evaporation has been covered in section 4.5, the value of ϕ being determined by the fraction of fuel evaporated from the spray when the iteration (figure 4.4) converges.

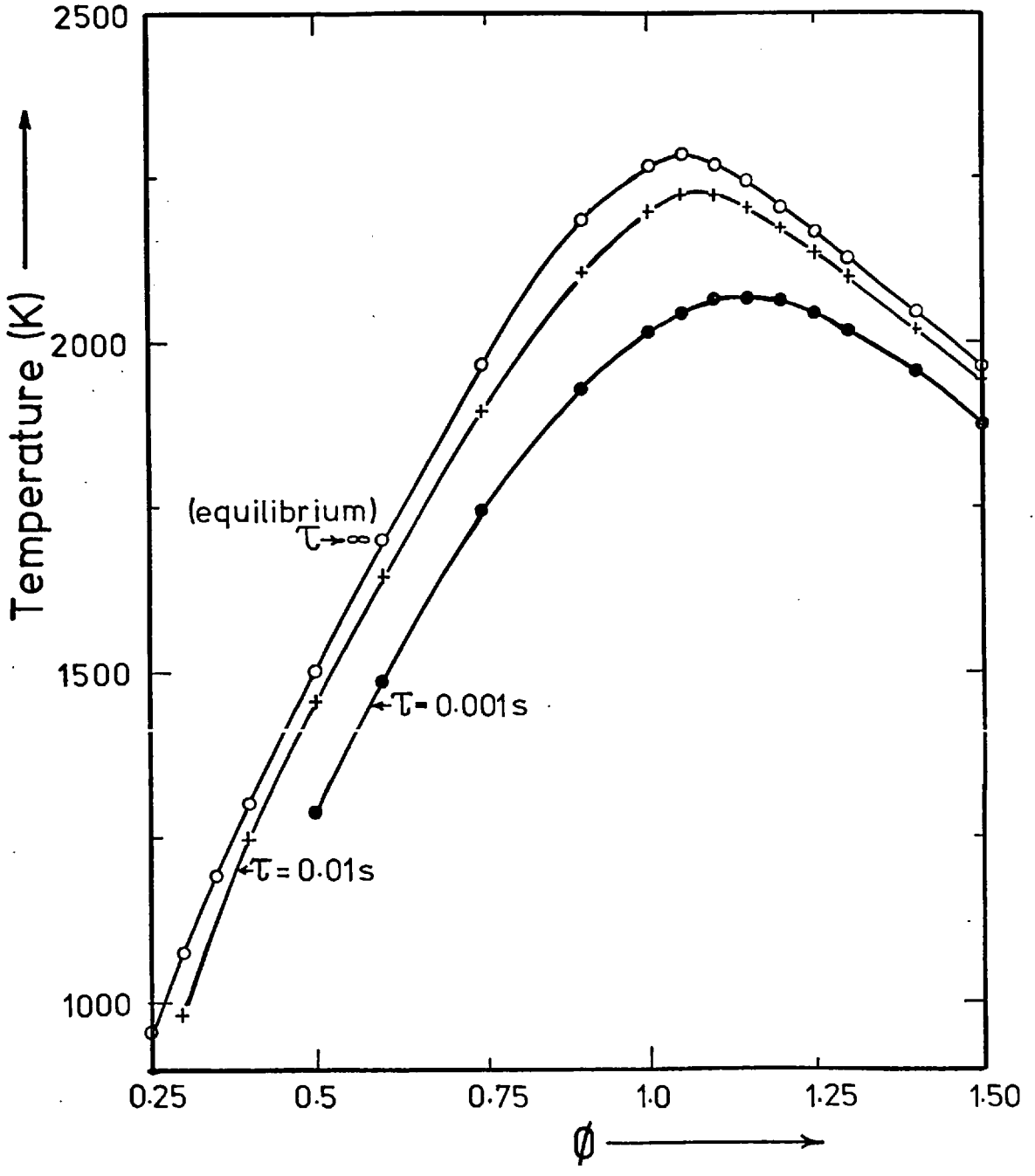

FIGURE 4.5 Effect of CSTR equivalence ratio and mean residence time on temperature.

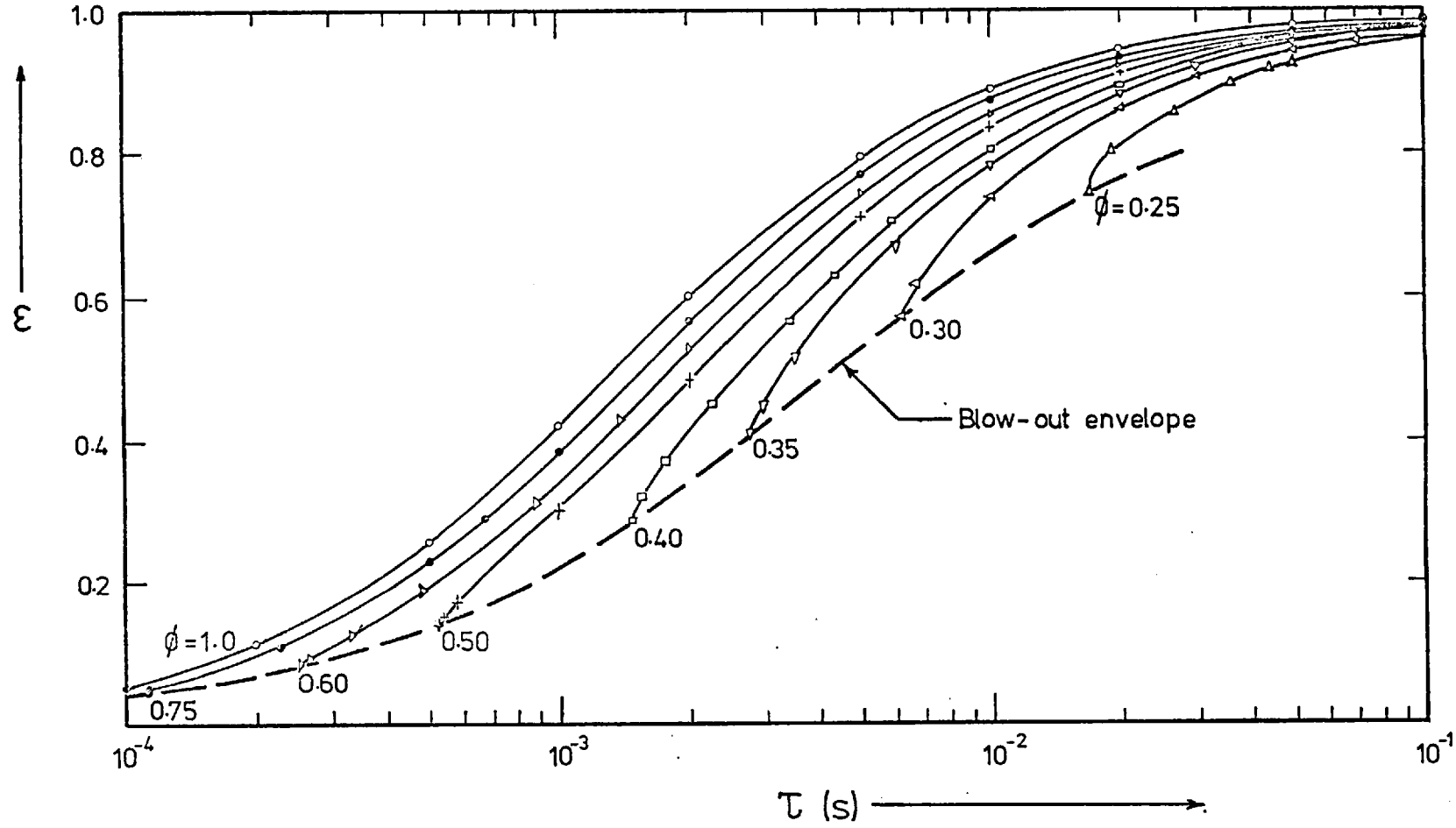

FIGURE 4.6 Evaporative efficiency of a CSTR as a function of mean residence time and equivalence ratio.

The combustion chemistry has been modelled by assuming instantaneous fuel pyrolysis to carbon monoxide and hydrogen, and subsequent reaction by the mechanism and at the rates given in Table 3.1.

For each of the above values of ϕ, figure 4.7 shows the variation with τ of the mole fractions of product species not involving nitrogen atoms, while figure 4.8 shows that for nitrogen containing species (except N_2, which remains essentially constant for all τ).

Comparison between parts (a), (b) and (c) of figures 4.7 and 4.8 is instructive in elucidating the effects of ϕ on the relative rates of the competing reactions.

The expected effect of ϕ on oxygen mole fraction is clearly shown, with both the O_2 and O mole fractions decreasing with increasing ϕ, for any given value of τ. This will affect the kinetics of any reactions dependent on O_2 and/or O, such as nitric oxide formation, and will determine to some extent (depending on other factors) how ϕ affects such oxygen dependent reactions.

The kinetics of all reactions are determined by the temperature, so that the value of ϕ has an indirect effect on kinetics through its effect on temperature as shown in figure 4.5. Figures 4.7 and 4.8 show that at $\phi = 1$ (where temperature is high relative to $\phi = 0.75$ and 1.2), the species concentrations approach closer to their equilibrium values than at $\phi = 0.75$ and 1.25, for reactors with equal mean residence times. Similarly, the approach to equilibrium is more rapid at $\phi = 1.25$ than at $\phi = 0.75$, corresponding to the relative temperatures at these two conditions. The clearest indication of these temperature dependent trends is obtained by comparing the values of the nitrogen species mole fractions at $\tau = 1$ with their respective equilibrium values at each of the values of ϕ in figure 4.8.

The practice of decoupling hydrocarbon from NO_x kinetics in post-flame reaction zones has been discussed in section 3.6, and the non-validity of this approach for (CSTR) zero-dimensional reactors explained. Figures 4.7(a), (b) and (c) clearly show that super-equilibrium levels of O, OH and H species indeed exist at values of τ of practical interest, so that the entire mechanism must be considered simultaneously.

Figure 4.8 indicates that the level of NO produced is at least one order (and typically two to three orders) of magnitude greater than all the other oxides of nitrogen, so that the NO mole fraction adequately represents the total nitrogen oxides.

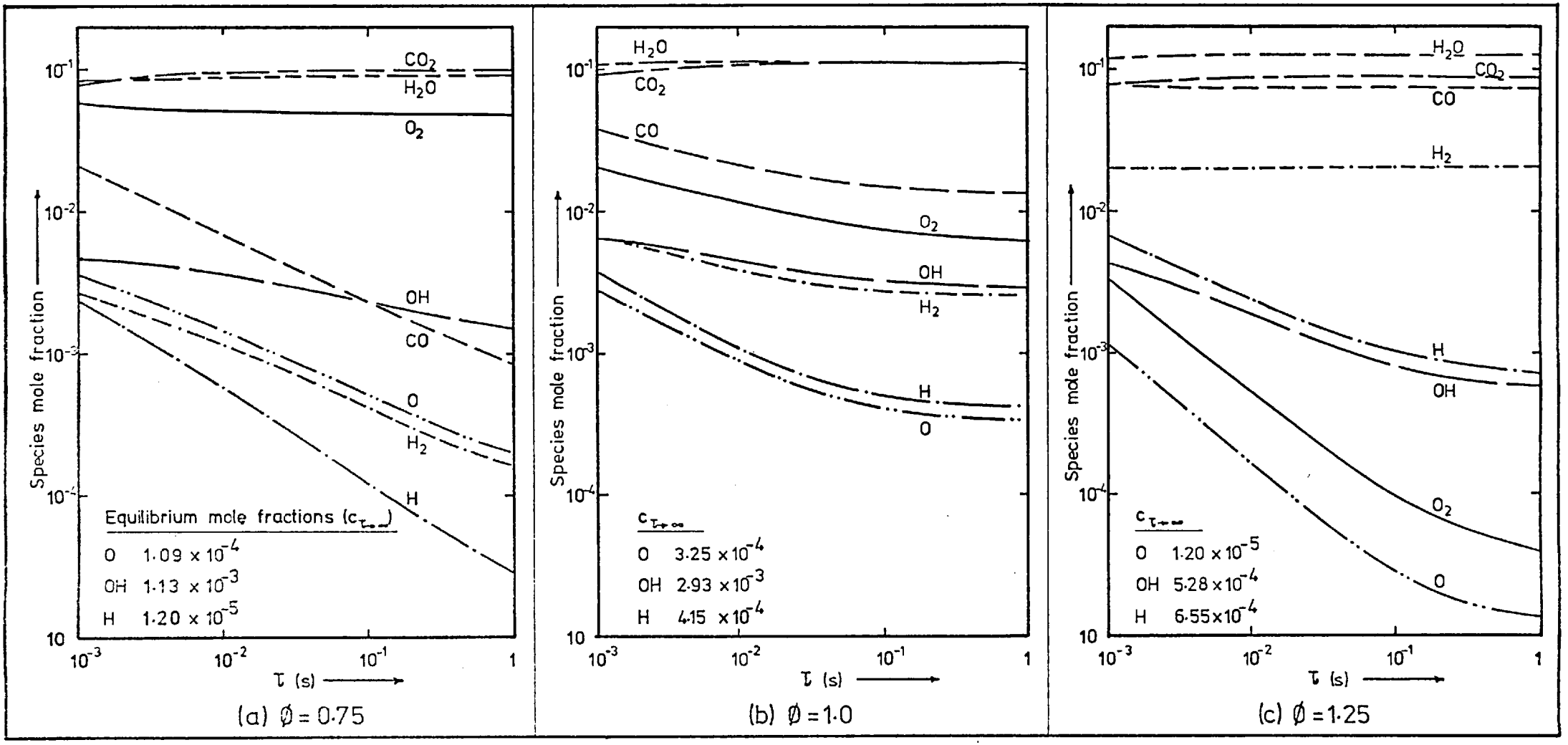

FIGURE 4·7 Carbon-hydrogen-oxygen species concentration in a CSTR as a function of mean residence time and equivalence ratio.

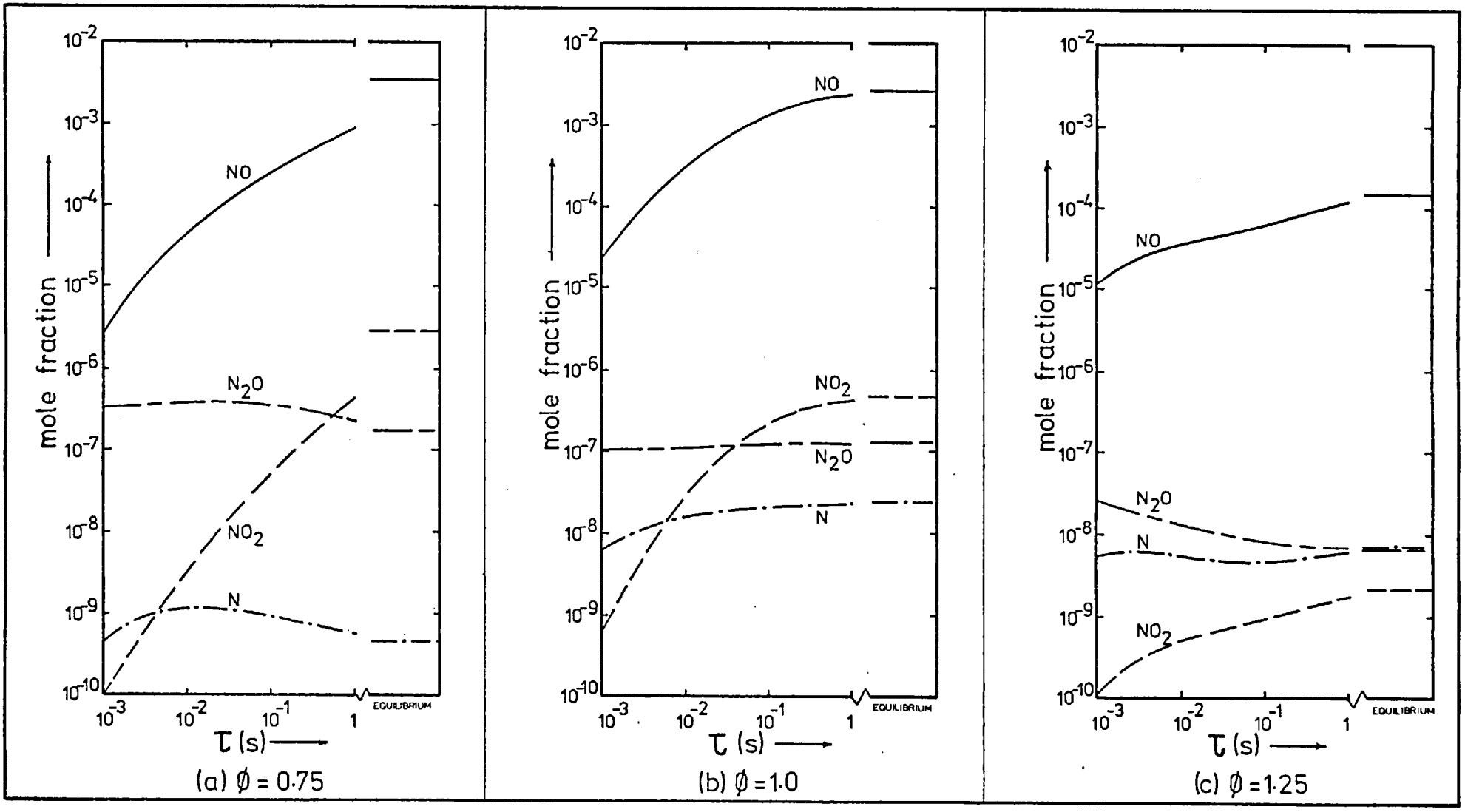

FIGURE 4.8 Nitrogen species concentration in a CSTR as a function of mean residence time and equivalence ratio.

Figure 4.9 shows NO mole fraction for two additional as well as the three above values of ϕ, and these confirm the trends of figure 4.8.

From Table 3.1 it can be seen that many of the reactions producing NO depend on O atom concentration. In particular, in the first reaction of the Zeldovich mechanism ($O + N_2 = NO + N$) O atom concentration is controlling. This reaction has a high pre-exponential factor for its kinetic rate and is therefore important at temperatures sufficiently high to balance its large activation energy. This is confirmed by comparing figures 4.8(a) and (c). Temperature at $\phi = 1.25$ is greater than at $\phi = 0.75$ so that for small τ (O atom concentrations are similar) more NO is produced at $\phi = 1.25$. At larger τ the influence of greatly reduced O atom concentration at $\phi = 1.25$ limits NO production, the rate of increase of which is considerably reduced as τ increases. For $\phi = 0.75$ the rate of increase of NO is not limited by low O concentrations and continues with increasing τ. The identical argument explains the relative NO emissions at various values of τ for $\phi = 0.50$ and $\phi = 1.50$.

For fuel rich conditions where O atom concentration is very low and the temperature somewhat reduced, the reaction

$$N + OH = NO + H$$

would account for relatively more of the NO produced that at stoichiometric or fuel lean conditions.

4.6.4: Effect of Feed Temperature on Combustion Stability. Consideration of figures 4.1(a) and 4.1(c) shows that an increase in the temperature of the feed stream would be expected to allow a higher throughput (lower τ) before the onset of blow-out. Results plotted in figure 4.10 show that this is predicted by the model used. As ϕ increases, the effect of increasing the feed temperature diminishes slightly, due to the increase in reactor temperature with ϕ. Values of ϕ between 0.25 and 0.40 are chosen because for equivalence ratios nearer stoichiometric the mean residence times at blow-out are extremely low and are much less than those of practical interest.

It must be stressed in this section that the model used does not account for any mixing non-uniformities as it assumes the CSTR to be micromixed. This assumption, if it is not accurate, may lead to serious errors in estimation of blow-out conditions. Swithenbank (54) discussed this effect and showed that for near stoichiometric

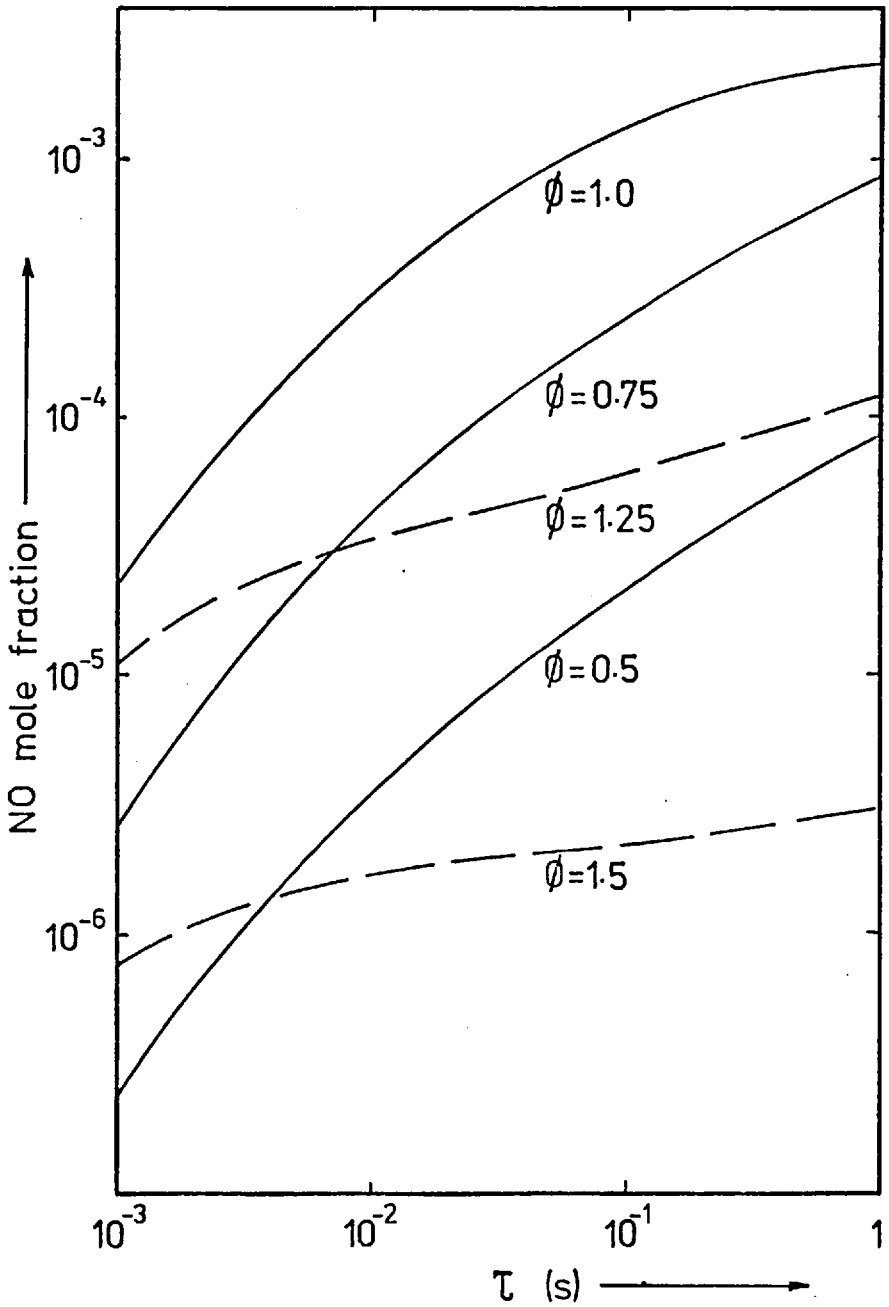

FIGURE 4.9 Nitric oxide emissions from a CSTR as a function of mean residence time and equivalence ratio.

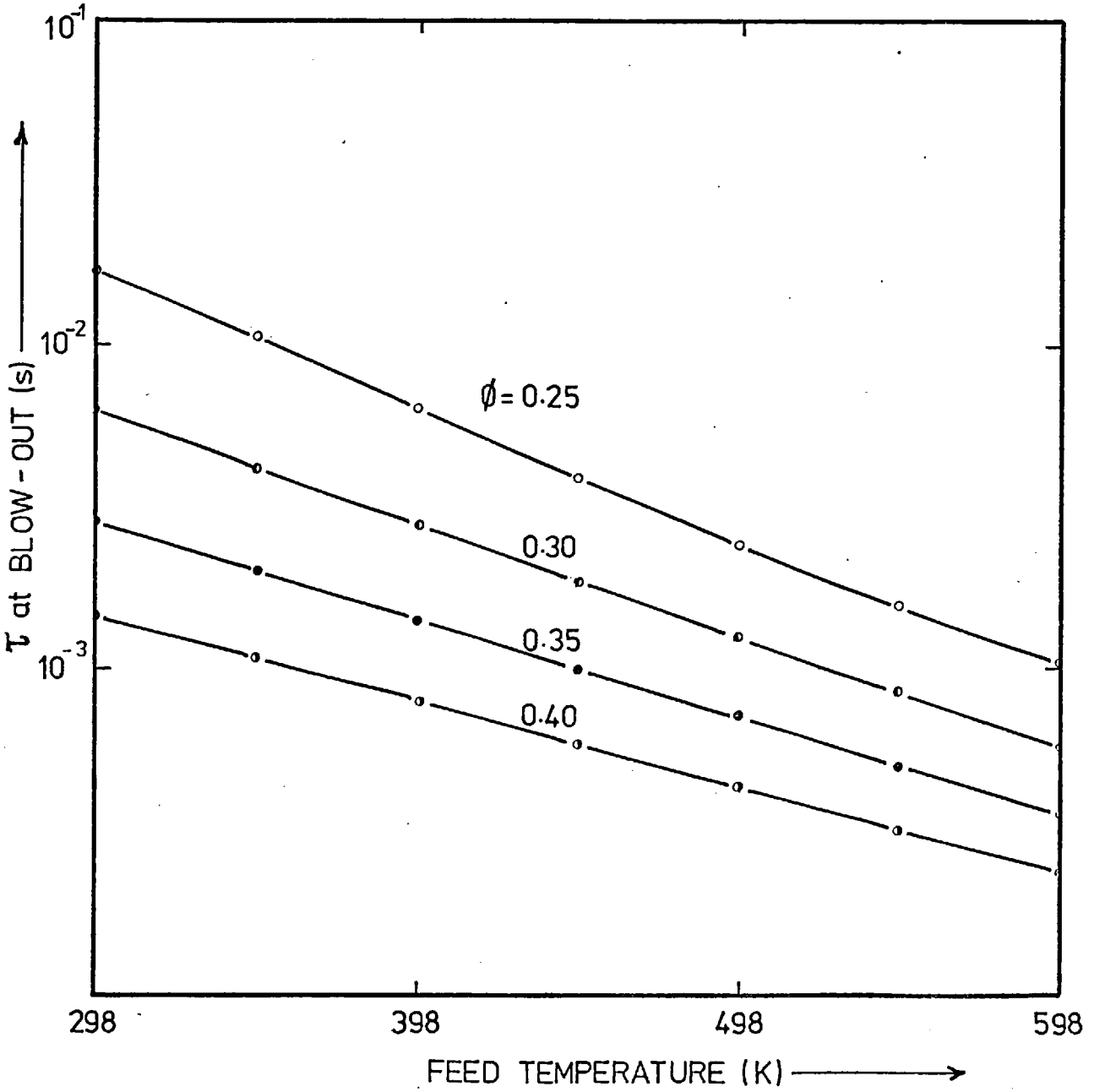

FIGURE 4.10 Effect of feed temperature to a CSTR on mean residence time at blow-out.

5. DESCRIPTION OF THE COMBUSTION SYSTEM USED

5.1: System Configuration

A flow diagram of the combustion system appears in figure 5.1. The details of the combustion chamber and atomiser are discussed in the following sections.

The gas oil fuel was delivered to the atomiser by a swash-plate positive displacement metering pump.

Primary air (atomising air) was supplied at 4 g/s and 2 bar by a Bullows Rotary Vane compressor with integral receiver and pressure control valve and passed through a rotameter, the pressure being measured on a gauge just downstream of the rotameter.

Secondary air was supplied by an Osmund blower [delivering up to a total of 30 g/s at 30" w.g. (107.5×10^3 N/m^2)] and fed separately to each half of the chamber casing. The flow through each pipe was measured by a calibrated venturi meter upstream of a valve which was used to adjust the air flow to each half of the chamber casing.

On leaving the chamber the combustion products pass through a water cooled cross piece used for sampling and then through a water spray cooling section, and a cyclone before passing out to the atmosphere through a stack.

One opening of the sampling cross-piece was used for the sampling valve described in chapter 6 and the other for a steam cooled stainless steel sampling probe leading to a chemiluminescent NO_x analyser. Pressure gauges indicated the pressures in the sight glass tube shown in figure 5.2, and the forward and reverse chamber casing.

Thermocouples were inserted at the points shown in figure 5.1, and the outputs continuously recorded on a sixteen point recorder (Honeywell, Elektronic 15).

The thermocouple readings were used to adjust venturi meter and rotameter calibrations as necessary and to monitor the cooling water outlet temperature. When starting up the system, or changing an operating parameter from one setting to another, steady operation was indicated by constant thermocouple outputs and steady pressure and flow readings. Changes in one parameter tended to result in adjustment of another due to feedback either through the combustion process or, in the case of forward and reverse secondary air because of a common supply. Experience was required to achieve desired settings quickly, as feedback through the combustion

conditions, unmixedness leads to an increase in τ at blow-out, while at lower or higher ϕ unmixedness actually allows a decrease in τ (increased throughput) before blow-out is observed.

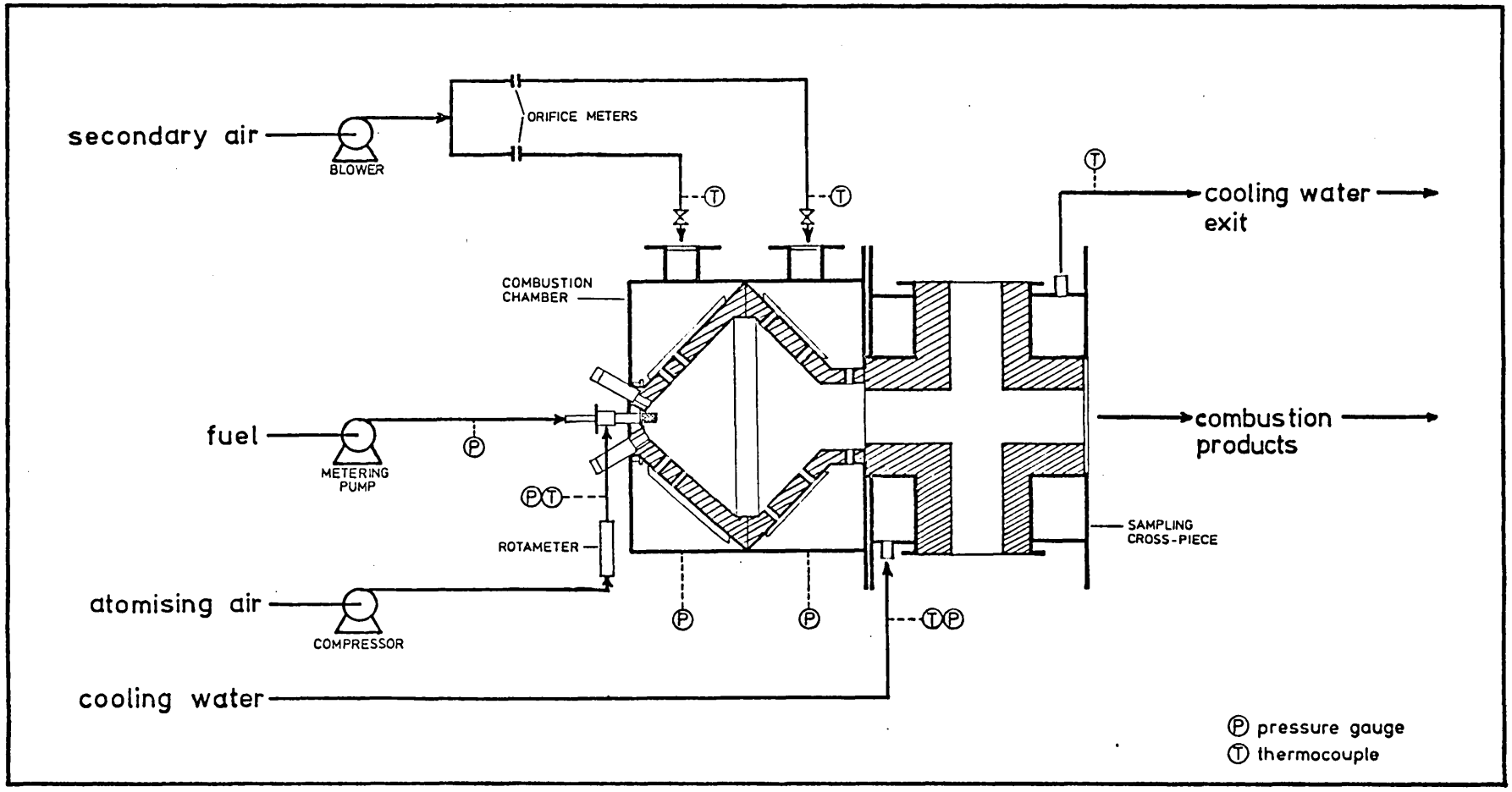

FIGURE 5.1 Flow diagram of combustion system used.

process could take a long time due to thermal inertia, the system taking up to twenty minutes to settle down to steady operation.

5.2: The Combustion Chamber and Sampling Cross-Piece

The combustion chamber was designed and fabricated by Urquhart's (1926) Ltd. for high intensity combustion of liquid fuel.

Figure 5.2 shows relevant features of the chamber design. The chamber consists of two co-axial refractory lined conical frustra joined at their bases and mounted inside a lagged cylindrical casing. Rows of $\frac{1}{8}$" (3.18 mm) ceramic nozzles radially disposed in the cones feed the secondary air into the chamber, after it has cooled the refractory cone.

The chamber was fitted with two identical tubular openings on each side of the atomiser port. One was used for holding a pyrotechnic ignition device and the other was used as a sight tube for visual observation of the combustion space. A flame failure device was available for use through the sight tube but was not utilized as the system was never left running unattended, any irregularities being immediately registered on the pressure and temperature measuring devices.

The sampling cross-piece was a water-cooled refractory lined cylinder with its axial 3 inch (76 mm) diameter tube immediately downstream of and in line with the chamber exit. It had two opposing, radial 3" (76 mm) diameter sampling ports in the horizontal plane which were fitted with flanges for leak free insertion of sampling probes etc. Figure 5.1 shows the relative positions of the chamber and cross-piece.

5.3: The Atomiser

The atomiser used was an Urquhart's Mark IV Number 2 twin fluid atomiser, and is shown in figure 6.6.

The design of a high intensity combustion chamber is inextricably connected with the characteristics of the spray produced by the atomiser, in respect of drop size distribution as well as spatial distribution of the spray.

5.3.1: Drop Size Distribution. The atomiser could be used with a number of different shims which regulate the annular cross-section through which the atomising air is metered. The mass flowrate of atomising fluid is determined by the shim size and the supply pressure.

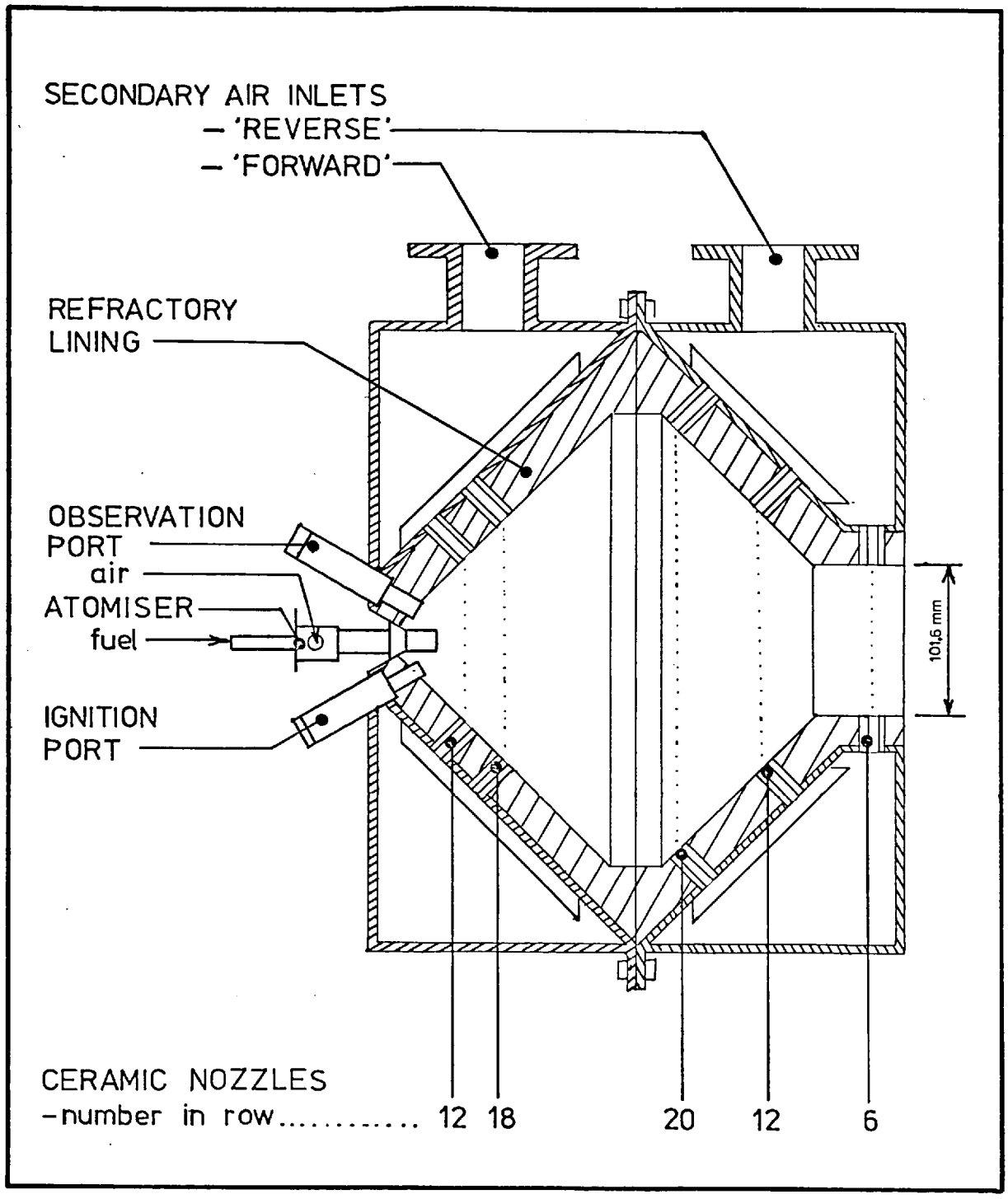

FIGURE 5.2 The high intensity spray combustion chamber used.

The effect of atomising fluid pressure has been shown by Fraser (9; p.698) to be important in determining the drop size. As a result of this a minimum atomizing pressure of 15 psig (2 bar) was used to ensure efficient disintegration of the liquid fuel.

Another parameter which is important in determining the drop size is the air/liquid mass ratio (9; figure 11). To ensure that the spray surface mean diameter was below 70 μm, an air/fuel ratio of 2 was used in all experiments. The fuel firing rate used was 2 g/s, so that 4 g/s of air was used to maintain a constant spray drop size distribution.

The requirements of 4 g/s air at a minimum of 2 bar supply pressure for the atomiser dictate that a shim length of 0.263" (6.68 mm) be used. Larger shims resulted in increased airflow at the above pressure, or lower pressure for the same air flow.

Under different operating conditions it was found that different upstream pressures were required to produce 4 g/s flow through the above shim. This was attributed to expansion effects due to the varying amounts of heat radiated back to the atomiser from the chamber and the resulting different steady state temperature reached.

Fraser and Eisenklam (10, figure 14) present results of drop size distributions obtained from an atomiser of the type used. The distribution obtained for the conditions closest to those used is shown in figure 5.3.

For the purposes of the theoretical analysis it is desirable to express the spray drop size distribution in the form given in equation 3.1. This is basically a one parameter equation, the parameter, b, being effectively a measure of the evaporative mean diameter as shown by equation 4.18.

The value of b to give a best fit to the experimental data is also shown in figure 5.3. Statistically, the equation satisfied 95% confidence limits for 10 degrees of freedom, and this was considered reasonable especially in view of the uncertainties connected with experimental drop size determination.

Ideally, it is necessary to know the drop size distribution actually produced in the chamber, and, of course, to fit this distribution accurately. A possible way of dealing with general distributions not accurately fitted by the single parameter equation is discussed in chapter 9.

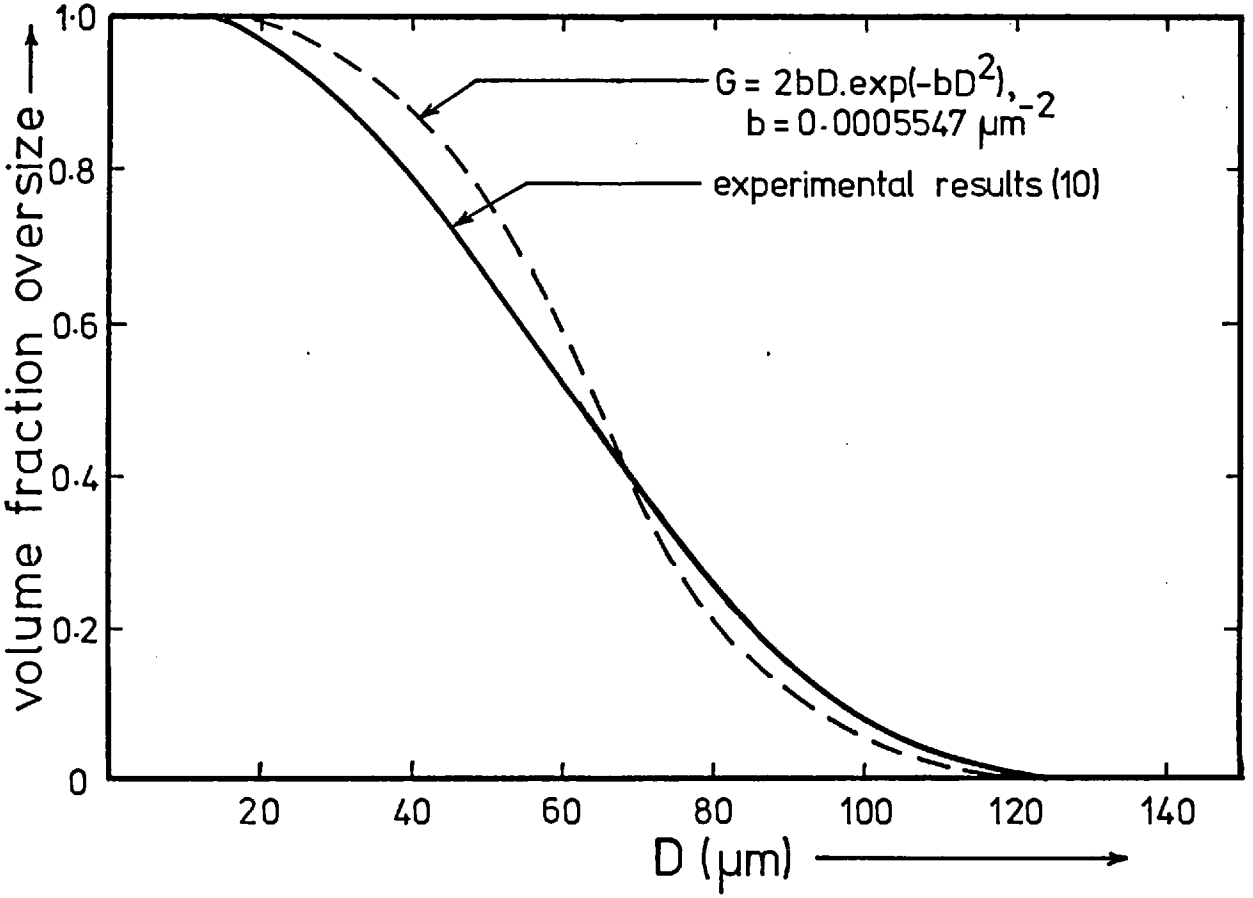

FIGURE 5.3 Spray drop size distribution.

5.3.2: Spatial Distribution of Spray. The spatial drop size distribution is determined by the angle of the spray cone, and its momentum relative to the surroundings (i.e. chamber geometry and pressure and momenta of any other interacting streams).

The most important parameter determining the spray cone angle for a given twin fluid atomiser was found by Fraser (9) to be the ratio of swirl momentum to forward momentum.

The cone angle of the air jet was measured for varying air pressure and shim size (with no liquid flow). The cone angle was insensitive to air pressure for pressures between 10 and 20 psig (0.7-1.4 bar), but decreased with decreasing shim size.

For the shim size used in the experiments, the cone angle was found to be 40°. This is very much less than the 90° spray cone angle around which the chamber was designed, but was nevertheless used to comply with the drop size distribution requirements. The very low cone angle may be explained by the observation that for the small shim size used it was possible for some of the air to bypass the swirlers thus reducing the swirl/forward momentum ratio and hence the cone angle. Figure 5.4 shows how this bypass comes about.

Consequently, the momentum of the spray is effectively entirely in the axial direction, and this assumption is made in Appendix F where the momenta and kinetic energy ranges of various streams in the chamber are calculated.

5.4: Measurement of Nitric Oxide Emissions

Nitric oxide emissions from the combustion chamber were measured by withdrawing a sample from the exit stream at the sampling cross piece.

A steam-cooled stainless steel probe with a $\frac{1}{8}$" (3.18 mm) diameter sample tube was used and the sample passed through a glass wool filter and a bed of silica gel to remove particulates and moisture respectively before being drawn into a chemiluminescent NO_x analyzer, which was calibrated with a 100 ppm NO standard mixture. The tubing used in the system was made of stainless steel (for the probe), glass (for the treatment sections) and teflon (for the analyzer input) to reduce changes of NO_x concentration due to catalytic reactions on the tube walls, which are known to occur in the presence of copper.

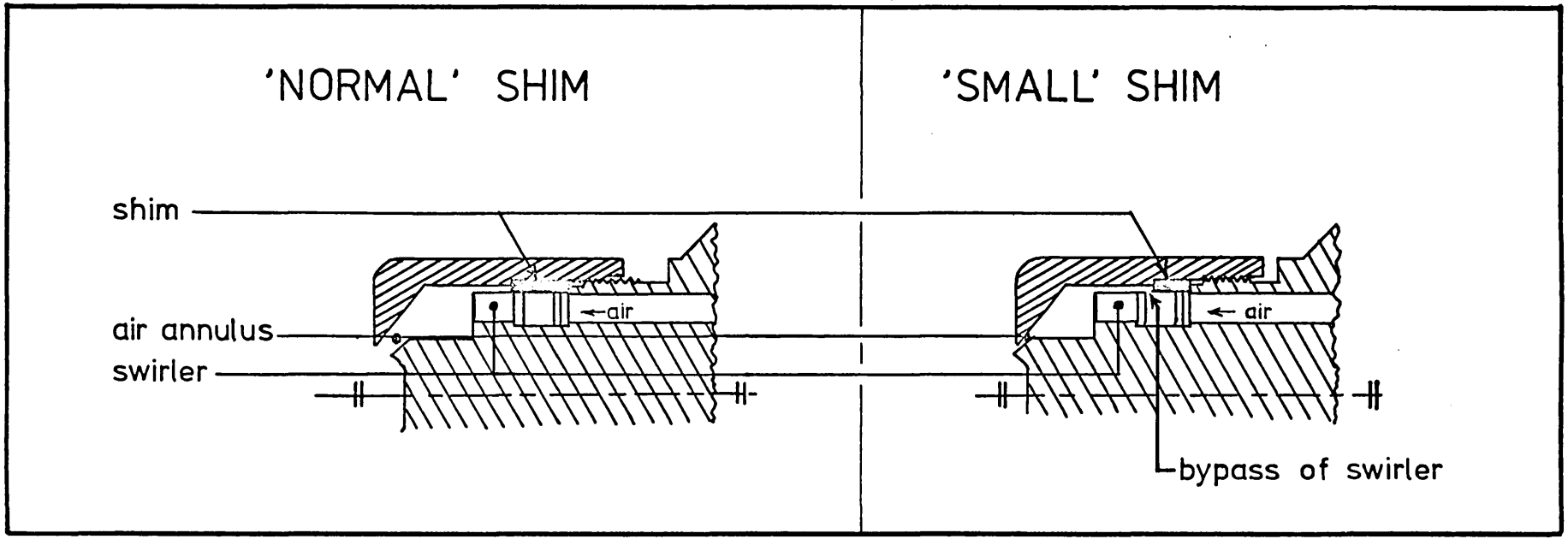

FIGURE 5.4 Bypass of atomiser swirlers resulting from small shim size.

6. EXPERIMENTAL DETERMINATION OF RESIDENCE TIME DISTRIBUTION

This chapter will discuss the determination of RTD in high intensity combustion chambers, with particular reference to the chamber used in the experimental work and described in chapter 5. Some points common to chambers in general will be discussed first, followed by problems specific to accurate RTD determination for systems with very short mean residence time, such as high intensity combustion chambers.

An experimental approach which makes accurate RTD determination possible for high intensity chambers under operating conditions will be presented. The experimental method and equipment used to put this approach into practice are then described in detail.

6.1: Residence Time Distribution in Combustion Chambers

Combustion chambers generally have a number of feed streams (inputs) and one product stream (output). The multiplicity of inputs is designed to provide a mixing and flow pattern conducive to the attainment of satisfactory combustion performance.

The presence of multiple input streams requires care in the definition of a chamber residence time distribution (RTD). The RTD for the feed entering through one inlet, will, in general, be different from that coming through any of the other inlets.

The aim of the tracer experiments is to deduce a flow configuration of reactor elements equivalent to that present in the chamber under operating conditions, so that the combustion process may be modelled. In the case of chambers with one twin fluid atomiser fuel enters with the atomising fluid and may reasonably be assumed the limiting reactant, as it does not reach all parts of the chamber. In the present context fuel relates to liquid fuel drops as well as the unreacted/reacted vapour air mixture. Combustion can only take place in the regions reached by the fuel, and it is the passage of the fuel through the chamber that tracer is required to follow. In the chamber used for the experiments it will be assumed that the liquid fuel spray is a dilute suspension of drops moving with the atomising fluid and vapour (i.e. drops are so small that their Reynolds number is effectively zero). A gaseous tracer injected into the atomising fluid will therefore trace the fuel spray and its products as required. The RTD as determined in this manner is that of the reactor flow configuration of the chamber.

The secondary air inputs to the chamber will each have an RTD which may be measured independently (79; p.1261). Changes in one or more of the inputs may result in changes to the RTDs of other inputs depending on the way in which each input enters the overall flow configuration.

In the experimental program to be described, the RTD of the atomiser input was measured for a number of different secondary air inputs. The way in which the secondary air inputs enter the reactor flow configuration was decided on the basis of chamber geometry. RTD experiments on the forward and reverse secondary air inputs could have verified the parts of the reactor flow configuration through which each of these inputs passes.

The flow configuration in the parts of the chamber not reached by any fuel cannot be deduced without RTD experiments on the other inputs, but as no reaction can take place in these regions, knowledge of the flow there is not directly relevant to modelling of the combustion process. The dead volume of the chamber - space which is not used for the combustion process - can be deduced from the combustion model and the total chamber volume (as shown in Appendix E) and is a measure of the under-utilization of the chamber volume.

6.2: Selection of a Suitable Tracer

As discussed in chapter 2, stimulus response experiments carried out by measuring the input and output concentration-time curves of a pulse tracer can be used to characterize the flow configuration in a system. Experimentally, certain requirements must be met for the results to accurately represent the actual residence time history of the system.

The main requirement is that the tracer used accurately follows the stream being traced through the system, without itself affecting the flow or being adsorbed. This requirement usually dictates that gaseous tracers be used for gaseous systems, as particles are unable to undergo sudden velocity changes due to their inertia. By extension of the same argument, the diffusivity of the tracer should be the same as the fluid being traced so that radioactive isotopes of the fluid would be an ideal tracer.

The specific activity of radioactive tracer required for injection was calculated, and it was found that this was more than could be safely used without extensive shielding of the whole system and special facilities for dispersion of the exhaust stream. This approach was therefore abandoned.

A second class of tracer often used is that of the inert gases, the most common being helium and argon. These are stable in the combustion environment and may be detected at very low concentration levels using mass spectrometry. Small quantities are used for each pulse injection, which not only allows the pulse to be relatively short, but keeps the concentration in the chamber down to levels which do not interfere with the combustion processes by diluting the reactants.

Argon would be preferable to helium as its molecular weight and diffusivity are closer to those of the combustion gases, but helium was used because of the availability of a helium leak detector, i.e. a mass spectrometer tuned to detect helium. Under the conditions present in a high intensity combustion chamber it is reasonable to assume that transport by convection and turbulence would be very much greater than that by molecular diffusion, so that the helium would be a suitable tracer in spite of its high molecular diffusivity.

6.3: Dynamic Measurement of Tracer Concentration

Concentration time data for tracer input and output from a system are usually obtained dynamically. A pulse of tracer is injected and a detector is used to continuously monitor and record the tracer concentration variation with time for the appropriate stream(s).

In general a sample is withdrawn continuously from the stream and conveyed in a sampling line to the tracer measuring instrument.

This procedure inherently introduces some distortion of the actual tracer response due to the effect of diffusion in the sampling line and 'averaging' (or time constant) effects of the detector. The importance of these effects depends on their time constants compared to that of the system being measured; for a system with a relatively short residence time, the sharp peak produced by a pulse input will be spread by diffusion in the sampling line and further distorted by the time constant of the detector.

The effect of the sampling line on concentration profile has been discussed by Schefer *et al.* (80) and by Lewis (81) who recommended flow conditions which would minimize distortion due to these effects.

The type of distortion obtained in practice is shown in figure 6.1. Curve 1 is the impulse response of a stirred tank with a plug flow sampling line time delay in series. Curve II shows the effect of time delays in the detector system, which

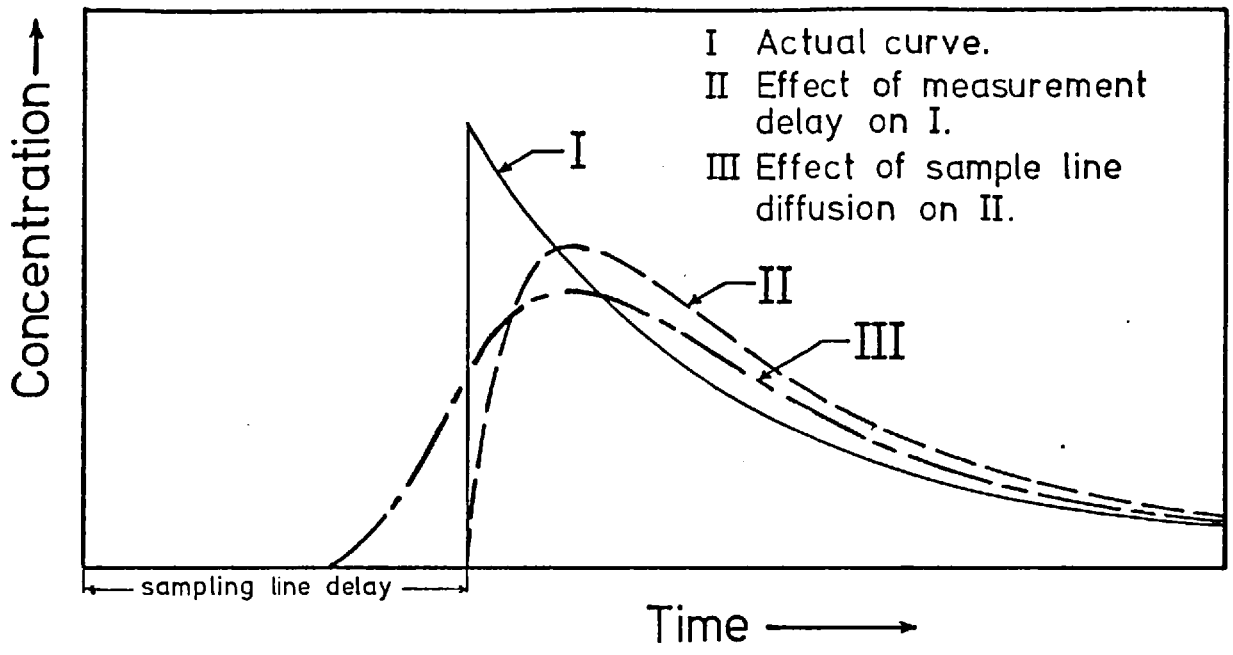

FIGURE 6.1 Effect of measurement delay and sample line diffusion on tracer concentration-time curve.

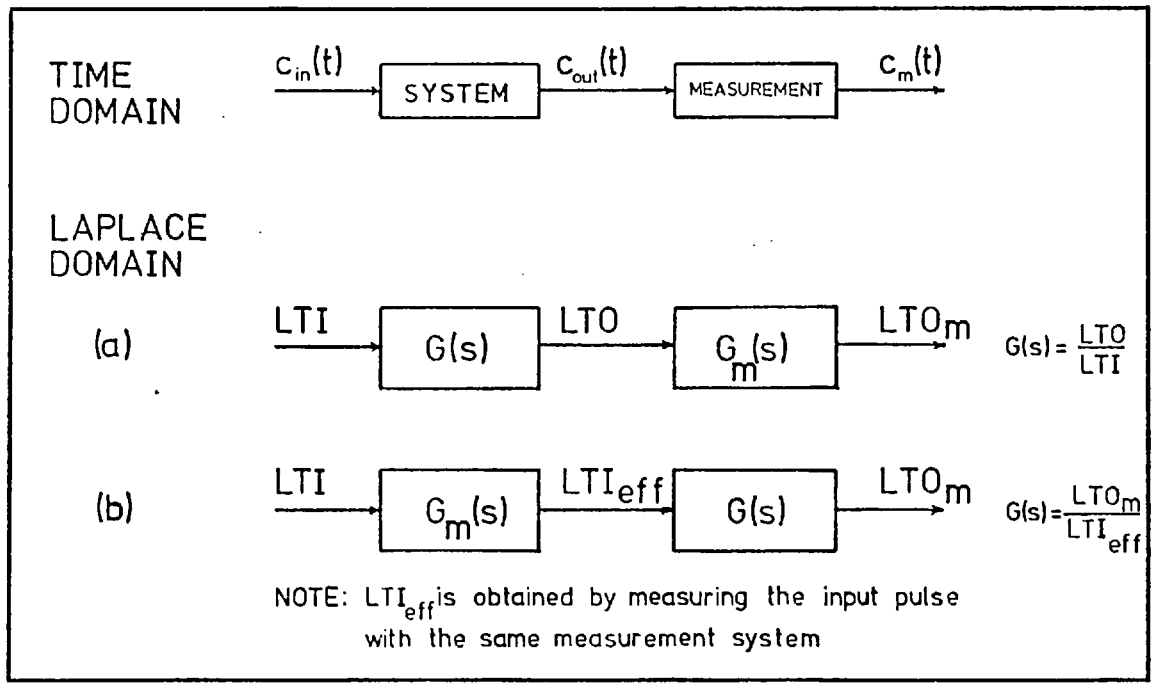

FIGURE 6.2 Effective modification of input resulting from measurement system dynamics.

cannot therefore follow rapid concentration changes accurately. Curve III shows the additional effects of longitudinal dispersion in the plug flow sampling line.

As the time constant of the detection system increases relative to that of the system being identified, the distortion is increased, until in the limit the response obtained approximates that of the detector, and not of the system.

If the characteristics of the measurement system are expressed by means of an overall transfer function $G_m(s)$, figure 6.2 shows that the effect of $G_m(s)$ is to modify the LTI. This is so because the LTO is independent of the order of linear elements in series. Figure 6.2 shows that the effective input to the system being identified, LTI_{eff}, may be considered to be the product of LTI and $G_m(s)$. LTI_{eff} will have a lower value than LTI (for a given s), corresponding to an increase in the effective pulse duration as shown in figure 6.1. The sensitivity of LTI_{eff} to errors in input pulse measurement is therefore also greater than that of LTI as shown in figure 2.8.

The effect of measurement delays may therefore be lumped with those of finite input pulses, and the conclusions arrived at in chapter 2 with respect to the latter may be applied with the modification that the effective mean pulse time $\bar{t}_{p,eff}$ is taken as the sum of $\bar{t}_p$ and the time constant of the measuring system, $\bar{t}_m$

i.e.
$$\bar{t}_{p,eff} = \bar{t}_p + \bar{t}_m \qquad (6.1)$$

The importance of keeping $\bar{t}_{p,eff}$ as small as possible compared with τ, the mean residence time of the system being tested, has been discussed at length in chapter 2. When τ is so small that the response time of an instrument used to measure concentration is inherently greater, dynamic measurement will necessarily result in significant experimental error.

As shown in figure 6.2, $G_m(s)$ is accounted for by obtaining the effective input by measuring the input shape under the same conditions as the output. The effective input is then used to calculate G(s). The assumption here is that $G_m(s)$ remains constant for each measurement. This condition that is difficult to ensure in practice, especially when the allowable error (in say sampling delay time or instrument response) must be small compared to the mean residence time of the system being tested. This measurement error is itself further multiplied when the analysis is carried out in the Laplace domain, due to the increased effective pulse duration and the consequent increase in sensitivity as shown in chapter 2.

6.4: Steady State Measurement of Tracer Concentration by Dynamic Sampling

To overcome the errors introduced by the dynamics of measuring systems in stimulus response experiments, a method of dynamic sampling is proposed as follows.

Consider a hypothetical tracer concentration-time curve of a stream as shown in figure 6.3. If a sampling valve is placed in this stream and made to open and close within a very short time interval it will draw in a sample whose tracer concentration is the time average of that of the stream during the time it is open. If the opening time is very small compared with the time taken for concentration to change, the sampled gas will in effect be the concentration at a point on the curve. However, as the opening time is reduced, so is the amount of sample drawn in. To obtain sufficient sample for analysis it may be necessary to repeat the process a number of times, ensuring that the input pulse shape and the system residence time distribution remain constant and that the sampling valve is opened at precisely the same point on the curve. As many points as are necessary to characterize the curve are determined in turn in the above manner.

The advantage of this system is that the tracer concentration at each point is determined by steady state measurement, so that the actual pulse shape is not distorted by the dynamics of the measurement system.

In practice the input pulse is injected at a frequency of once every t_i seconds, and the sampling valve is operated t_{sd} seconds after the beginning of each pulse injection, until sufficient sample has been collected to measure the tracer concentration at a single point on the curve. The sampling delay, t_{sd}, is then altered and the process repeated for subsequent points. Figure 6.4 shows the relationship between hypothetical input and output curves and sample concentration for one value of t_{sd}.

Clearly the pulse frequency must be such that t_i is sufficient to allow the tracer from the previous pulse to completely leave the system before the subsequent pulse begins to appear at the exit.

Subsequent sections will describe the experimental system developed to carry out stimulus response testing of combustion chambers using the dynamic sampling method.

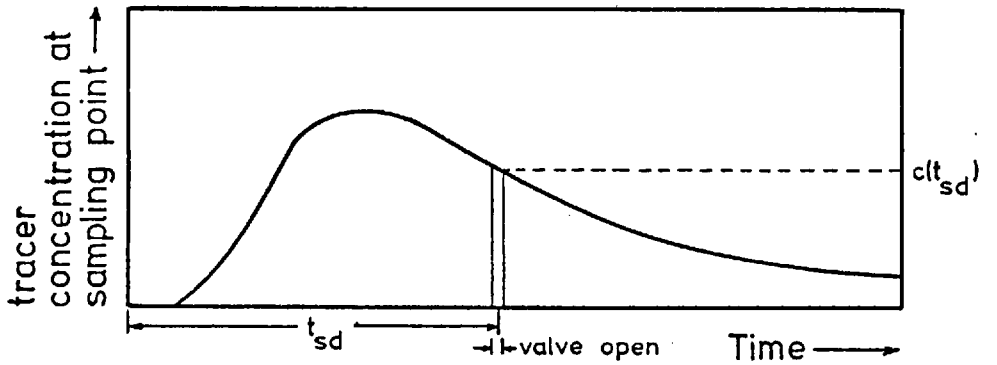

FIGURE 6.3 Concentration sampled by a valve open for a short duration in a stream whose concentration changes with time.

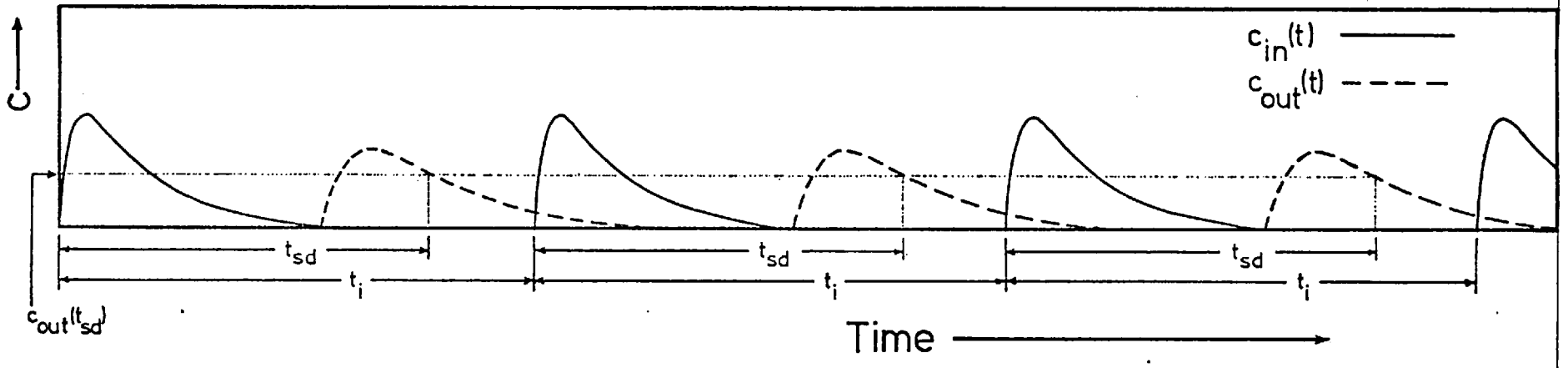

FIGURE 6.4 Injection and sampling at constant frequency and sampling delay

6.5: Description of Experimental System Used for Stimulus Response Tests

This section will describe each part of the experimental system developed and used to carry out the stimulus response experiments on the high intensity combustion chamber used. Following this, the procedure for carrying out such tests will be given.

6.5.1: Control Circuit. The heart of the dynamic sampling system is the electronic circuit which drives the injection and sampling valves at the appropriate frequency and phase difference. This circuit was specially designed and constructed in the Departmental Electronics Workshop to suit the injection and sampling valves used. A diagram of the circuit appears in figure 6.5, and an explanation of its mode of operation is given in Appendix G. The injection and sampling frequency could be set at either 1 or 2 cycles per second and the phase difference, t_{sd}, was continuously variable between 12 and 1112 ms to an accuracy of ±10 μs. The phase difference, t_{sd}, was independently checked throughout the experiments using a digital timer-counter (Advance Electronics TC-7). In practice t_{sd} is measured as the difference in time between the beginning of the drive pulses to the injection and the sampling valves.

6.5.2: Tracer Injection. Helium tracer was supplied from a cylinder at a constant pressure, which could be adjusted by means of a control valve. This was connected by 6.4 mm diameter copper tubing to the injector valve, which was a two-way, normally closed solenoid valve (ASCO Dewrance model number 8262C). The injector valve was connected to the atomising fluid inlet tube on the atomiser, as shown in figure 6.6. The connecting piece was made as short as possible, drilled with a 3 mm diameter hole to allow unimpeded flow of helium when the valve was opened, and had a hemispherical bowl cut in its exit end to aid in washout of the helium. Calculations showed that the amount of helium remaining in the adaptor after the valve was closed was negligible compared with the total amount injected.

The helium was supplied at 45 psig (4 bar) and the injector valve was opened by a 5 ms pulse supplied by the control circuit.

6.5.3: Sampling Valve. A sampling valve was required which could

(a) open and close in a time of the order of 1 to 2 ms.

(b) withstand the environment of the exit stream of a high intensity combustion chamber, viz. oxidising or reducing conditions at gas temperatures of up to 2300°K and velocities of the order of 70 m/s,

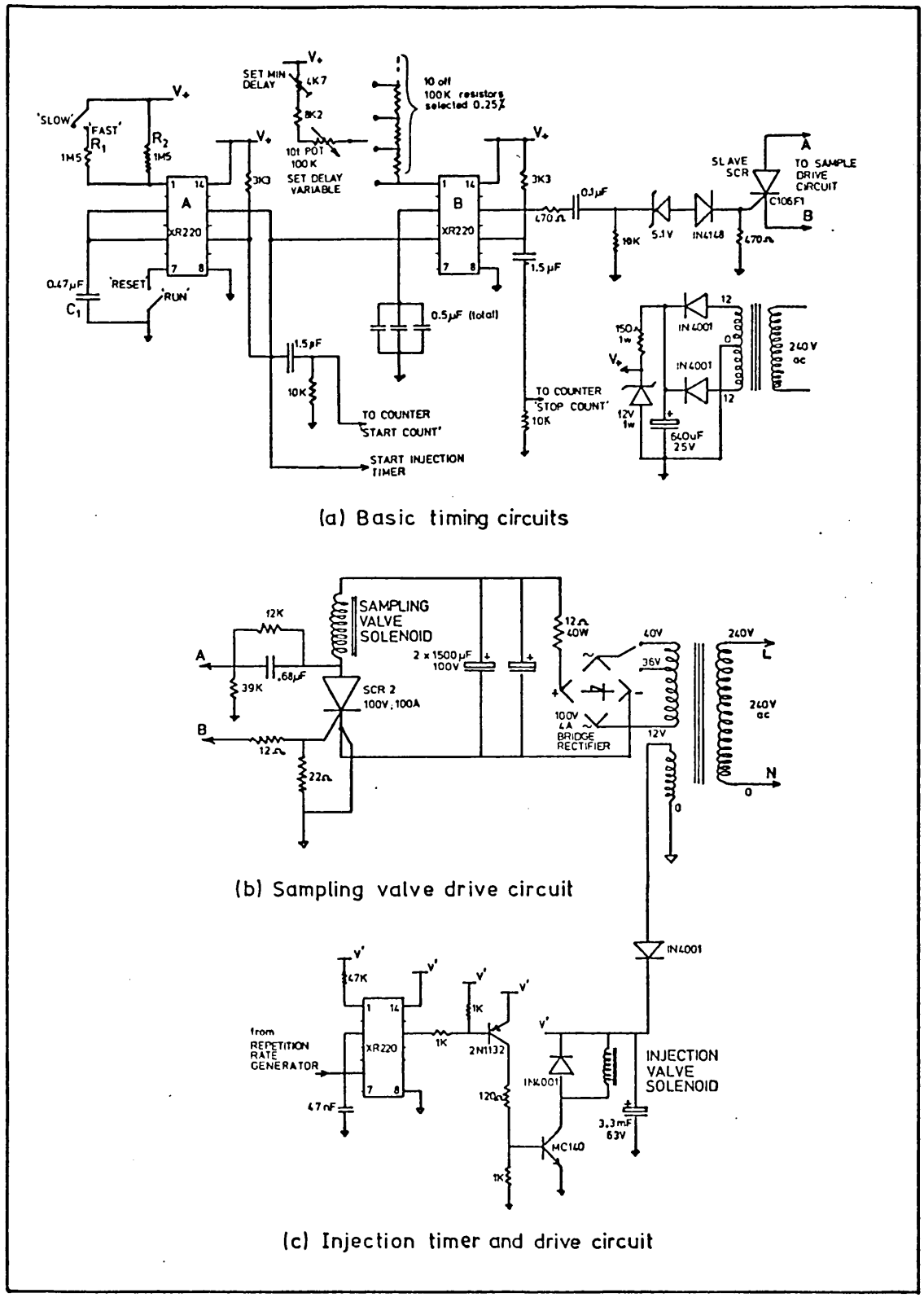

FIGURE 6.5 Circuit diagram of injection and sampling control.

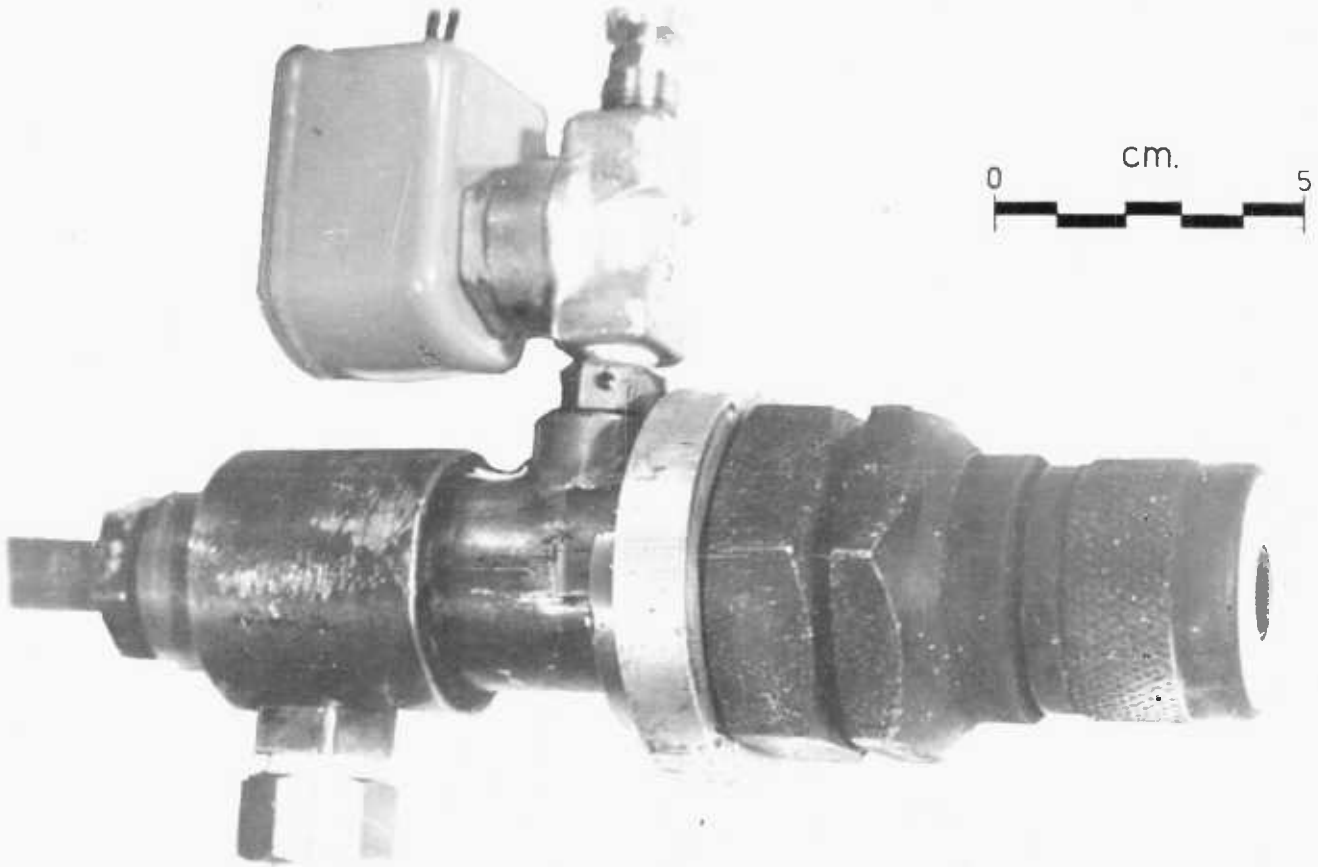

FIGURE 6.6 ATOMISER AND TRACER INJECTION VALVE

(c) sample a reasonable amount of gas from a stream at atmospheric pressure during each opening.

No such valve was commercially available, so one was developed for the purpose. The electromechanical drive mechanism was based on that of a unit developed by R.H. Aldridge (82) but the sample inlet system and the cooling system were specially designed to comply with (b) and (c) above. The construction of the valve and its mode of operation are described as follows.

Figure 6.7 is a composite photograph of the sampling valve, showing the main components in the rest position. All components shown are co-axial. Figure 6.8 is a longitudinal cross-section of the valve, while figure 6.9 shows cross-sections of the valve body in other planes.

Assembly of the valve must be carried out in a specific order as follows. Referring to figures 6.7 and 6.8, the platform which supports the hammer spring is screwed onto the valve body (with three equally-spaced 6BA screws sitting at the bottom of the groove) only after the poppet and anvil have been assembled. Following this, the coil (comprising 75 turns of 18 s.w.g. enamelled copper wire) and its support are fixed loosely onto the valve body with six equally spaced 6BA screws. The hammer spring, hammer and back section are then placed in their respective positions, taking care to slip the hammer guide over the protruding poppet shaft before tightening up all the screws. This ensures that all the components are accurately aligned on the valve axis.

The coil former, its support, and the hammer are fabricated from soft iron and each has radial splits to reduce circumferential eddy currents. The hammer spring is comprised of five turns plus closed ends of 0.63 mm diameter spring steel, 38 mm long x 12.7 mm O.D. This spring sits in the groove in the top surface of the platform.

The back section of the valve, a view of which is given in figure 6.10, serves two purposes. Firstly, it houses the rubber washers used to restrain the hammer and damp its motion after each operation of the valve. In addition it supports the hammer guide, along which the hammer slides. The use of a hammer guide as shown in figure 6.8 is preferable to using an extended poppet shaft for guidance, as it is desirable to keep the mass of the moving parts and their inertia to a minimum.

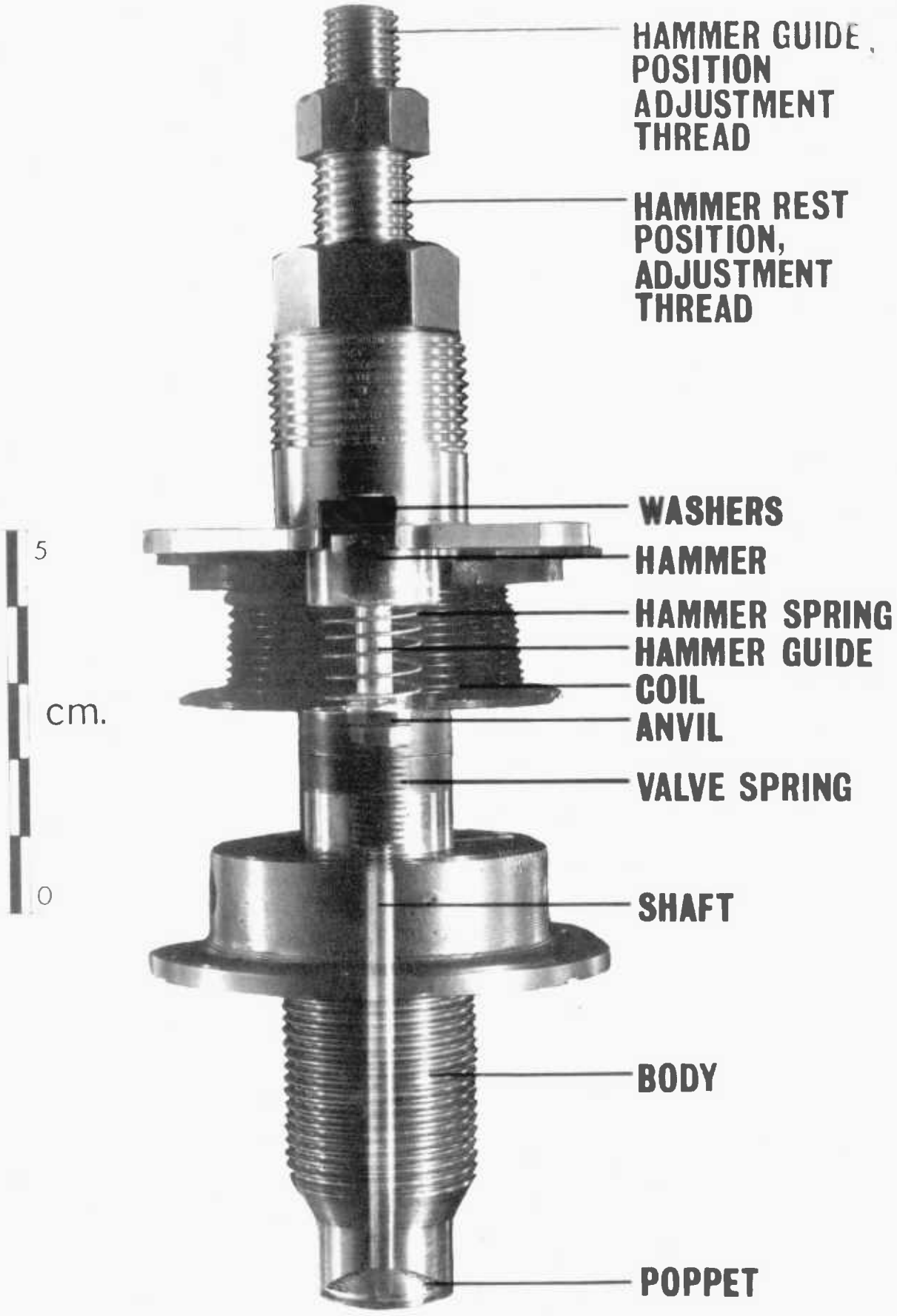

FIG. 6.7 COMPOSITE PHOTOGRAPH OF SAMPLING VALVE SHOWING CONFIGURATION OF MAIN COMPONENTS

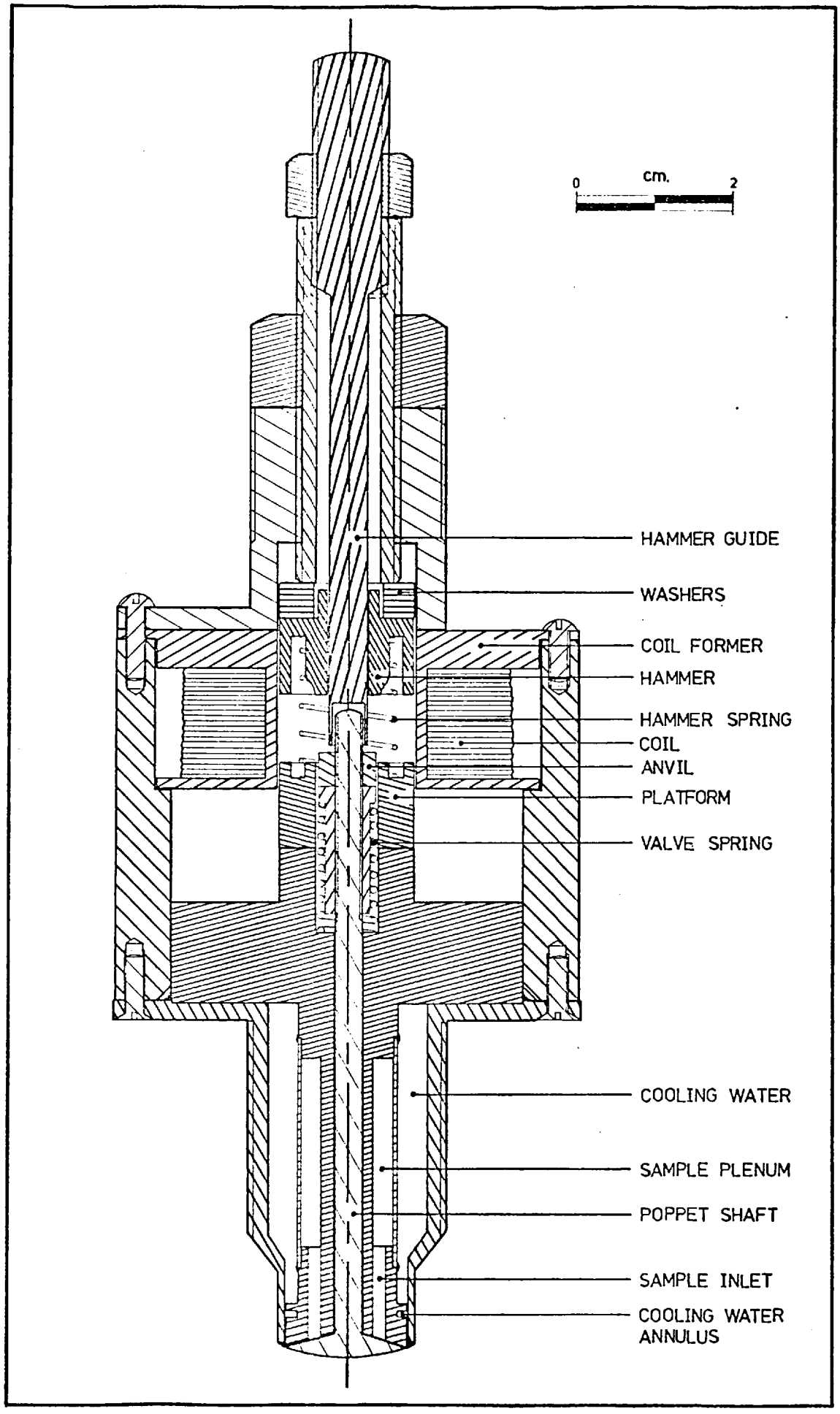

FIGURE 6.8 Cross-section of sampling valve.

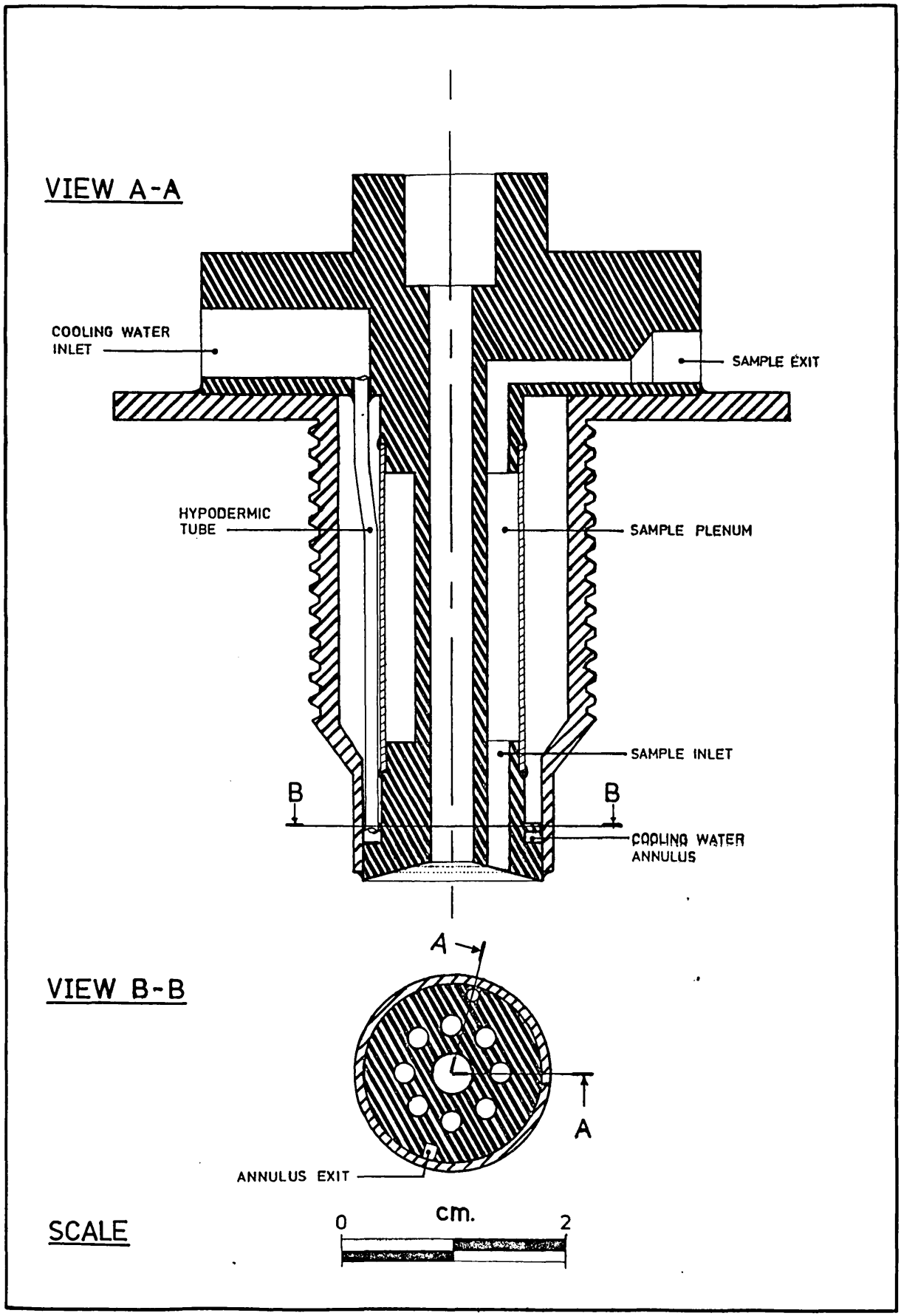

FIGURE 6.9 Sampling valve body.

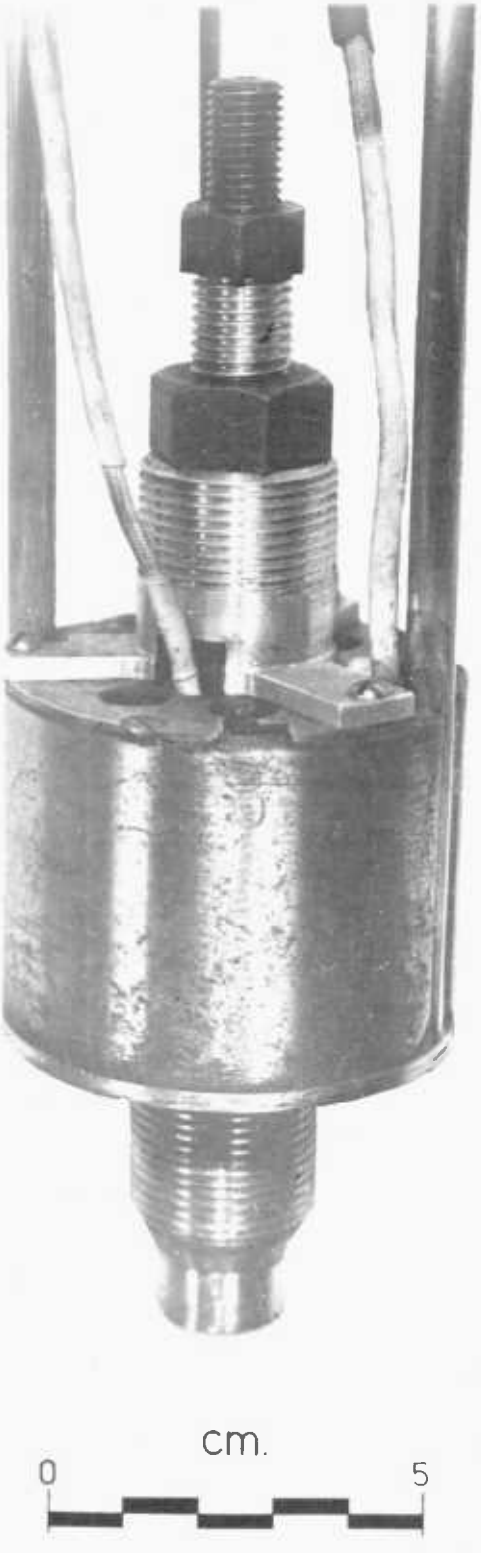

FIGURE 6.10 REAR VIEW OF SAMPLING VALVE

The front section of the valve, shown in figure 6.8 is fabricated entirely from 316 stainless steel. The valve sample intake is composed of eight 2 mm diameter holes which lead from the poppet seat to the sample plenum chamber. From here there is a single exit hole leading to the exit tube for the gas sample. When the poppet is seated, the sample intake holes are completely sealed, the matching faces having been lapped with successively finer grades of "Diagrit" diamond paste abrasive. The poppet shaft diameter is only 0.05 mm smaller than the clearance in the valve body, so that when the poppet lifts off its seat virtually no gas will be sucked from inside the valve in preference to the outside. Cooling water (supplied at 2.5 bar) is conveyed at 30 g/s by a single hypodermic tube to the front of the valve. On leaving the hypodermic tube the cooling water divides equally and flows in each direction around an annulus around the valve seat until it leaves through a hole opposite the entry. It then flows through the valve between the outer wall and the sample plenum chamber and out to the water exit pipe through a single tubular passage.

The poppet is made from inconel as it is required to maintain its strength at high temperature. The anvil and lock nut are made of beryllium-copper due to the relative ease of working in the half-hard state and the subsequent hardness which is attainable by either heat treatment or work hardening from repeated blows by the hammer. Considerable difficulty was initially experienced with the anvil gradually becoming unscrewed from the poppet shaft during valve operation. The first remedy that was attempted was the addition of a lock-nut, and when this was not found adequate, three high tensile steel socket set screws were set in alternate faces of the lock nut to lock it onto the poppet shaft. The shaft itself was dimpled so that the set screws, which had points ground at their ends, would positively lock into the shaft. The anvil, lock nut and set screws were all further secured from loosening with "Loctite". The valve spring (25.4 mm long, and 8.25 mm OD) comprised 8 turns plus closed ends of 1.3 mm diameter spring steel.

The operation of the valve is as follows. The coil is energised by the control circuit, and the hammer is accelerated against the hammer spring until it strikes the anvil. If the hammer continues to move forward with the anvil it is stopped by the top of the platform, whose level is just below the initial level of the top of the anvil. The hammer is then returned to its starting position by the hammer spring. As a result of the short duration impulse transmitted by the hammer, the anvil and poppet shaft move against the valve spring causing the poppet to be

displaced from its seat and the sample inlet holes to be opened. The valve spring causes the poppet to rapidly return to its rest position.

6.5.3.1: Testing of the Valve

(a) Leak testing. The valve seal was tested by connecting the sample exit tube to a pressure gauge with about 50 cm of 6 mm tubing, and evacuating the system with a rotary vacuum pump to a pressure of less than 10^{-1} torr (13.3 N/m^2) when the line to the pump was closed off with a valve. If the gauge indicated less than 1 torr after being left for an hour, the seal was considered satisfactory.

(b) Repeatability. It is essential that the valve opening is repeatable with respect to the time that the energising pulse is applied to the coil. This was checked by the following experiment.

The valve was secured in its horizontal firing position on a rigid platform which could be traversed by means of a calibrated screw. A laser beam was passed across the valve poppet so that the poppet just obstructed part of the beam, and a photosensitive detector was placed in the beam path on the far side of the poppet. The detector was connected to an oscilloscope through a circuit whose voltage varied with the amount of the laser beam reaching the detector. The relationship between the poppet displacement and the voltage was ascertained by moving the calibrated platform and noting the corresponding voltage output of the detector. The calibration curve is shown in figure 6.11(a).

The valve was then energised repeatedly (once a second) with the oscilloscope being triggered by the coil current pulse. The trace of the output voltage (related to valve displacement above) with time was recorded using the oscilloscope in the storage mode. Figure 6.11(b) shows a photograph of the oscilloscope traces for twenty consecutive openings, and clearly indicates the repeatability of the valve opening with respect to timing, duration and displacement. The method used was sufficiently sensitive to detect the bounce of the poppet on the seat as the valve closed. The valve began to open about 4.5 ms after the coil was energised and remained open for about 1 ms. The voltage produced by the detector was non-linear with respect to displacement but from the calibration curve the maximum displacement was determined as approximately 0.5 mm. Greater accuracy could have been obtained by focusing the circular laser beam into a line, resulting in a linear calibration, but the system used was adequate for the purposes of the test.

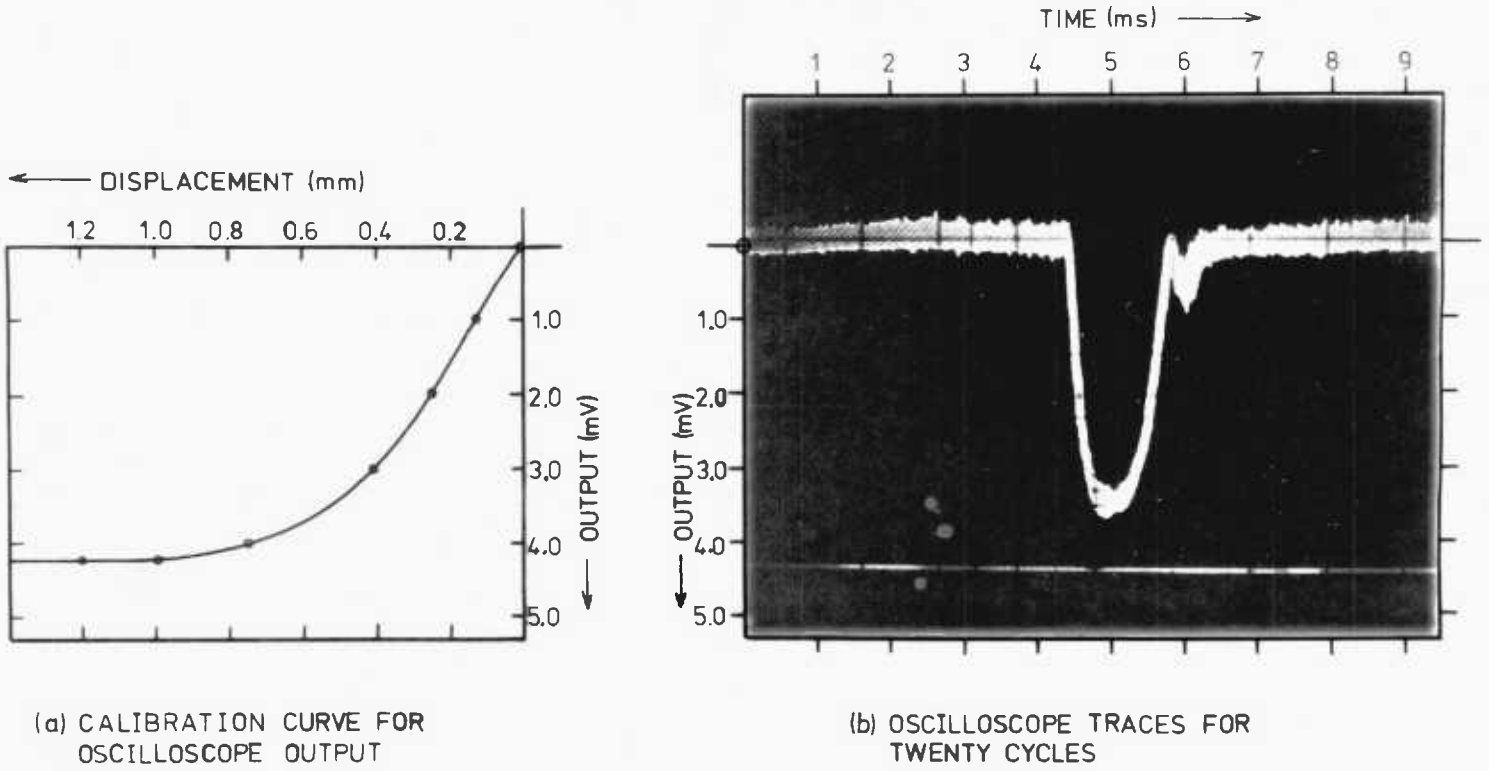

(a) CALIBRATION CURVE FOR OSCILLOSCOPE OUTPUT

(b) OSCILLOSCOPE TRACES FOR TWENTY CYCLES

FIGURE 6.11 POPPET DISPLACEMENT WITH TIME

(c) Amount of Gas Sampled per Opening. This is an important criterion of the valve as it determines to a large extent the number of times it must be cycled to draw in sufficient gas for analysis.

The gas sampling rate was tested by measuring the pressure increase in a vessel of known volume. For atmospheric ambient pressure and an evacuated sample plenum chamber (i.e. Δp of about 1 bar) the sampling rate was 1.5 cm^3 of air at STP. The advantage of the large sample flow area provided by the eight holes in the poppet seat may be appreciated when comparing this figure (i.e. 1.5 cm^3 for Δp of 1 bar) with that for other rapid sampling valves. For example, Pratley et al. (83; p.18) quote 0.13 to 0.22 cm^3 per opening for Δp of 4 to 16.5 bar for their valve and Garner et al. (84) observed values of 0.2 to 0.8 cm^3 per opening for Δp of 17 to 40 bars. These examples are in the range of 0.01 to 0.03 cm^3/bar, indicating that the new valve design (giving 1.5 cm^3/bar) results in a sample size per opening about two orders of magnitude greater than previous sampling valves.

6.5.3.2: Positioning of valve in chamber exit stream. A special adaptor was designed to hold the sampling valve in the cross-piece downstream of the combustion chamber. The adaptor was faced with cast refractory, which was shaped so as to match the sampling cross-piece wall and was designed to allow only the poppet to be exposed to the combustion gases. Stages in the assembly of the valve in its adaptor are shown in figure 6.12.

The refractory face protruded into the exit tube by about 5 mm and the sampling valve by a further 5 mm. The highly turbulent conditions in the tube should ensure that the tracer concentration was constant across the tube section, the valve being placed a little way into the tube to overcome any boundary layer effects.

6.5.4: Sample Handling and Tracer Analysis. The combustion gas sucked into the sampling valve each time it opens must be fed to the helium leak detector in a carefully controlled manner so that the detector output will be truly proportional to the helium concentration in the sampled gas.

A Mullard model VC400 helium leak detector was used for tracer analysis. This instrument is a mass spectrometer used to detect only helium. The leak detector was tested for linearity using standard leaks supplied by the Ministry of Defence (AQUILA) and found to be satisfactory in this respect. It was not, however, as sensitive as its specification claimed and this dictated the use of higher tracer gas concentration than would otherwise have been necessary.

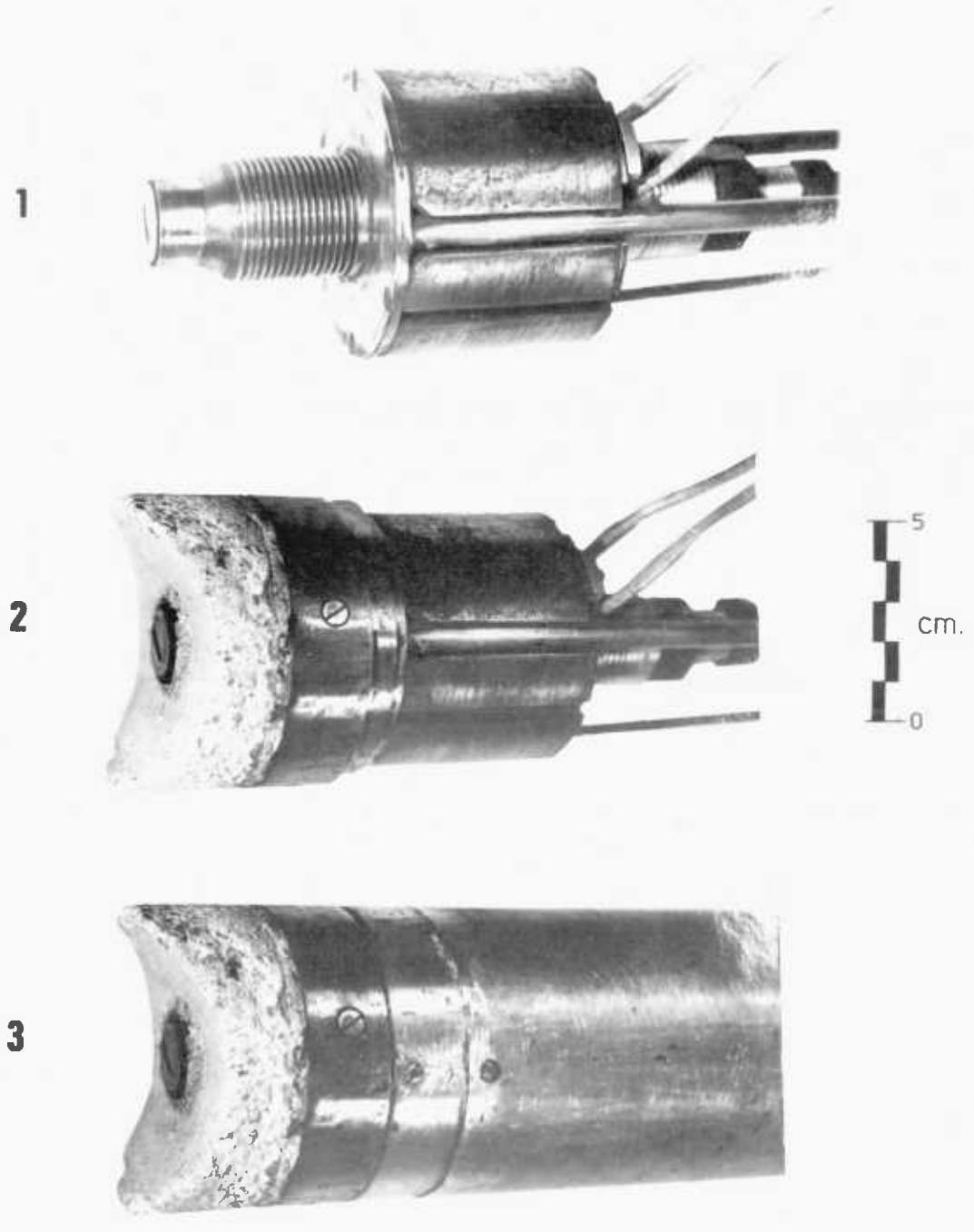

FIGURE 6.12 STAGES IN ASSEMBLY OF SAMPLING VALVE IN CROSS-PIECE ADAPTOR

The mass spectrometer works on the basis of detecting a fixed proportion of the helium atoms which flow into the instrument, so that the output is proportional to the helium flow rate. The gas sample flow rate into the instrument must therefore be kept constant for the duration required for the detector to reach its steady state output. Furthermore, this flow rate must be accurately repeatable from one sample to the next as it is the relative tracer concentration of the different samples which determines the shape of the concentration-time curve.

The problem of gas sampling for mass spectrometers is further complicated by the low pressures and throughputs characteristic of these instruments. As the pressure in a system is reduced to the point where the mean free path of the molecules is comparable with the dimensions of the system, the flow regime begins to change from viscous to molecular. The laws describing flow in each of these regimes are discussed by Dushman (85, chapter 2), and an understanding of the principles involved is necessary when designing a system for sample handling.

The system used was based on that described by Honig (86), in which the sample is expanded into a reservoir from where it leaks slowly into the mass spectrometer inlet through a fine orifice. The reason for expanding the sample into the reservoir is the necessity to reduce its pressure to a level which results in a flow through the fixed orifice less than the pumping capacity of the mass spectrometer vacuum system at a pressure of 10^{-4} torr (13.3 mN/m^2). If the flow through the orifice exceeds this pumping capacity, and the pressure in the mass spectrometer increases above 2×10^{-3} torr (266 mN/m^2), a pressure sensitive switch turns off the mass spectrometer filament to prevent it being oxidised.

The leak was made by drawing down a glass tube until (by trial and error) the orifice size was such that the flow through it did not cause the mass-spectrometer filament to switch off for reservoir pressures up to about 10 torr (1.33 kN/m^2).

A constant and repeatable flow rate was achieved by ensuring that a constant pressure of gas was present in a 1000 cm^3 reservoir during each analysis.

Zemany (87) discusses the flow conditions in mass spectrometer inlet systems and the consequences of viscous or molecular flow. If the flow from the reservoir through the leak is molecular, the helium tracer flow rate would be relatively greater than that of the other gases and the reservoir would become gradually depleted of helium, so that it is preferable that the combination of reservoir pressure and orifice diameter be such that the flow is in the viscous regime. This

was tested for by allowing a reservoir sample to be analysed over a long period (10 minutes) and observing that the detector output remained constant. The reservoir pressure also remained constant for the whole period so that the leak rate is small relative to the amount of gas present in the reservoir. When the same test was repeated using a "metrosil" porous plug leak (88) which ensures flow in the molecular regime for pressures up to 100 torr (133 kN/m^2), the detector output was observed to fall with time indicating the depletion of helium in the reservoir. This was performed as a control to ensure that the flow in the glass leak was effectively viscous and did not appear so only as a result of detector inaccuracy.

A diagram of the sample handling system appears in figure 6.13.

A sample is trapped between valves A and C and expanded into the previously evacuated flask by opening valve C. The leak detector begins to respond almost immediately to helium passing through the leak, and reaches a steady value within about five seconds.

Detailed instructions for carrying out a test appear in the next section.

6.5.5: Procedure for Carrying Out a Stimulus Response Test

1. Ensure that the combustion chamber is operating at steady state at the required conditions.

2. Check that the helium injection pressure is at 45 psig (4 bar) and that the helium feed line has been purged with helium.

3. Zero the output of the leak detector and ensure that it is ready for use according to the instruction manual. Valve F (figure 6.13) is in the closed position if this is the first test of the day.

4. Close valve A, and open B, C, D and E and switch on the roughing pump (Edwards, model ED200). The pressure in the gas handling system should fall below 10^{-2} torr (1.33 N/m^2) quickly once the pump has warmed up. This may be checked by the Pirani Gauge on the reservoir.

5. Close valves C, D and E and open F. The reservoir is now sealed off except for the fine leak into the mass spectrometer, and the pressure remains constant at about 10^{-2} torr (1.33 N/m^2).

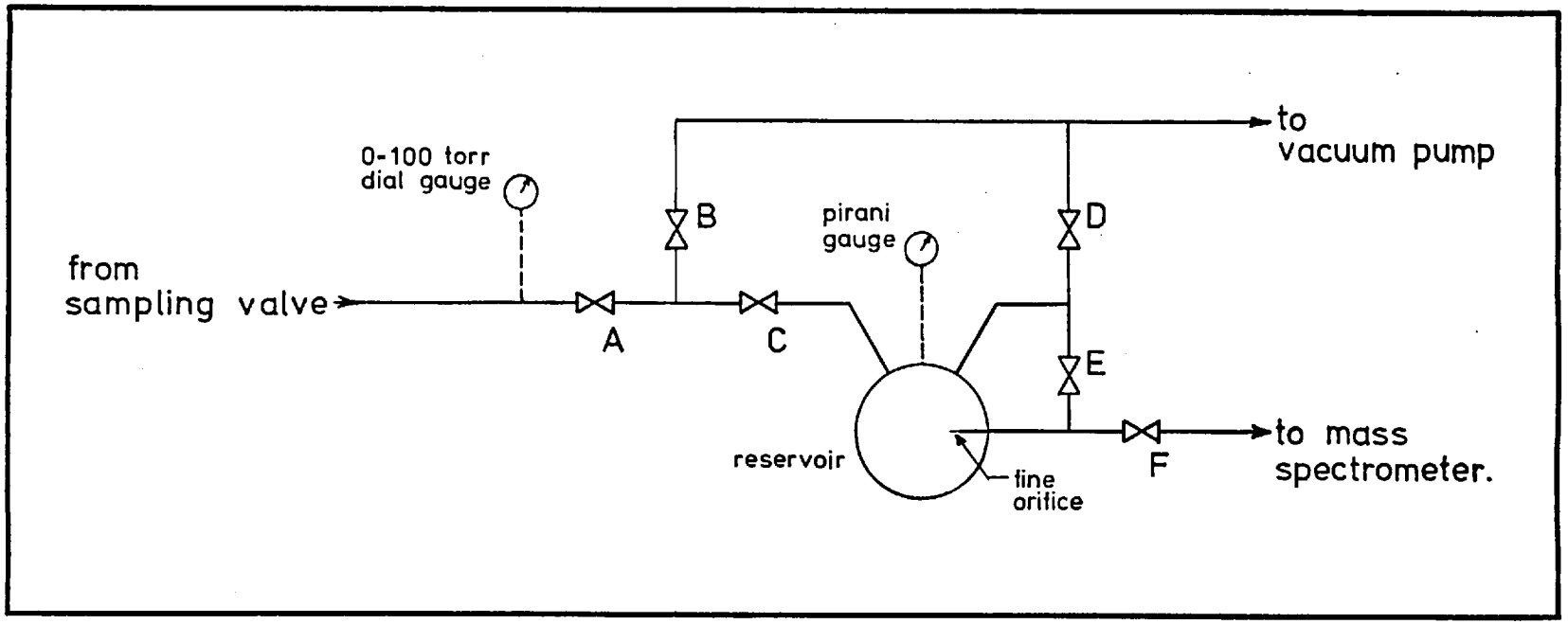

FIGURE 6.13 Sample handling and mass spectrometer feed system.

6. The sampling valve plenum chamber and connecting pipe are evacuated to less than 10^{-1} torr (13.3 N/m^2) by opening valve A, the sample handling system now being ready for use.

7. The sampling delay time, t_{sd}, is set on the control system at the value required.

8. The injection and sampling valves are activated by switching on the control circuit and valve B is immediately closed.

9. Allow injection and sampling to continue until the dial gauge indicates a sample pressure of 100 torr (13.3 kN/m^2) in the valve sample line and at this point close valve A promptly, trapping some gas sample between valves A, B and C. Switch off the control circuit.

10. Open valve C expanding the trapped sample into the reservoir where the pressure should be shown by the Pirani Gauge to be 8 x 10^{-1} torr (106.6 N/m^2). The sample immediately begins to leak into the mass spectrometer, which should give a steady reading in less than five seconds.

11. To prepare the sample handling system for the next test, evacuate the system by opening valves D and B until the pressure in the reservoir falls to less than 10^{-2} torr (1.33 N/m^2). Then close valves C and D and repeat steps 6 to 10.

12. To shut the system down, close valves F, D and B and open all the other valves. The roughing pump may be turned off, and the mass spectrometer vacuum system may be turned off or left running depending on when it is next required. (It should be left running if this is less than a week).

6.5.6: Measurement of Input Pulse Shape. Even though the control system supplies a voltage to the injection valve for a known period of time, this time is not the effective pulse duration for two reasons. Firstly, the injection valve would have some inertial effects which could be significant relative to the short (5 ms) pulse supplied. Also, the pulse of helium is injected into the atomiser air tube, and flows with the atomising air into the chamber. The effective input pulse shape with regard to the chamber is therefore that at the atomiser exit, and the only way to determine this with any certainty is to measure it.

A special adaptor was constructed to enable the sampling valve described in section 6.5.3 to be used for measuring the pulse shape at the atomiser exit. If the

sampling valve were simply held near the atomiser exit the helium concentration would be affected by entrained air, draughts, etc. so that the adaptor was essential.

Figure 6.14 shows the adaptor holding the atomiser and sampling valve so that the air from the atomiser (there was no fuel feed, the cup being filled with plasticine) passes the poppet seat with a minimum of space between the two, and then along the outside of the valve and out through the radial holes in the adaptor.

The input pulse shape was measured using the procedure given in section 6.5.5.

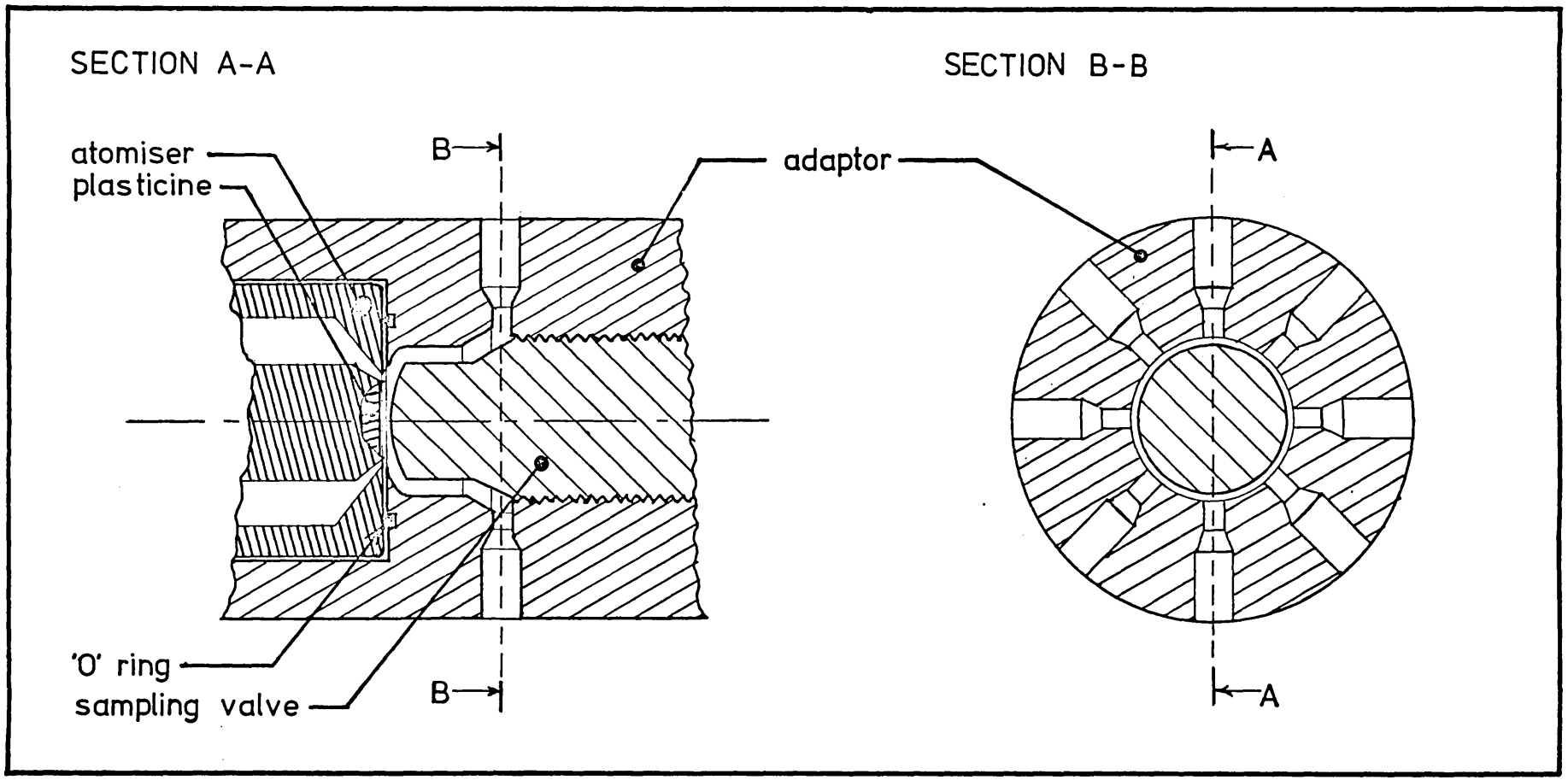

FIGURE 6.14 Adaptor used to measure tracer pulse at atomiser exit.

7. EXPERIMENTAL PROGRAM AND RESULTS

This chapter will describe the experimental program undertaken and the results obtained.

7.1: Experimental Conditions

Experimental runs were performed with the high intensity spray combustion system described in chapter 5 for a number of different combinations of parameter values.

The spray drop size distribution was kept constant ($\bar{D}_{31}$ = 52 μm) throughout by using the same fuel firing rate (2 g/s) and atomising air/fuel ratios (2.0).

The chamber parameters which were varied are

(i) the overall equivalence ratio, ϕ. This parameter affects the performance of the combustion chamber through its effect on the combustion chemistry and thermodynamics.

and (ii) the forward/reverse secondary air mass flow ratio. This ratio may affect the aerodynamics of the chamber and also the equivalence ratio in various parts.

The combustion chemistry and thermodynamics are also interrelated with the reactor flow configuration in the chamber, so that the above effects are not separable. In particular the flow configuration will determine the distribution of local equivalence ratios in each reactor element. However, if each is well defined, a good model of the spray combustion process will be able to predict the combustion temperature and products both at the chamber exit as well as in various parts of the chamber.

Table 7.1 Numbering of Experimental Runs in Relation to Values of Parameters Varied

Ratio of forward to reverse secondary air mass flow rates	Overall ϕ		
	0.9	1.0	1.2
4/5	8	2	7
1/1	4	1	5
5/4	9	3	6

For each of the runs in Table 7.1 the nitric oxide concentration was measured at the chamber exit. The stimulus response experiments were carried out as described in chapter 6 for runs 1-7. The concentration-time curve was obtained by separate experiments each fixing a single point at a time. The sampling delay time, t_{sd}, was varied at random to avoid any systematic errors. As a check some points were repeated during each run, and if any point seemed not to fall on a reasonably smooth curve, it too was repeated. As all the points obtained for each run fell on a smooth curve, the error associated with the curve is small as it is a combination of a considerable number of independent measurements.

In addition, the input pulse shape was measured using the system described in section 6.5.6. This experiment was repeated a second time on a different day to confirm that the input pulse shape remained constant. The duplicate input pulse appears as Table H.9, Run $^{-3}$.

7.2: Experimental Results

The results of the nitric oxide measurements are shown in Table 7.2 and the stimulus response results are given in Appendix H.

The raw stimulus response data was processed by a computer program (LAPLACE) described in Appendix I. The time datum for the experiments is measured from the time that the control circuit drive pulse to open the injection valve begins. Program Laplace calculates the initial point of the response, i.e. the point in time when tracer first begins to appear, and then calculates the area under the pulse. Each ordinate is then divided by this area to obtain points on a normalized curve. A typical set of normalized input/output points is shown in Figure 7.1.

Table 7.2 Measured Nitric Oxide Emissions (ppm by volume)

Ratio of Forward/ Secondary Air Mass Flow Rates	ϕ = 0.9	ϕ = 1.0	ϕ = 1.2
4/5	40	64	89
1/1	35	52	45
5/4	29	50	73

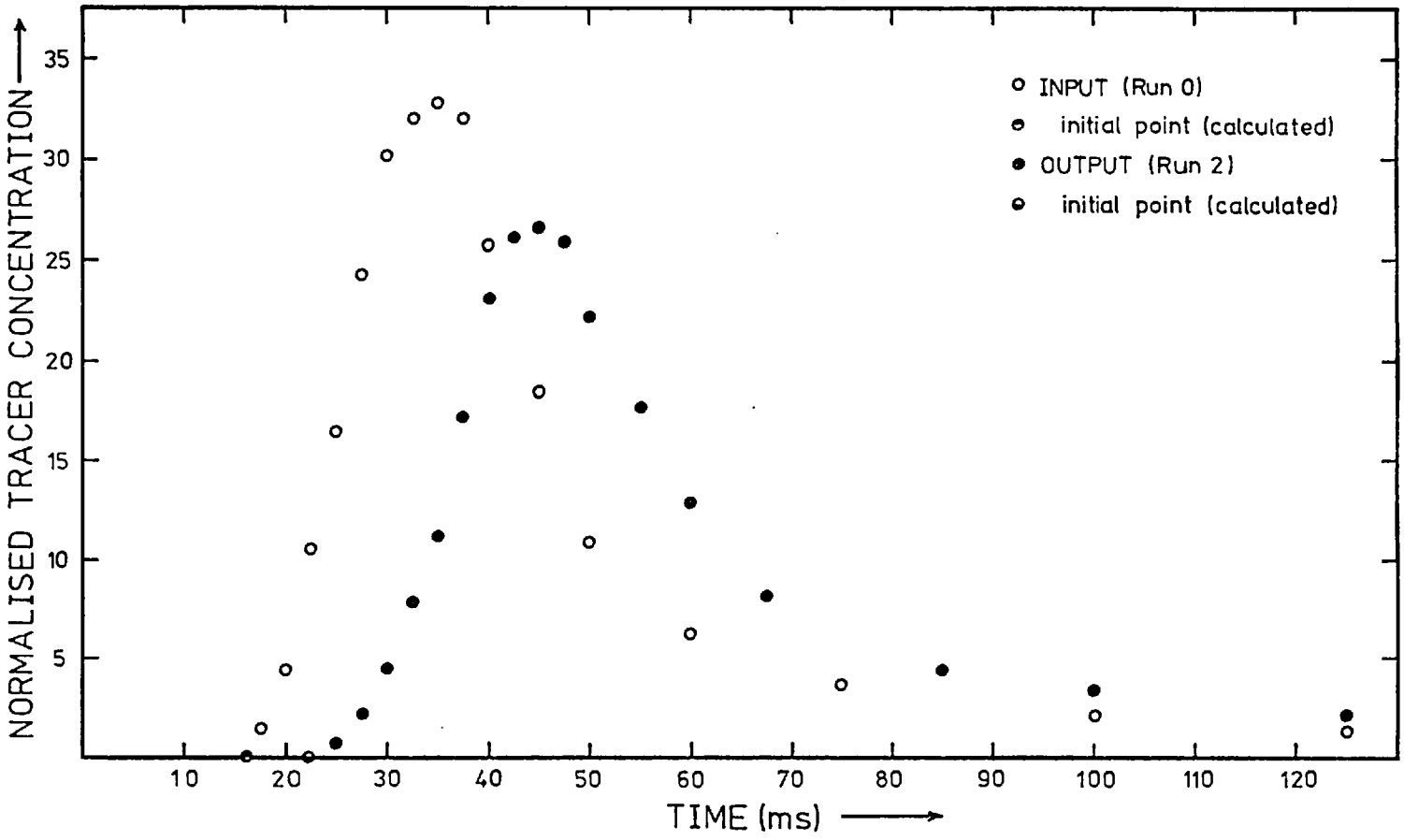

FIGURE 7.1 Experimental input/output data

For each curve the time delay (from the above datum) of the initial point is attributed to the sum of

(i) the delay between the opening of the injection valve and appearance of tracer at the sampling valve (plug flow delay),

and (ii) the difference between the time it takes the injection and sampling valves to open, each measured from the beginning of the electrical drive pulse to its respective coil from the control box.

As the time involved in (ii) is constant for both input and output pulse measurements, the difference between the delays for each pulse may be attributed completely to (i), i.e. the difference in time of the initial points of the input and output curves is assumed to be the plug-flow delay time of the system being measured. This plug-flow delay time is calculated directly from the time domain data and then the rest of the configuration (which is in series with the plug flow delay) is identified on the basis of transfer functions calculated from the input and output curves, each shifted to begin at the origin. The details of this procedure are given in Appendix I.

The mean time of the shifted input and output curves (t_p) may be calculated, and the difference between these is the mean time, τ, of the chamber (excluding the plug flow delay). This is because the mean time of the output is necessarily the sum of that of the input and the system.

Program LAPLACE carries out all the above time domain calculations and in addition calculates the LTI and LTO and G(s) for a range of the Laplace parameters. These values are given in Appendix H for each run, and are plotted in figure 7.2.

As a check on the time domain calculation of τ, the program lists $\frac{1}{s} \ln [G(s)]$ for each value of s. This quantity approaches $-\tau$ as s approaches zero (89). Figure 7.3 shows the value of $\frac{1}{s} \ln[G(s)]$ plotted against s for each run and compares the intercepts with τ as calculated in the time domain. In each case the results agree.

The computed transfer functions constitute the derived experimental results each of which is to be matched by the transfer function of a feasible reactor flow configuration to model the chamber as discussed in chapter 2.

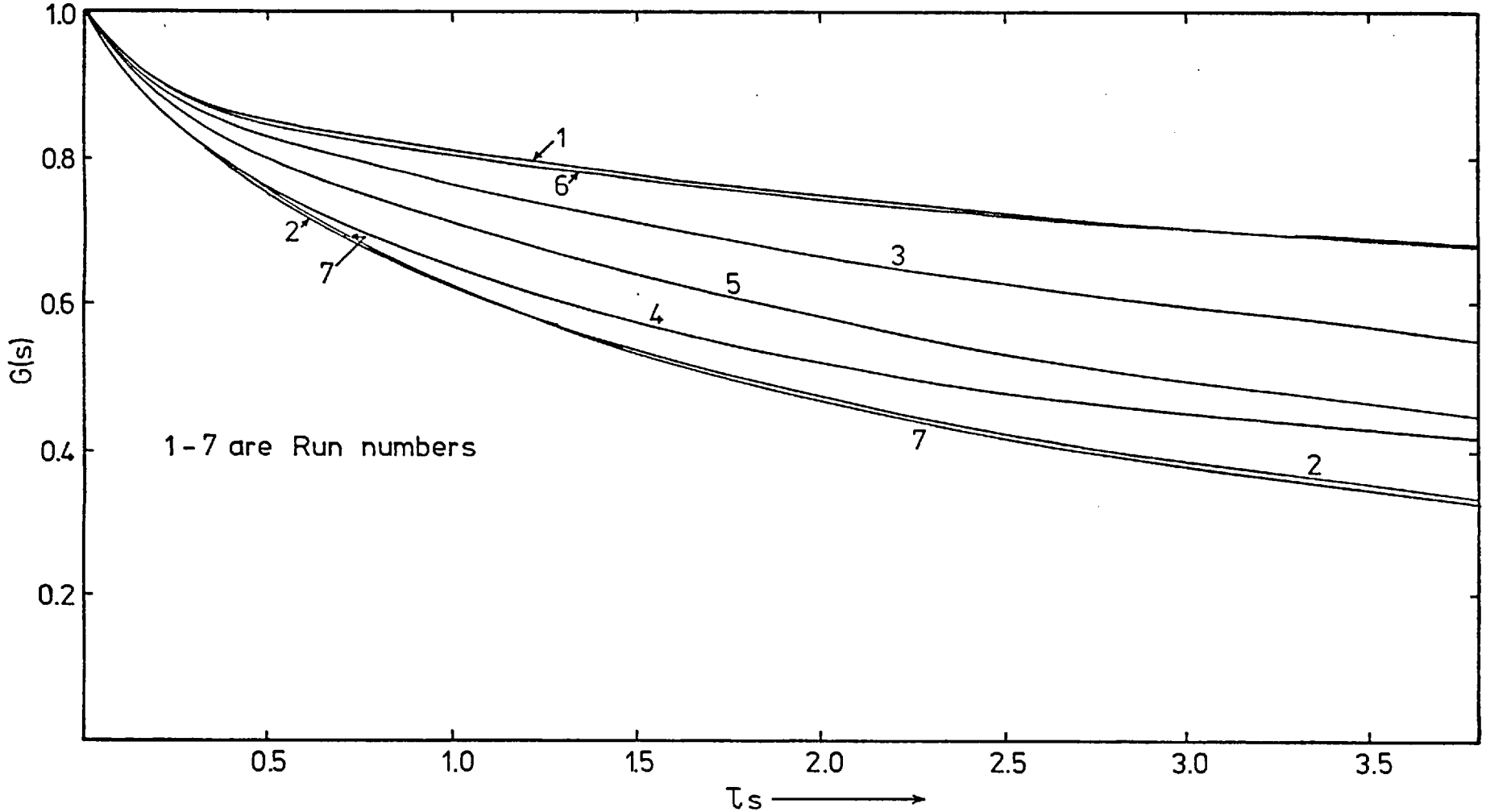

FIGURE 7.2 Transfer function for each run.

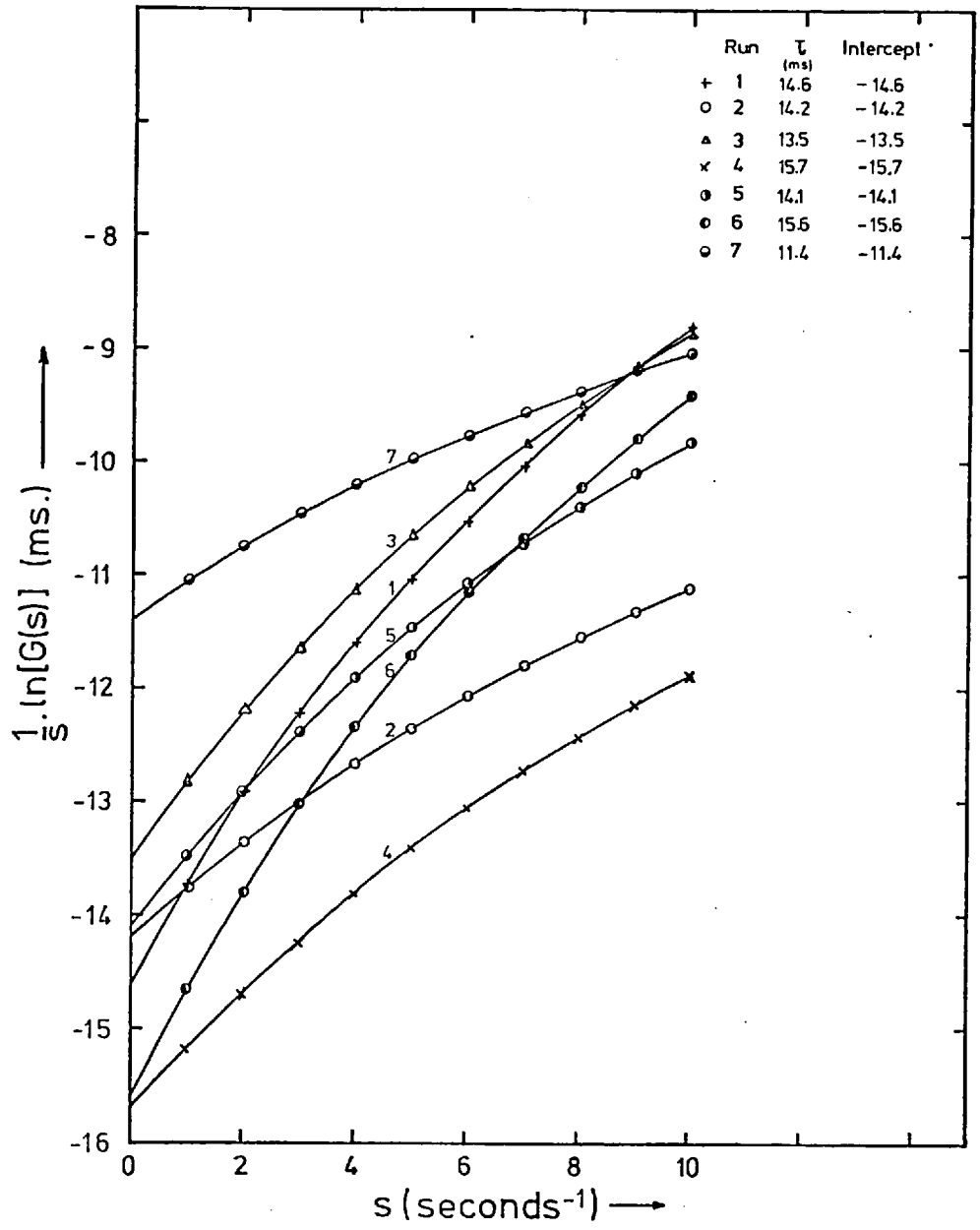

FIGURE 7.3 Mean residence time from Laplace domain.

8. ANALYSIS OF RESULTS AND EVALUATION OF COMBUSTION CHAMBER MODELS

This chapter describes the development of feasible reactor flow configurations for the combustion chamber used. Following this, the actual configuration of the chamber for each run is identified using the stimulus response experimental results given in Appendix H. Predictions of the spray combustion model developed in chapter 4 for the performance of each configuration are then given, and the model evaluated on the basis of the agreement of its predictions with measured results; the effects of various assumptions in the model are discussed. Finally, the way in which the model elucidates the effects of a number of chamber design and operating parameters is pointed out.

8.1: Feasible Reactor Element Configurations

The aerodynamics of a combustion chamber is determined mainly by the chamber geometry and the relative disposition and momenta of the inlet streams.

As shown in Appendix F, the primary air/fuel spray emerging from the atomiser is the main source of momentum and kinetic energy in the chamber. The fuel spray enters the chamber as a supersonic jet with a cone angle of about 40°. Because of its predominant momentum it may be assumed that most of the jet proceeds undisturbed, i.e. in turbulent plug flow, along the axis of the chamber. The jet may or may not penetrate to the end of the chamber, depending on the particular conditions present.

The expected aerodynamics of the forward region of the combustion chamber is depicted in figure 8.1.

The external recirculation is caused by the high momentum turbulent jet entraining fluid along its length, with the consequent reduction in pressure near its base inducing reverse flow from the outside edge of the partly dissipated jet further downstream. The secondary air jets would enter the recirculating flow, and possibly enhance it relative to the axial flow. Internal recirculation would be minimal due to the absence of swirl resulting from bypass of the swirlers of the atomiser as discussed in section 5.3.

From the physical picture built up above, the forward secondary air enters the outer recirculation zone and only finds its way into the jet by means of the entrained recirculation. Also it seems that a process of distributed interchange between the plug flow and recirculation zones would take place, especially in view

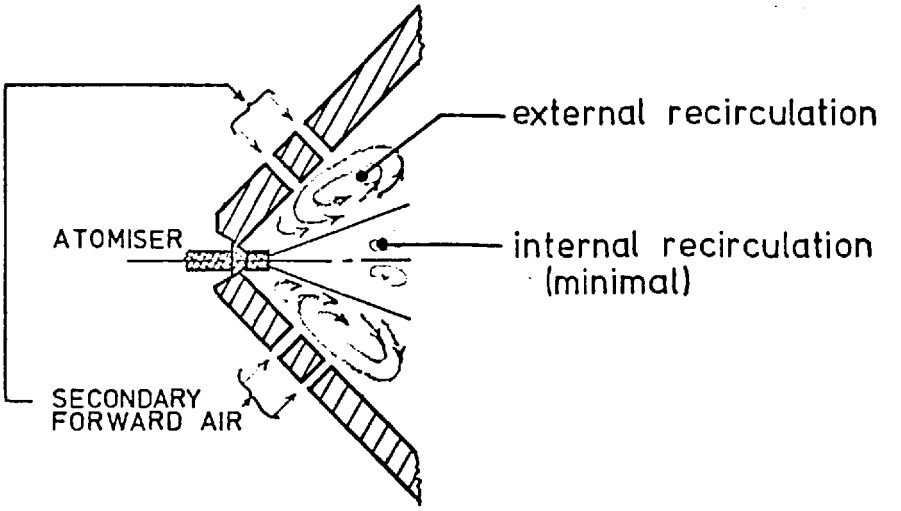

FIGURE 8.1 Expected flow pattern in chamber forward section.

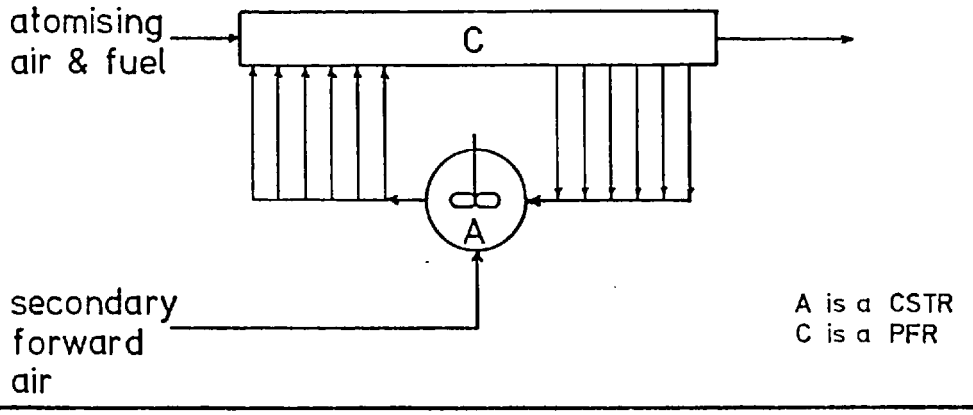

FIGURE 8.2 Flow model for chamber forward section.

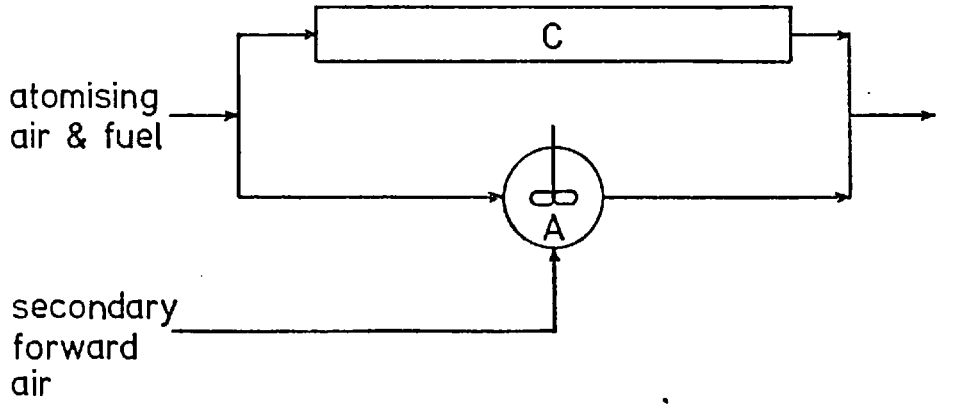

FIGURE 8.3 Effective reactor flow configuration for chamber forward section.

of the fluctuating local conditions resulting from turbulence. Figure 8.2 is a schematic diagram of the distributed interchange between the plug flow jet and recirculating flow. The former is denoted by a plug flow reactor (C) and the latter by a CSTR (marked A).

The extent or indeed the existence of distributed interchange between the reactor elements A and C would be very difficult to ascertain from stimulus response experiments for the following reason. The residence time in element C is much less than the mean residence time in A, so that tracer which enters A at any stage will have a residence time distribution (RTD) very similar to that of A, while that which passes straight through C will do so in the very short residence time of that element (due to the supersonic initial jet velocity). A negligible amount of the flow will pass through A twice as the fraction recirculated from C is small due to (i) the low amount of swirl and (ii) the secondary air providing most of the entrainment requirements of the jet. Consequently the RTD will distinguish between tracer which passes through A from that which does not, but it will not be able to determine the precise nature of the interchange. Even if the mean residence times of A and C were similar, the integrating effects inherent in RTD experiments do not, in general, allow the interpretation of fine structure such as distributed interchange.

In view of the above, the reactor flow configuration of figure 8.2 may be represented by the effective configuration of figure 8.3, and this will be considered the feasible model for the chamber forward section.

The products of the forward section pass into the rear (or reverse) section where the secondary reverse air is introduced. Depending on the relative momenta, the entire products of the forward section may mix with the secondary air in reactor element B. Alternatively the jet core will bypass reactor B, leaving only the slower moving outside regions (which is that participating in the interchange in the forward region) to mix and react with the secondary air.

A plug flow delay was detected in each run, and this is shown in the feasible models as reactor D at the exit. Whether this represents plug flow in part of the chamber or in the exit tube prior to the sampling valve (or a combination) is open to question, but the effect on the RTD remains the same. This is the most feasible position to account for this delay.

Figures 8.4(a) and (b) show the two alternative feasible reactor flow

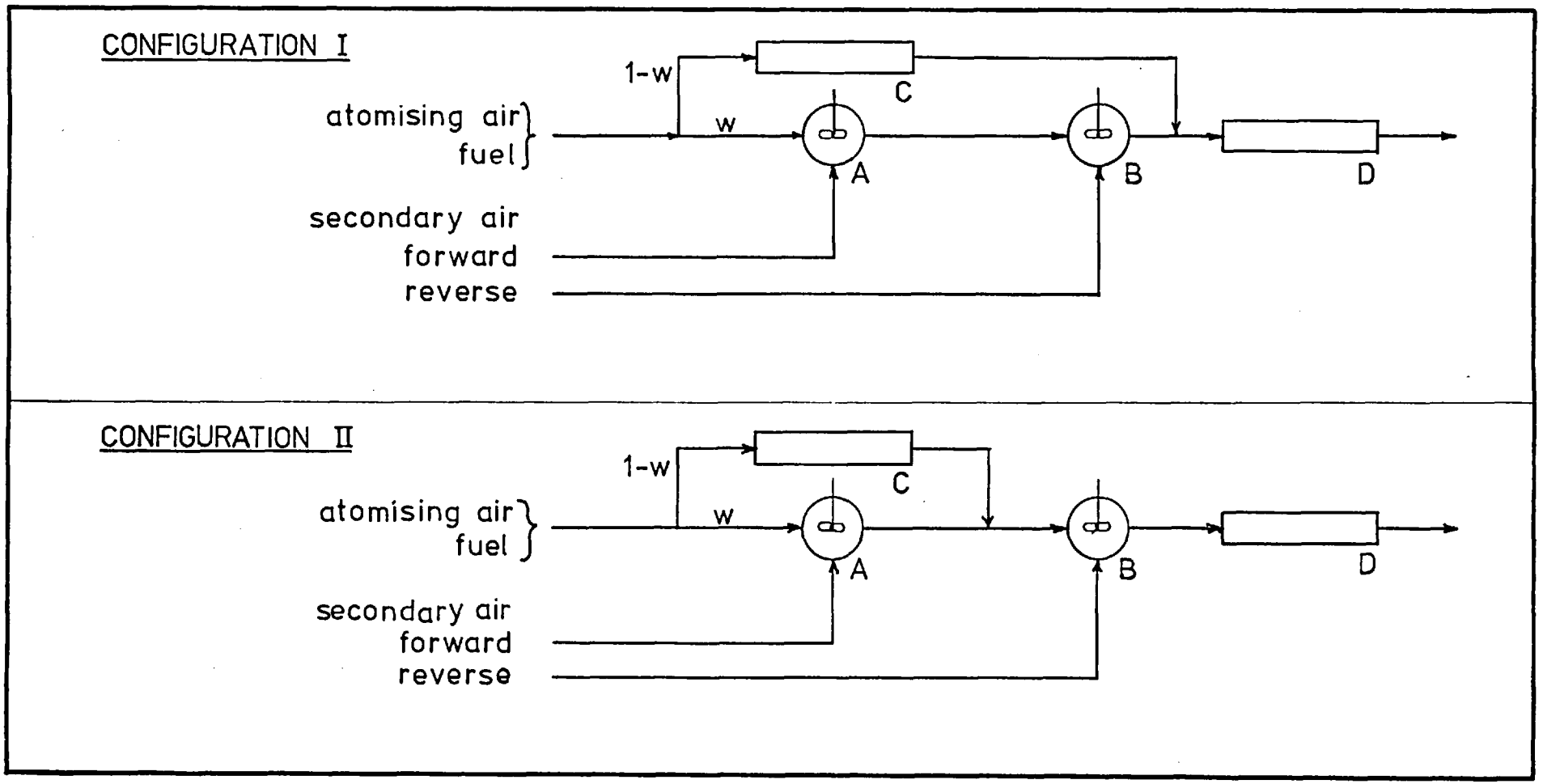

FIGURE 8.4 Alternative feasible reactor flow configurations

configurations of the chamber arrived at by combining the above models for each part of the chamber.

The transfer functions of each of these configurations excluding plug flow reactor D has been calculated for a range.of their parameters, viz. relative residence times of the elements and relative amount of bypass flow through element C. Some of these are shown in figures 2.4 and 2.5.

8.2: Identification of Best Configuration and its Parameters

As discussed in chapter 2 the best reactor flow model for the combustion chamber are selected by comparing values of the experimental and model transfer functions for values of τs of 1, 2 and 3.

Table 8.1 shows the values of the experimental transfer functions for each run at these values of τs. Tables 8.2 and 8.3 show the values of the transfer functions of the best fit models and the model parameters respectively. The values of τ of the individual reactor elements are derived from the overall mean τ and the model parameters using the equations in Appendix A. An example is given in Appendix E.

8.3: Combustion Performance Predicted by Chamber Models

For each run listed in Table 8.3, the reactor flow configuration and its parameters could now be used together with the spray combustion model developed in chapter 4 to estimate the conditions in each reactor element of the chamber model, and at the exit.

A detailed calculation for the entire configuration of Run 5 is shown in Appendix E by way of example, and the results for four runs so calculated are summarised in Tables 8.4 to 8.7. The following points relevant to the calculations should be noted here:

(i) The exit stream from one reactor element and any other feed to the next element are assumed to be instantaneously mixed upon entry (micromixed CSTR conditions) and their ratio and compositions will determine the effective feed temperature and composition of the element.

(ii) Due to the extremely short residence time in reactor element C for each run, and the low feed temperature to it, the combustion processes occurring there would be negligible. In addition, it is doubtful whether

Table 8.1 Value of Mean Residence Time and Transfer Function for Each Experimental Run

Run no.	τ (ms)	Value of Transfer Function		
		$\tau s = 1$	$\tau s = 2$	$\tau s = 3$
1	14.6	0.811	0.748	0.702
2	14.2	0.626	0.474	0.385
3	13.5	0.764	0.666	0.598
4	15.7	0.652	0.523	0.453
5	14.1	0.710	0.581	0.495
6	15.6	0.803	0.745	0.704
7	11.4	0.627	0.470	0.379

Table 8.2 Best Configuration for Each Experimental Run and Values of its Transfer Function

Run no.	Configuration (see fig. 8.4)	Parameters			Transfer Function Value		
		w	τ_A/τ_B	τ_C/τ_B	$\tau s = 1$	$\tau s = 2$	$\tau s = 3$
1	I	0.15	11	0.125	0.811	0.751	0.700
2	II	0.20	11	0.125	0.627	0.478	0.384
3	I	0.15	5	0.125	0.763	0.668	0.588
4	II	0.30	15	0.125	0.650	0.528	0.447
5	II	0.15	25	0.125	0.707	0.581	0.492
6	I	0.15	10	0.125	0.806	0.743	0.690
7	II	0.15	12	0.125	0.628	0.472	0.373

Table 8.3 Parameters of Best Configuration for Each Run

Run	Configuration (see fig. 8.4)	Bypass Parameter w	Mean Residence Time of Reactor Elements (ms)			
			τ_A	τ_B	τ_C	τ_D
1	I	0.15	84.2	7.66	0.957	6.6
2	II	0.20	47.3	4.30	0.537	5.9
3	I	0.15	67.1	13.4	1.68	6.1
4	II	0.30	42.1	2.81	0.350	9.2
5	II	0.15	72.6	2.91	0.363	4.9
6	I	0.15	88.8	8.88	1.11	5.2
7	II	0.15	47.1	3.92	0.490	4.9

even the combustion products from A would be able to ignite the mixture in the short time available. Furthermore, combustion in plug flow reactors is inherently unstable (unless the feed has been preheated above the ignition temperature).

(iii) The plug flow reactor at the exit end of each configuration has been simulated as a series of CSTRs with mean residence times as given in Tables 8.4 to 8.7 (Reactor D is split up into D1, D2 etc.). The main reason for this is the fact that a one-dimensional combustion program was not available for rigorous calculation of the plug flow region, and it was not considered justified to develop such a program as it was possible to model the PFR by means of CSTRs. The mean residence time of reactor D was split up into increments of approximately 1 ms. This was considered a sufficiently fine division for estimation of the evaporative efficiency and combustion products, in particular the NO emissions. A test was carried out to see the effect of reducing the incremental time to 0.5 ms, and this further reduction produced negligible change in the results, confirming the above assumption. Further justification with respect to prediction of nitric oxide emissions is provided by the paper of Pratt et al., who show (90; figure 5) that the NO emissions predicted from a single perfectly stirred reactor are of the same order as those from a plug flow reactor for mean residence times less than about one millisecond.

Table 8.4 Summary of Results for Model of Run 2

Reactor Element	A	B	D1	D2	D3	D4	D5	D6 (exit)	Total or overall value for run
Mean residence time (ms)	47.3	4.3	1.0	1.0	1.0	1.0	1.0	0.9	20.1
Equivalence ratio, ϕ	0.472	0.804	0.891	0.942	0.971	0.987	0.996	1.00	1.0
Temperature (^{o}K)	1428	1931	2074	2157	2204	2230	2244	2250	
Efficiency, ε	0.960	0.750	0.428	0.440	0.444	0.445	0.448	0.447	
Cumulative Efficiency, ε_{cum}	0.192	0.798	0.885	0.935	0.964	0.980	0.989	0.994	0.994
Nitric oxide mole fraction (ppm)	10.7	35	51	73	95	115	134	150	150
Volume of Reactor Element (cm^3)	2337	723	182	190	194	197	198	179	4200

Table 8.5 Summary of Results for Model of Run 4

Reactor Element	A	B	D1	D2	D3	D4	D5	D6	D7	D8	D9 (exit)	Total or overall value for run
Mean Residence Time (ms)	42.1	2.81	1.0	1.0	1.0	1.0	1.0	1.0	1.0	1.1	1.1	24.9
Equivalence Ratio (ϕ)	.550	.670	.766	.825	.860	.880	.891	.898	.901	.904	.905	0.9
Temperature (^{o}K)	1579	1710	1882	1990	2057	2099	2126	2143	2154	2161	2166	
Efficiency (ε)	.959	.633	.405	.419	.425	.431	.435	.436	.438	.463	.463	
Cumulative Efficiency (ε_{cum})	.288	.738	.844	.910	.948	.970	.983	.991	.995	.997	.999	0.999
Nitric Oxide Mole Fraction (ppm)	15.2	10.9	15.3	24	35	47	59	71	82	94	105	105
Volume (cm^3)	2797	460	181	192	199	203	206	207	208	209	210	5072

Table 8.6 Summary of Results for Model of Run 5

Reactor Element	A	B	D1	D2	D3	D4	D5 (exit)	Total or Overall Value
Mean Residence Time (ms)	72.6	2.91	1.0	1.0	1.0	1.0	0.9	19.0
Equivalence Ratio ϕ	0.398	0.874	1.03	1.11	1.13	1.14	1.14	1.5
Temperature (^{o}K)	1279	2001	2189	2234	2235	2229	2222	
Efficiency	0.970	0.675	0.442	0.445	0.447	0.446	0.420	
Cumulative Efficiency	0.145	0.723	0.845	0.914	0.952	0.974	0.985	0.985
Nitric Oxide Mole Fraction (ppm)	8.9	46	73	81	84	86	87.5	87.5
Volume (cm^3)	2882	427	162	168	168	168	151	4062

Table 8.7 Summary of Results for Model of Run 7

Reactor Element	A	B	D1	D2	D3	D4	D5 (exit)	Total or Overall Value
Mean Residence Time (ms)	47.1	3.92	1.0	1.0	1.0	1.0	0.9	16.3
Equivalence Ratio ϕ	0.44	0.95	1.05	1.16	1.17	1.18	1.19	1.20
Temperature (^{o}K)	1362	2101	2255	2284	2287	2281	2274	
Efficiency	0.957	0.749	0.449	0.453	0.453	0.451	0.425	
Cumulative Efficiency	0.144	0.786	0.882	0.936	0.965	0.981	0.989	
Nitric Oxide Mole Fraction (ppm)	8.6	99	135	147	156	161	164	164
Volume (cm^3)	1784	605	168	172	172	171	154	3226

Calculated results for runs 1, 3 and 6 have not been presented. The reactor flow configuration for each of these runs corresponds with model I of figure 8.4 which has a very high bypass. In each case 85% of the fuel feed passes through plug flow reactors C and D, and as a result the calculations indicate that it remains unburnt. The calculations show that most of the other 15% of the fuel burns in reactor A and that the combustion reaction is already quenched in reactor B as there is insufficient fuel left to heat up the secondary reverse air entering B. The relatively cold ($< 800^{\circ}K$) products of reactor B are then unable to ignite the fuel entering D from C.

The predictions resulting from this configuration (I) were not observed in practice, the combustion appearing stable and effectively complete. Other model configurations which would fit the experimental results for these runs were studied. Each type of configuration considered necessarily accounted for the extremely high short circuiting indicated by the results, and therefore resulted in the same type of predictions as configuration I. The results for runs 1, 3 and 6 remain, for the time being, unexplained. Configuration I is abandoned as unfeasible for the chamber used, on the grounds of its incorrect predictions.

Modelling of the combustion chamber using configuration II (figure 8.4) indicates some general features which may be used to elucidate the factors determining chamber performance. Referring to the numerical results presented in Tables 8.4 to 8.7, these features may be stated as follows:

(i) The combustion chamber is stabilized by a relatively high mean residence time ($\tau_A \sim 50$ ms) recirculation region in which more than 95% of the fuel spray entering it evaporates. The mixture in this region is very fuel lean due to the fact that most of the fuel (70-85%) bypasses it, while about 50% of the total air enters it from the forward secondary air input.

(ii) The products of reactor A pass to a second stirred tank B ($\tau \sim 2$-4 ms) where they mix with the bypass stream (from plug flow reactor C) and the remainder of the secondary air and ignite the fuel in the cold bypass stream, evaporating 60-75% of the entering fuel spray. The gas leaving reactor B contains only 20-30% of the spray volume fed to the chamber.

(iii) The products of reactor B pass into a plug flow reactor (D) which is split up for computation into a series of CSTRs with $\tau \approx 1$ ms. Each of these has an evaporative efficiency of 40-50%, so that by the time the combustion gases have reached the fourth or fifth CSTR, less than 2% of the spray volume remains.

(iv) The temperature and local equivalence ratio, together with the mean residence time determine the amount of nitric oxide formed in each reactor element. These effects may be qualitatively assessed by comparison of NO levels in corresponding reactor elements in Tables 8.4-8.7, and their relationship to the above parameters.

(v) The reactor flow configuration allows an estimate to be made of the volume of the chamber which is actually used for the combustion process (i.e. that part which is reached by fuel). The volumes of each reactor element and the respective totals for each run are given in Tables 8.4 to 8.7, and range from 3.2 to 5.1 x 10^3 cm^3, which represents 30 to 50% of the actual chamber volume.

8.4: Evaluation of Chamber Models

8.4.1: Criterion for Model Assessment. The criterion to be used for assessing the models developed for the combustion chamber is the extent of agreement between the predicted and measured emissions of nitric oxide.

The reasons for selecting this particular criterion are as follows:

(i) Nitric oxide emissions are a sensitive function of the time/temperature/composition history of the combustion gases.

(ii) The measurement of nitric oxide emissions was simple to carry out accurately, and the level of emissions was indeed found to be sensitive to the values of the operating parameters.

(iii) Nitric oxides are an undesirable by-product of combustion systems, the minimisation of which is one of the aims of modern combustion engineering. Knowledge of emission levels and how they are affected by changes in the design and operation of a particular combustion chamber is therefore important.

(iv) The combustion efficiency of the chamber (and correspondingly, evaporative efficiency in the model) is very close to 100% under all the conditions used. The carbon-hydrogen-oxygen species (C-H-O) product composition and temperature have been found to be (within the accuracy of measurement) those predicted by the water-gas equilibrium for the overall equivalence ratio (55), irrespective of the values of other parameters. The temperature, efficiency and C-H-O product composition would therefore not provide suitable criteria for model evaluation.

Table 8.8 Measured and Predicted Nitric Oxide Emissions

Ratio of Forward to Reverse Secondary Air Mass Flow rates	ϕ = 0.9			ϕ = 1.0			ϕ = 1.2		
	Run No.	NO Emissions (ppm by volume)		Run No.	NO Emissions (ppm by volume)		Run No.	NO Emissions (ppm by volume)	
		Measured	Predicted		Measured	Predicted		Measured	Predicted
4/5	8	40		2	64	150	7	89	164
1/1	4	35	105	1	52		5	45	87.5
5/4	9	29		3	50		6	73	

8.4.2: Comparison of Model Predictions with Results. Table 8.8 shows the measured and estimated levels of nitric oxide emissions from the combustion chamber, for different values of ϕ and secondary air distribution. Values of nitric oxide emissions were measured for the complete set of the above parameters, and all these measurements are included, even though detailed modelling was only carried out for four conditions.

Comparison between the corresponding calculated and measured results indicates that the model correctly predicts the trends in nitric oxide emissions with changes in the parameters varied. Quantitatively, the model overestimates nitric oxide emissions by a factor of about 2, except for run 4, where the overestimation is by a factor of 3.

8.4.3: Effects of Model Assumptions on Quantitative Prediction of Nitric Oxide Emissions.

8.4.3.1: Kinetic rate data: One possible source of the systematic overestimation of nitric oxide emissions is the uncertainty in the rate constants used for the nitric oxide formation kinetics. The critical evaluation of rate data by Baulch et al. (91) indicates that the uncertainty of the rate constant in the first reaction of Table 3.1 (which is the rate limiting NO formation reaction in most elements of the model) is a factor of two or more, and this could provide a plausible explanation.

8.4.3.2: Micromixing: The errors in estimated NO emissions from a reactor resulting from an incorrect micromixing assumption depend on the mean equivalence ratios in the reactor. If the mean equivalence ratio is close to stoichiometric the nitric oxide levels are overestimated, while if it is not (especially on the

fuel lean side), nitric oxide levels will be underestimated. This arises from the highly non-linear dependence of nitric oxide formation kinetics on temperature, and through this on equivalence ratio. For example, if at an overall equivalence ratio of 0.7, there is non-uniformity of mixing, the regions which have a local ϕ nearer 1.0 will produce a much greater additional amount of NO (relative to $\phi = 0.7$) than the reduction in the NO produced by the regions having correspondingly lower values of ϕ. Detailed modelling of this effect has been carried out for gas turbine engines by Heywood and co-workers (35, 92), and these calculations have confirmed the above effects. Figure 8.5 shows typical results obtained from the model used by the above workers (which has been described in chapter 3). The parameter s_0 is a measure of the divergence from micromixing; $s_0 = 0$ corresponds to perfect micromixing.

Tables 8.4 to 8.7 show that most NO is produced at near stoichiometric conditions, where not taking account of mixing non-uniformities would lead to an overestimation of NO emissions. The systematic overestimation of the model indicates that the micromixing assumption may not in fact be justified. This explanation, if accepted, would still allow the model to be used for estimating trends in emissions and efficiency provided that the basic model configuration and equivalence ratio distribution is not markedly altered between different operating conditions. The latter was found to be the case for the range of conditions studied and adds no further constraint to the application of the model, so that it is doubtful that the additional complexity introduced by micromixing considerations would be justified if the model is required for prediction of trends, rather than absolute values which would in any case be difficult to predict at present due to uncertainties in kinetic rate constants.

8.4.3.3: Pyrolysis: The instantaneous pyrolysis assumption (and also the assumption that the heating-up period of the drops in the spray is negligible) would both lead to overestimation of NO emissions by allowing relatively more time for the gas phase reaction kinetics to proceed. The advantage to be gained by attempting to estimate these processes more accurately is probably not justified considering the present state of knowledge of pyrolysis mechanisms and rate data.

8.4.3.4: Assumption of plug flow at exit: The plug flow residence time of the model (reactor element D) is considerably greater in Run 4 than the corresponding reactor in the flow models of the other runs ($\tau_D \sim 9$ ms compared with 5-6 ms for other runs). It is possible that the assumption made in section 8.1 that the plug flow section is entirely at the exit end of the chamber is not correct or is less

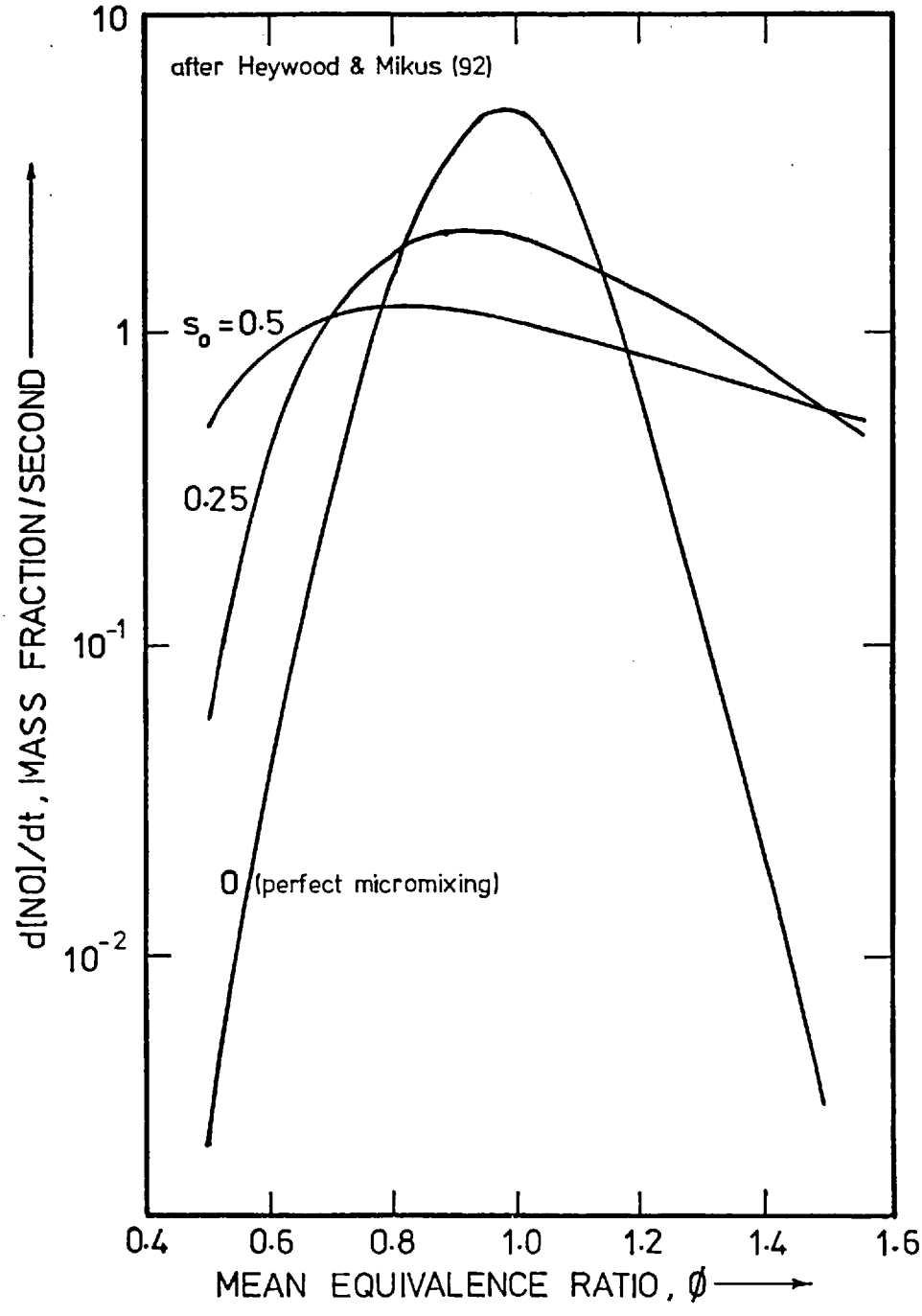

FIGURE 8·5 Effect of micromixing on nitric oxide formation rate.

correct for the conditions of Run 4. This would explain the higher degree of overestimation of NO in this run as follows. The NO mole fraction increases rapidly with residence time in the plug flow region of Run 4 (reactors D1 to D9, Table 8.5), due to the availability of O_2 (and O atoms) at the fuel lean conditions present. If it were assumed that the series plug flow at the chamber exit is limited to 5 ms, (with any additional plug flow portion at the entry) the model would predict a nitric oxide emission level of 59 ppm, which has the same relative value to the measured level as the other predictions. This further assumption, while giving more credence to the model, would require experimental confirmation. Such confirmation could be obtained from stimulus response experiments on the forward and reverse secondary air, or from internal measurements in the combustion chamber. This is further discussed in chapter 9.

8.4.4: Additional Points Arising from Model Predictions. A number of points additional to those above are amplified by the detailed summary of the model predictions given in Tables 8.4 to 8.7.

The effect on NO emissions of increasing the amount of time available in plug flow reactor D is strongly dependent on the overall value of equivalence ratio. For near stoichiometric conditions, the high temperature is very conducive to the kinetics and providing there is sufficient oxygen present to provide O atoms for the main NO formation reaction, the amount of NO emitted can increase by the order of 20 ppm/ms increment in available time (Run 2). For fuel rich conditions even if the temperature is high ($\sim$2200^{o}K in Run 5) the incremental NO formation is only 6 ppm/ms on average, compared with about 12 ppm/ms for the lower temperature ($\sim$2100^{o}K) for Run 4. This would indicate that if the NO formation in the initial part of the system can be kept to a minimum, (say, by partial combustion of the fuel at equivalence ratios far from stoichiometric) a relatively large amount of time can subsequently be provided for completion of combustion without seriously increasing the NO emissions. This is a principle that has been used in a number of systems designed to reduce NO emissions, among which is the class of two stage combustion systems.

The effect of the ratio of forward/reverse secondary air may also be explained in terms of the model configuration. The results show a fairly definite decrease in NO emissions as this ratio is increased, due to the primary recirculation zone (reactor element A) becoming more fuel lean with a consequent decrease in temperature.

The fact that the same configuration (with variations in the parameters) successfully predicted the effects of different forward/reverse secondary air ratios indicates that this ratio has only a second order effect on the aerodynamics. The sensitivity of NO emissions to the feed distribution of secondary air may therefore be attributed to the resulting equivalence ratio distribution among the various regions in the chamber (corresponding to the reactor elements of the model). As the relative amount of forward secondary air is increased, the equivalence ratio in the fuel lean recirculation zone tends to decrease further, lowering the temperature and the NO emissions in the early part of the system. This effect carries through the system as the subsequent reactor elements have a relatively short mean residence time, and especially in the case of overall fuel lean combustion, are not conducive to NO formation. Minimization of NO production in the early part of the chamber tends to produce the same result with regard to the chamber products.

Other results of the detailed modelling of the reactor configuration which warrant discussion are the estimates of actual volume used for the combustion reaction ("active" volume). The total "active" volume ranges from 3.2 to 5.1 x 10^3 cm^3, as compared with an actual chamber volume of 9.1 x 10^3 cm^3. It is interesting to note that the result for Run 4 is considerably in excess of the other results and if the plug flow region at the exit is reduced to the extent indicated earlier in this section, the "active" volume is reduced to a value of about 4.2 x 10^3 cm^3, which is more in line with the values for the other runs. This reinforces the earlier conjecture relating to overestimation of the exit plug flow portion of the model for Run 4.

These results indicate that less than 50% of the reactor volume is utilized for combustion under the operating conditions used. The atomiser spray angle and momentum, which determine the overall aerodynamics, would require adjustment to achieve a greater utilization of chamber volume and a corresponding increase in the total achievable heat release. In order to maintain the same fine drop size distribution, while increasing the spray angle, a smaller size atomiser of similar design would be called for.

9. CONCLUSIONS AND RECOMMENDATIONS FOR FURTHER WORK

This chapter will present the main conclusions of this work and discuss points which are relevant to the general application of the modelling techniques developed.

9.1: Main Conclusions

The main results of this work may be summarised as follows.

(i) A novel experimental method has been developed to carry out stimulus response experiments on high intensity combustion chambers under operating conditions. The method has an accuracy of the order of one millisecond, so that the flow configuration of chambers with very small mean residence times may be identified.

(ii) Stimulus response experiments were carried out on a high intensity spray combustion chamber burning gas oil, under a number of operating conditions. For each condition, a reactor flow configuration was selected from feasible alternatives based on the geometry and aerodynamics of the chamber. Identification was carried out by matching of values of transfer function in the Laplace domain. The best configuration was found to be two stirred tanks in series with plug flow bypass of the first, followed by a plug flow reactor.

(iii) A model for the high intensity combustion of a size distributed spray in stirred and plug flow reactors was developed. Predicted effects of variations in a number of combustion parameters on the performance of a stirred reactor burning gas oil were presented.

(iv) For each experimental run, the spray combustion model was used to calculate the conditions in each reactor element of the derived flow configuration. The temperature, efficiency and composition in each reactor element, and at the chamber exit were predicted. Trends of predicted nitric oxide emissions (used as the criterion of model accuracy) with variations in equivalence ratio and air distribution agreed with those measured. Furthermore, the model allowed these trends to be explained in terms of the distribution of equivalence ratio and residence time in various parts of the chamber. The effects of changes in parameters other than those varied might therefore be predicted by the model with reasonable confidence.

(v) To improve the model so that quantitative prediction of nitric oxide emissions might be possible for high intensity spray combustion chambers in general, it is suggested that the following factors be further considered:-

(a) Allowance for mixing nonuniformities in reactor elements.

(b) Accuracy of data on kinetic reaction rates and mechanisms.

and (c) Inclusion of reliable pyrolysis mechanisms and rates when these become available.

9.2: Further Applications and Development

In addition to possible improvements in the combustion model itself (summarised above), a possible limitation to the applicability of the spray evaporation equation to other chambers is the one parameter drop size distribution equation which was used for the spray. This equation is not capable of accurately describing sprays whose size distribution has a great or lesser dispersion about the mean (than that fixed by a value of b = 2 in equation 3.4). A possible approach which would allow the model to be used is to consider the spray as composed of two or more groups, each group being adequately described by the one parameter equation used. It is likely that many of the distributions found in practice could be well approximated by summing only two or three one parameter distributions, appropriately weighted relative to one another. The evaporation from each group is calculated separately, and the appropriately weighted sum used to determine the rate of fuel addition in each reactor. This approach would appear worthwhile as the form of the size distribution used, when combined with the drop evaporation rate equation leads to a very simple explicit relation for spray evaporation efficiency in a stirred or plug flow reactor element.

With regard to the stimulus response experiments, the analysis of sensitivity to errors (in Appendix C) shows that the input pulse duration was excessively large relative to the mean residence time of the reactor flow configuration in the chamber. Decreasing the input pulse duration would have resulted in greater certainty in the precise values of the parameters of the derived flow configuration. The pulse duration could be reduced by improving the injection system, and in particular by reducing the amount of tracer required by using a detector with greater sensitivity.

Additional stimulus response experiments, on the secondary air inputs would provide valuable information on the chamber flow configuration. In particular the

results would indicate how the secondary air feeds are distributed between the various reactor elements on entry to the chamber, this having been intuitively assumed in the absence of these results. Furthermore, the existence and characteristics of some of the reactor elements in the configuration (those through which the particular stream passes) could be confirmed.

Further confirmation of the existence of various stirred or plug flow sections could be obtained from tracer injection and/or sampling inside the chamber, but such experiments would involve considerable complication with regard to experimental technique and also interference of the probes etc. with the system being measured.

If measurements of local temperature and species concentrations throughout the chamber were available, comparison with the model predictions could identify specific shortcomings in the model. For example, spatial or temporal variations in temperature or species concentrations in a well stirred region would indicate that the micromixing assumption is not valid for that region.

APPENDIX A: CALCULATION OF TRANSFER FUNCTIONS OF REACTOR CONFIGURATIONS

(a) Two CSTRs in recycle (figure 2.3(a))

Reactors A, B are CSTRs and R is the recycle ratio.

Overall mean residence time,

$$\tau = (R + 1)\tau_A + R\tau_B \tag{A.1}$$

let $$B_1 = \frac{\tau_B}{\tau_A} \tag{A.2}$$

$$\therefore \quad \tau = (R + 1 + RB_1)\tau_A \tag{A.3}$$

let $$F_1 = 1/(1 + R(B_1 + 1)) \tag{A.4}$$

$$\therefore \quad \tau_A = F\tau \tag{A.5}$$

from figure 2.2(c)

$$G_1(s) = \frac{G_A(s)}{(1 + R) - RG_A(s)G_B(s)} \tag{A.6}$$

from equations 2.5 and A.5

$$G_A(s) = \frac{1}{\tau_A s + 1} = \frac{1}{F_1\tau s + 1} \tag{A.7}$$

from equations 2.5, A.5 and A.2

$$G_B(s) = \frac{1}{\tau_B s + 1} = \frac{1}{B_1F_1\tau s + 1} \tag{A.8}$$

Substituting equations A.7 and A.8 into equation A.6 and rearranging

$$G_1(s) = \frac{B_1F_1\tau s + 1}{(1 + R)(B_1F_1\tau s + 1)(F_1\tau s + 1) - R} \tag{A.9}$$

(b) Two CSTRs in series with plug flow bypass of the first (figure 2.3(b))

Reactors A and B are CSTRs; reactor C is a PFR.

Bypass fraction = $1 - w_2$

$$\tau = w_2\tau_A + (1 - w_2)\tau_C + \tau_B \tag{A.10}$$

let $$B_2 = \frac{\tau_B}{\tau_A} \tag{A.11}$$

$$C_2 = \frac{\tau_C}{\tau_B} \tag{A.12}$$

$$F_2 = 1/(w_2 + (1 - w_2)B_2C_2 + B_2) \tag{A.13}$$

$$\therefore \quad \tau = \tau_A/F_2 \tag{A.14}$$

Using the rules of figure 2.2

$$G_2(s) = [w_2(\frac{1}{F_2\tau s + 1}) + (1 - w_2)\exp(-B_2C_2F_2\tau s)] \frac{1}{B_2F_2\tau s + 1} \tag{A.15}$$

APPENDIX B. OPTIMUM RANGE OF $s\tau$ FOR DISCRIMINATION BETWEEN MODELS IN THE LAPLACE DOMAIN

When attempting to discriminate between various feasible models in the Laplace domain, the problem arises of what range or value of $s\tau$ to use. In many instances it is likely that a range of $s\tau$ will exist where the difference between the alternative transfer functions is relatively large, so that in this range of $s\tau$ it is less difficult to decide which model best matches the experimentally derived transfer function. If the value of the transfer function at only one $s\tau$ was to be used, then the comparison should be made at the $s\tau$ where a maximum difference between the alternatives exists.

As an example, consider the plausible models to be ℓ and $\ell + 1$ CSTRs in series.

The transfer functions of these models are

$$G_{\ell}(s) = (1 + \frac{s\tau}{\ell})^{-\ell} \tag{B.1}$$

and

$$G_{\ell+1}(s) = (1 + \frac{s\tau}{\ell + 1})^{-(\ell+1)} \tag{B.2}$$

and the difference is given by

$$\Delta G_{\ell}(s) = G_{\ell}(s) - G_{\ell+1}(s) \tag{B.3}$$

Figures B.1 and B.2 show $G_{\ell}(s)$ and $\Delta G_{\ell}(s)$ respectively (for various values of ℓ), and these show that a maximum does indeed exist for $\Delta G_{\ell}(s)$, enabling an optimum value of $s\tau$ to be selected according to the above criterion. The optimum $s\tau$ for the alternative models used for this example varies between 2 and 3.

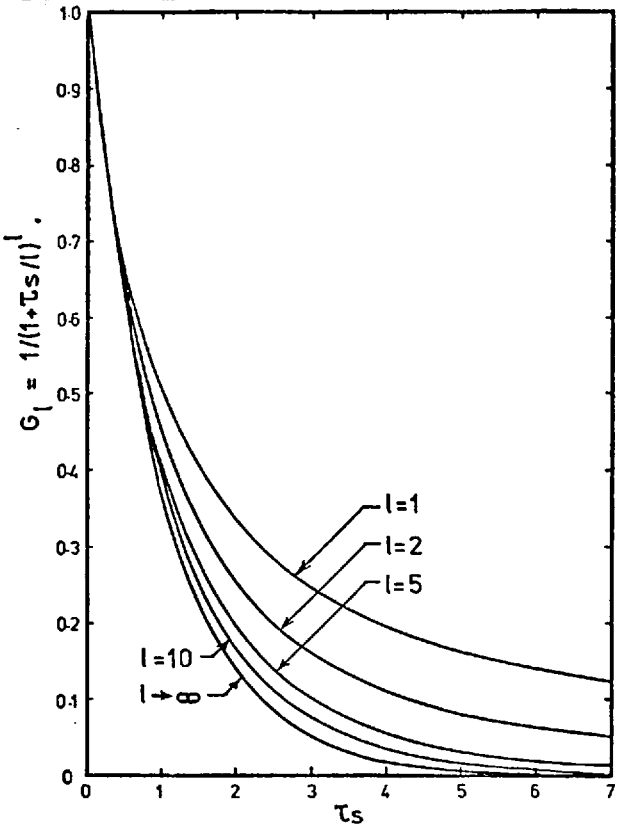

FIGURE B.1 Transfer function of l CSTRs in series.

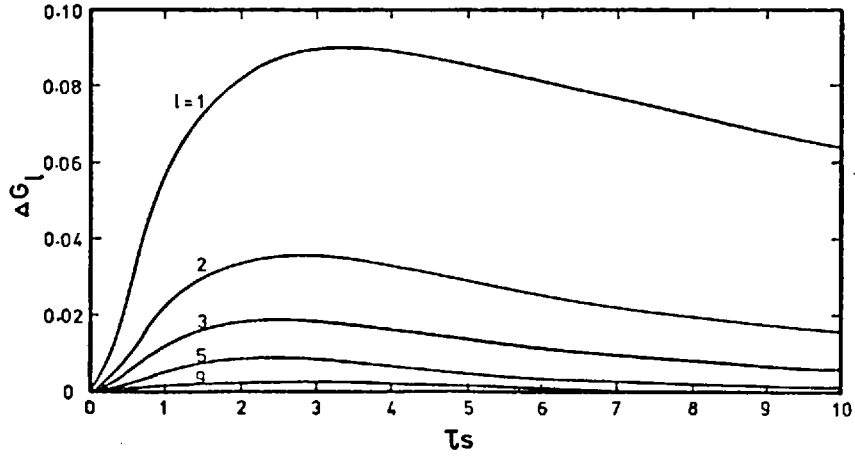

FIGURE B.2 Difference between transfer functions of l and l+1 CSTRs in series.

APPENDIX C: ERRORS IN EXPERIMENTAL TRANSFER FUNCTIONS

This appendix will demonstrate how the sensitivity analysis in chapter 2 may be applied to determine the accuracy of model identification in the Laplace domain.

A model and its parameters are identified from values of G(s) which is determined from the ratio of the LTO and the LTI, so that errors in the latter will result in some corresponding error in parameters of the identified model, and possibly in the model itself. The errors in the LTI and LTO depend on the accuracy of measurement of the pulse shapes, and also on the sensitivity of each as defined in chapter 2. In this example, it will be assumed that the sensitivity of the actual pulse shapes is well approximated by that of the asymmetrical pulse shown in chapter 2, so that the measurement error in each may be characterised in terms of the error of the pulse spread, t_p.

The value(s) of s used for the model identification is determined by both the value of τs to be used and on the value of τ of the system being identified. τ is obtained as the difference between the mean times, $\bar{t}_p$, of the output and input pulses.

The accuracy of $\bar{t}_p$ for each pulse should be estimated statistically from a large number of experimental determinations. Only one duplicate determination was actually carried out, this being on the input pulse. This will be used to estimate the accuracy of both input and output pulses on the grounds that they are both of similar duration and hence their errors can be considered to be the same. This approach is not claimed to be rigorous, and a single duplication is certainly insufficient for estimation of the result to any degree of statistical significance. The aim of the exercise is to demonstrate the approach, which relates the uncertainty in the parameters of a model identified by Laplace domain analysis, to errors in pulse shape measurement.

For the stimulus response experiments performed, the two input pulse determinations (Tables H.1 and H.9) have mean times $\bar{t}_p$ of 38.5 and 39.4 ms respectively. The relative error in $\bar{t}_p$ will therefore be assumed to be ±1 ms in 40 ms or 2.5% for both the input and output pulses. A typical value of $\bar{t}_p$ for the output pulses is 55 ms, so that τ is given by 55-40 $\sim$ 15 ms.

Using the sensitivity curve in figure 2.8 relating to the asymmetrical pulse shape, the relative errors in LTI and LTO for the above pulse tests may be

calculated as follows:

At $\tau s = 1$

$$(st_p)_{input} = \frac{1}{\tau}(2\bar{t}_p)_{input}$$

$$= \frac{80}{15} = 5.3$$

Similarly

$$(st_p)_{output} = \frac{1}{\tau}(2 \times 55)$$

$$= \frac{110}{15} = 7.3$$

From figure 2.8

Sensitivity of the input = 1.1

Sensitivity of the output = 1.3

$(E_r)_{LTI}$ = relative error in LTI = 0.025 x 1.1 = 0.0275

$(E_r)_{LTO}$ = relative error in LTO = 0.025 x 1.3 = 0.0325

since $G(s) = \frac{LTO}{LTI}$

$(E_r)_{G(s)}$ = relative error in G(s).

$$= \sqrt{(E_r)^2_{LTO} + (E_r)^2_{LTI}}$$

$$\therefore (E_r)_{G(s)} = \sqrt{.0275^2 + .0325^2}$$

$$= 0.042 = 4.2\%$$

Similarly, at $\tau s = 2$, $(E_r)_{G(s)} = 5.3\%$

at $\tau s = 3$, $(E_r)_{G(s)} = 5.8\%$

The above will be applied to the results of RUN 2 by way of example. From Table 8.1, G(s) has values of 0.626, 0.474 and 0.385 at $\tau s = 1$, 2 and 3 respectively. Applying the above percentage errors, the range of values of G(s) at different values of τs are as follows.

$\tau s = 1 \quad G(s) = 0.626 \pm 4.2\%$

i.e. $0.600 < G(s) < 0.652$

$\tau s = 2 \quad G(s) = 0.474 \pm 5.3\%$

i.e. $0.459 < G(s) < 0.499$

$\tau s = 3 \quad G(s) = 0.385 \pm 5.8\%$

i.e. $0.358 < G(s) < 0.412$.

The band of values of G(s) as described by the above ranges is shown in figure C.1. This band may be used to determine a range of values for parameters of the model being identified. The range corresponds to the uncertainty in the parameter values due to errors in pulse shape measurement.

If an accurate analysis of the variation in the parameters w, τ_A/τ_B, τ_C/τ_B is required, it is necessary to carry out a factor analysis to show which combination leads to extreme values of G(s) within the band. This was in fact attempted, and one example is quoted here, where w and τ_C/τ_B are constant (at 0.2 and 0.125 as fixed in the identification [Table 8.3]). The range of the third parameter τ_A/τ_B for which G(s) lies within the band shown in figure C.1 is

$$9.6 < \tau_A/\tau_B < 12.8$$

Using the equations given in Appendix A and the overall value of τ for Run 2 (14.2 ms), the ranges of τ_A and τ_B corresponding to the above range of τ_A/τ_B are

$\tau_A/\tau_B = 9.6; \quad \tau_A = 45.2$ ms, $\quad \tau_B = 4.7$ ms

$\tau_A/\tau_B = 12.8; \quad \tau_A = 49.7$ ms, $\quad \tau_B = 3.9$ ms

For the model identified for Run 2:

$\tau_A/\tau_B = 11.0; \quad \tau_A = 47.3$ ms, $\quad \tau_B = 4.3$ ms.

Summarising, the effect of an error of 2.5% in both the input and output pulse measurements leads to a range of values of the model parameters τ_A and τ_B as follows

$45.2 < \tau_A < 49.7$ ms (compared with $\tau_A = 47.3$ ms)

$4.7 < \tau_B < 3.9$ ms (compared with $\tau_B = 4.3$ ms)

If the input pulse had been short in duration relative to the mean residence time of the chamber, the width of the band of G(s) would have been much narrower. For example, had the input pulse mean time, $\bar{t}_p$, been 5 ms the percentage relative

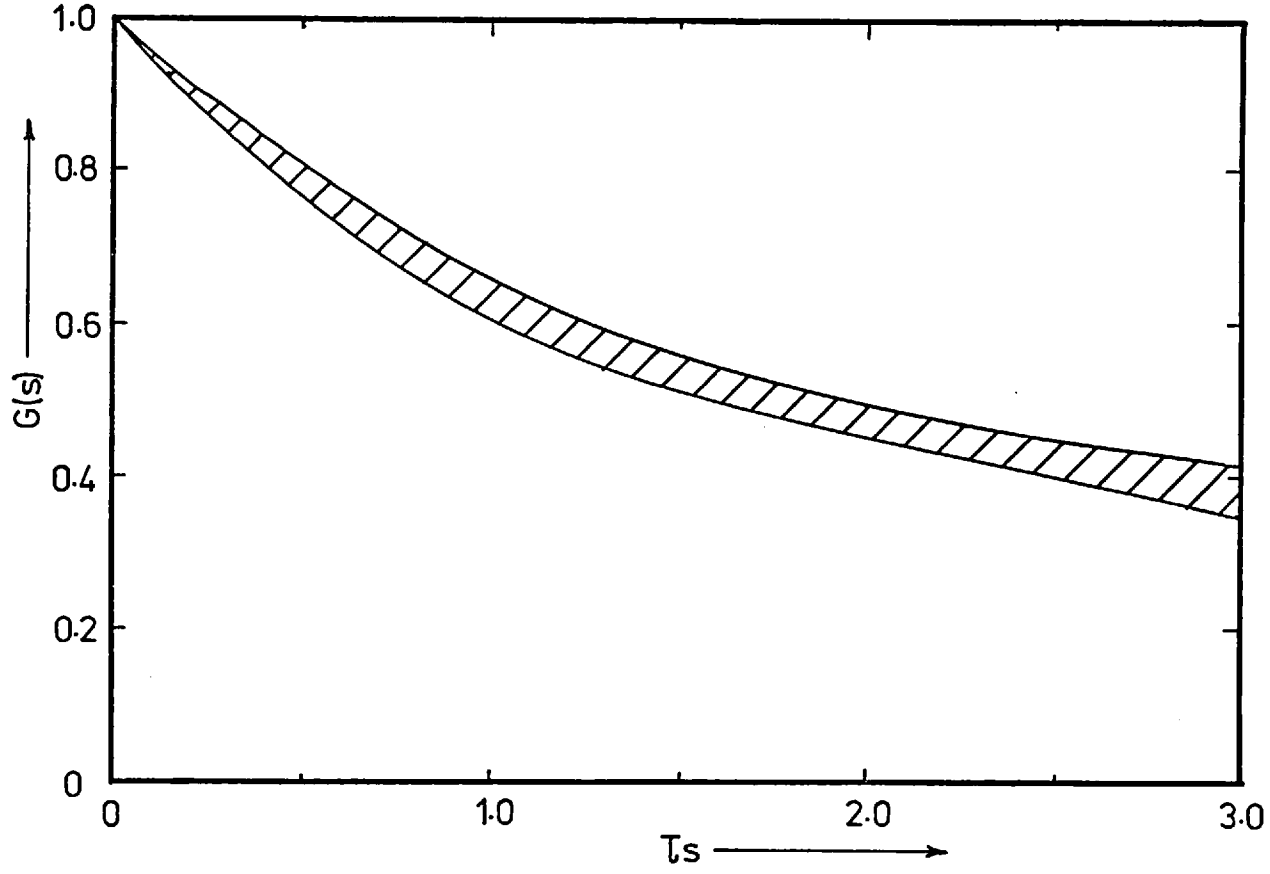

FIGURE C.1 Band of G(s) resulting from errors in pulse measurement.

error in G(s) for 2.5% relative error in t_p would have been:

$$\text{at} \quad \tau s = 1, \quad (E_r)_{G(s)} = 2.0\%$$

$$\tau s = 2, \quad (E_r)_{G(s)} = 3.0\%$$

$$\tau s = 3, \quad (E_r)_{G(s)} = 3.8\%$$

compared with 4.2%, 5.3% and 5.8% respectively for the actual input pulse ($\bar{t}_p \sim 40$ ms).

It is obvious that the narrower band of G(s) resulting from a shorter duration input pulse results in a smaller range of values of model parameters within which the actual value is expected to be.

APPENDIX D: SOME PROPERTIES OF THE DROP SIZE DISTRIBUTION EQUATION

The drop size number frequency equation used in this work is of the form

$$G = bnD^{n-1}\exp(-bD^n) \tag{D.1}$$

The fractional number undersize is given by

$$\int_0^D GdD = 1 - \exp(-bD^n) \tag{D.2}$$

and the fraction number oversize = $\exp(-bD^n)$ (D.3)

Volume fraction oversize in terms of number frequency parameters

If it is necessary to fit an equation of the form of D.1 to experimental data relating to the fractional volume oversize, this must be calculated in terms of the parameters as follows.

$$\text{Volume fraction oversize} = \frac{\int_D^\infty GD^3dD}{\int_0^\infty GD^3dD} \tag{D.4}$$

Substituting G from equation D.1 and letting $f = bD^n$, (D.5)

$$\int GD^3dD = \int b^{-3/n}.f^{3/n}\exp(-f)df \tag{D.6}$$

from D.6 and D.5,

$$\text{Volume fraction oversize} = \frac{\int_{bD^n}^\infty f^{3/n}\exp(-f)df}{\int_0^\infty f^{3/n}\exp(-f)df} \tag{D.7}$$

$$= \frac{\gamma(1+\frac{3}{n},\ bD^n)}{\Gamma(1+\frac{3}{n})} \tag{D.8}$$

where $\gamma(A,X)$ is the incomplete gamma function, $\int_X^\infty e^{-\mu}\mu^{A-1}d\mu$.

For n = 2 (the form of D.1 used in this work), the volume fraction oversize is given by

$$\text{volume fraction oversize} = \frac{\gamma(\frac{5}{2},bD^2)}{\Gamma(\frac{5}{2})} \tag{D.9}$$

Equation D.9 was used to determine the best value of b to fit the number frequency distribution to the experimentally determined volume fraction oversize as shown in figure 5.3.

Evaporative mean diameter

The evaporative mean diameter is defined as

$$(\bar{D}_{31})^2 = \frac{\int_0^\infty GD^3 dD}{\int_0^\infty GDdD} \tag{D.10}$$

substituting for G in equation D.1 and letting $f = bD^n$

$$\bar{D}_{31}^2 = \frac{\int_0^\infty b^{-3/n} f^{3/n} \exp(-f)df}{\int_0^\infty b^{-1/n} f^{1/n} \exp(-f)df} \tag{D.11}$$

$$= \frac{\Gamma(1 + \frac{3}{n})}{\Gamma(1 + \frac{1}{n})} .b^{-2/n} \tag{D.12}$$

for n = 2

$$\bar{D}_{31}^2 = \frac{\Gamma(\frac{5}{2})}{\Gamma(\frac{3}{2})} .b^{-1} \tag{D.13}$$

but $$\Gamma(\tfrac{5}{2}) = \tfrac{3}{2}\Gamma(\tfrac{3}{2})$$

$$\therefore \quad \bar{D}_{31}^2 = \frac{1.5}{b} \tag{D.14}$$

APPENDIX E: EXAMPLE CALCULATION OF SPRAY COMBUSTION EFFICIENCY AND PRODUCTS IN A REACTOR CONFIGURATION

The steps in the calculation of the reactor configuration derived for Run 5 will be shown by way of example. The configuration as derived from stimulus response experiments (see chapter 7), and the relevant parameters for this run are shown in figure E.1.

(a) Calculation of mean residence time of each reactor element

Apart from the plug flow reactor D, the configuration is the same as that shown in figure 2.31, whose transfer function is given by equation 2.9. From the experimental results, τ_D = 4.9 ms and the mean residence time of the remainder of the configuration, τ_{ABC} = 14.1 ms.

From equation A.15 and data on figure E.1,

$$\tau_A = F_2\tau_{ABC}$$

$$= (w_2 + (1 - w_2)B_2C_2 + B_2)\tau_{ABC}$$

$$= 5.15 \times 14.1$$

$$= 72.62 \text{ ms}$$

$$\tau_B = \tau_A/25$$

$$= 2.91 \text{ ms}$$

$$\tau_C = 0.125\ \tau_B = 0.363 \text{ ms}.$$

(b) Calculation of Air Feed Distribution

The forward and reverse secondary air are assumed to enter reactors A and B respectively. From the overall equivalence ratio (ϕ = 1.2), the fuel flow rate (2.0 g/s) and the atomising air flow rate (4.0 g/s), the forward to reverse secondary air ratio (1/1), the forward and reverse secondary air are each calculated (in figure E.1) to be 10.0 g/s.

(c) Calculation of each reactor in the configuration

The mean residence time of and feed streams to each reactor element are now known, and these are dealt with in turn. Reactor A is solved first, then C, B and D. To solve each reactor, the mass feed rate and temperature of each feed species is required, and the solution is carried out as shown in figure 4.4.

OPERATING CONDITIONS

FUEL FEED RATE = 2.0 g/s

OVERALL ϕ = 1.2

$\therefore$ TOTAL AIR FLOWRATE = $\frac{2 \times 14.4}{1.2}$ = 24.0 g/s

ATOMISING AIR RATE = 4.0 g/s

$\therefore$ SECONDARY AIR RATE = 20.0 g/s

RATE OF FORWARD/REVERSE SECONDARY AIR = 1/1

$\therefore$ FORWARD SECONDARY AIR RATE = 10.0 g/s

REVERSE SECONDARY AIR RATE = 10.0 g/s

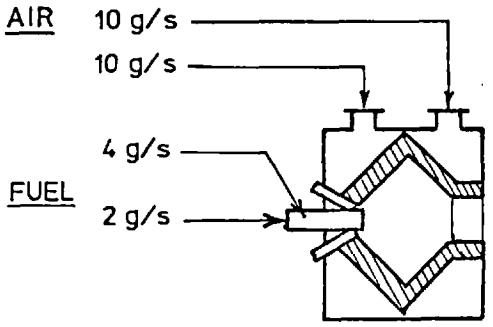

DERIVED FLOW CONFIGURATION AND ITS PARAMETERS

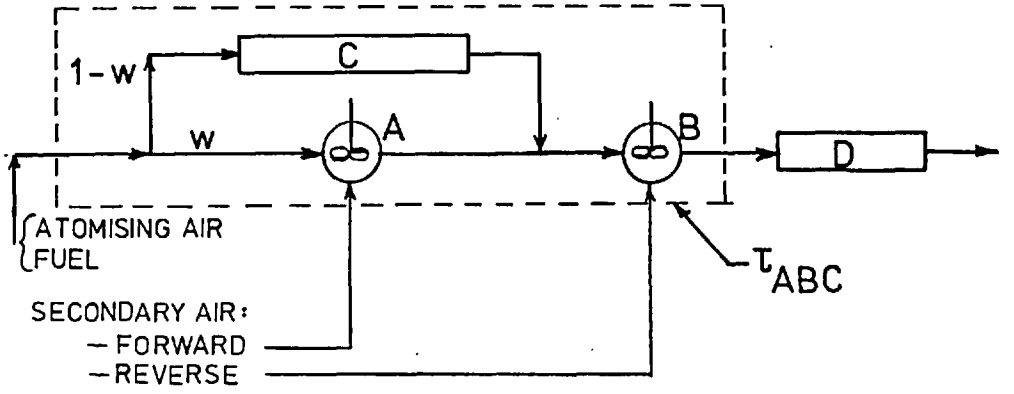

From time domain results (Table H.6)

τ_{ABC} = 14.1 ms

τ_D = 4.9 ms

From Laplace domain analysis (Table 8.2)

w = 0.15

τ_A/τ_B = 25.0

τ_C/τ_B = 0.125

Figure E.1. Operating Conditions and Derived Flow Configuration for Run 5

REACTOR A, is a CSTR with mean residence time of 72.62 ms

The feed streams comprise of: 15% of the atomising air
15% of the fuel
the forward secondary air.

Air feed: 0.15 x 4 = 0.60 g/s atomising
10.00 g/s secondary forward air
Total air 10.6 g/s comprising 2.495 g/s O_2
8.141 g/s N_2

Fuel feed: 0.15 x 2 = 0.30 g/s

Assuming fuel spray evaporation efficiency = 0.97,

the fuel available for combustion = 0.3 x 0.97
= 0.291 g/s

∴ Feed to reactor A is as follows:

$CH_{1.83}$	0.291 g/s	at	298°K
O_2	2.495 g/s	at	298°K
N_2	8.141 g/s	at	298°K

Using program CECPSR (section 4.5), the temperature in reactor A for the above feed is calculated to be 1279°K. To calculate the spray evaporation efficiency at this temperature, the drop evaporation constant is calculated using equation 3.3.

$$\kappa = \frac{8\bar{\lambda}}{\rho_\ell \bar{C}_p} \ln(1 + B_{ev}) \qquad (3.3)$$

where

$$B_{ev} = \frac{\bar{C}_p (T_g - T_\ell)}{L} \qquad (3.4)$$

The properties of the gas oil drops are

$\rho_\ell = 0.835$ g/cm^3

$L = 61.1$ cal/g

$T_\ell = 560$°K (50% distillation point)

The gas properties were calculated at the mean temperature between the gas and the drop, that is at (1279 + 560)/2 = 920°K. The specific heat capacity and thermal conductivity of the actual gas mixtures produced over a wide range of

equivalence ratio were compared with the values for air, and were found in all cases to be within 5%, (usually about 2%). The use of the properties of air was therefore considered justified as the calculation of mixture properties is fairly lengthy, and in any case is not much more accurate than the errors introduced by using properties of air.

$$\bar{C}_p = 0.269 \text{ cal/g } K^o$$

$$\bar{\lambda} = 154.2 \text{ cal/cm s } K^o$$

$$T_g = 1279^oK$$

Substituting the above into equations 3.4 and 3.3 gives

$$\kappa = 7.76 \times 10^{-3} \text{ cm}^2/\text{s}$$

The spray evaporation efficiency of a CSTR is given by

$$\varepsilon = \frac{\kappa\tau b}{1 + \kappa\tau b} \qquad (4.23)$$

substituting $\kappa = 7.76 \times 10^{-3} \text{ cm}^2/\text{s}$

$\tau = 72.62 \times 10^{-3} \text{ s}$

$b = 5.547 \times 10^{4} \text{ cm}^{-2}$

gives $\varepsilon = 0.969$, which is sufficiently close to the assumption of $\varepsilon = 0.970$. The gas composition calculated (by CECPSR) for the feed is shown in Table E.1. The calculated gas composition is in mole fractions. To calculate the mass flow rate of each species out of reactor A, the average molecular weight of the gases and the total mass flow rate are calculated to derive the total molar flow rate. This allows the mass flow rate of each species to be calculated from the mole fractions.

$$\text{Average molecular weight} = \sum_{\text{all species}} (\text{mole fraction} \times \text{molecular weight})$$

$$= 28.84$$

$$\text{Total (gas phase) mass flow rate} = 10.6 + 0.291$$

$$= 10.891 \text{ g/s}$$

$\therefore$ molar flow rate = 0.377 g mole/s

Mass flow rate of each species = 0.377 x species MW x species mole fraction.

The result for each species are shown in Table E.2.

The equivalence ratio in reactor A is given by

$$\phi = 14.4 \times \frac{0.291}{10.6} = 0.398$$

The cumulative efficiency, ε_{cum}, is defined as the fraction of the total fuel that has so far evaporated.

$$\varepsilon_{cum} = \frac{0.291}{2.0} = 0.145.$$

The reactor volume may be calculated from the mean residence time, molar throughput (exit conditions) and temperature assuming the perfect gas law

$$\text{Volume } (cm^3) = 22400 \times \frac{T\ (^oK)}{273} \times \left(\frac{\text{moles}}{s}\right) \times \tau$$

substituting

$$V_A = 22400 \times \frac{1279}{273} \times 0.377 \times 0.07262$$

$$= 2882\ cm^3.$$

REACTOR C is a plug flow reactor with a residence time of 0.363 ms, and it may be reasonably assumed that there is no evaporation or reaction in this reactor. The basis for this assumption was discussed in section 8.1.. The feed to reactor C therefore passes unchanged to reactor B, where it is instantaneously mixed with the products of reactor A, and with the secondary reverse air.

REACTOR B is a CSTR with mean residence time of 2.905 ms

Fuel feed: from C, 0.85 x 2 = 1.7 g/s

from A, unevaporated fuel = 0.009 g/s

total = 1.709 g/s

Air feed: from C 0.85 x 4 = 3.4 g/s

reverse secondary air = 10.0 g/s

total = 13.4 g/s

comprising 10.291 g/s N_2 at 298°K

3.109 g/s O_2 at 298°K

Some O_2 and N_2 also enters B from A, as shown in Table E.2.

Summing oxygen:	3.109 g/s at 298°K (see above)	
	1.481 g/s at 1279°K (from A)	
Total	4.590 g/s at 615°K	

Summing nitrogen:	10.291 g/s at 298°K (see above)	
	8.129 g/s at 1279°K (from A)	
Total	18.420 g/s at 731°K	

The feed rates of all other gas species entering B are those shown in Table E.2 as leaving A, at a temperature of 1279°K.

Assuming an evaporative efficiency of 0.675,

fuel evaporated = 1.709 x 0.675 = 1.154 g/s .

Using the above as data for program CECPSR, the product temperature is calculated to be 2001°K. At this temperature the values of κ and ϵ were calculated in the same way as for reactor A to be

$$\kappa = 13.1 \times 10^{-3} \text{ cm}^2/\text{s}$$

$$\epsilon = 0.678 \simeq \text{assumed } \epsilon_0$$

The product species mole fractions are given in Table E.1 and their mass flow rates as shown in Table E.2 were calculated as shown for reactor A. The mass flow rate of unevaporated spray from reactor B is 1.709-1.154 = 0.555 g/s. The volume of reactor B is calculated (as shown for reactor A) as 427 cm^3; cumulative efficiency = 0.723; equivalence ratio is 0.874.

REACTOR D is a plug flow reactor with a residence time of 4.9 ms. This was modelled as five CSTRs in series (as discussed in chapter 8), referred to as reactors D1 through D5.

Reactor D1 (τ = 0.001 s). The feed comprises of the products from B. Assuming ϵ_0 = 0.44, fuel evaporated is 0.555 x 0.44 = 0.2442 g/s.

Program CECPSR calculated the temperature as 2189°K

$\therefore$ $\kappa = 14.3 \times 10^{-3}$ cm^2/s and $\epsilon = 0.442$

$\therefore$ fuel evaporated = 0.555 x 0.442 = 0.2453 g/s .

Rerun of CECPSR gives T = 2189°K which gives ϵ = 0.442.

Products are as shown in Tables E.1 and E.2.

Unevaporated fuel = 0.3097 g/s

Cumulative efficiency = 0.845

Reactor volume = 162 cm^3

Reactors D2 through D5 are similarly solved; the product composition and flow rates are shown in Tables E.1 and E.2, and the other results in Table 8.6.

Table E.1. Species Mole Fractions in Reactor Elements of Run 5.

SPECIES \ REACTOR	A	B	D1	D2	D3	D4	D5
CO	1.054×10^{-3}	1.665×10^{-2}	$2.628xx\ 10^{-2}$	3.795×10^{-2}	4.192×10^{-2}	4.339×10^{-2}	4.439×10^{-2}
CO_2	5.459×10^{-2}	1.004×10^{-1}	1.096×10^{-1}	1.071×10^{-1}	1.053×10^{-1}	1.045×10^{-1}	1.040×10^{-1}
H	8.171×10^{-5}	1.376×10^{-3}	1.355×10^{-3}	1.069×10^{-3}	7.286×10^{-4}	6.372×10^{-4}	6.052×10^{-4}
H_2	1.224×10^{-4}	2.740×10^{-3}	4.956×10^{-3}	8.301×10^{-3}	9.510×10^{-3}	9.865×10^{-3}	1.017×10^{-2}
H_2O	5.049×10^{-2}	1.011×10^{-1}	1.164×10^{-1}	1.226×10^{-1}	1.238×10^{-1}	1.241×10^{-1}	1.241×10^{-1}
N	4.871×10^{-11}	4.098×10^{-9}	1.320×10^{-8}	1.165×10^{-8}	9.605×10^{-9}	9.167×10^{-9}	8.840×10^{-9}
NO	8.857×10^{-6}	4.572×10^{-5}	7.299×10^{-5}	8.123×10^{-5}	8.410×10^{-5}	8.612×10^{-5}	8.754×10^{-5}
NO_2	2.632×10^{-9}	2.491×10^{-9}	5.268×10^{-9}	5.336×10^{-9}	5.822×10^{-9}	6.049×10^{-9}	6.011×10^{-9}
N_2	7.699×10^{-1}	7.382×10^{-1}	7.273×10^{-1}	7.191×10^{-1}	7.167×10^{-1}	7.159×10^{-1}	7.154×10^{-1}
N_2O	3.834×10^{-6}	2.227×10^{-7}	9.617×10^{-8}	4.427×10^{-8}	2.885×10^{-8}	2.435×10^{-8}	2.195×10^{-8}
O	4.503×10^{-4}	1.953×10^{-3}	8.564×10^{-4}	2.098×10^{-4}	7.423×10^{-5}	5.242×10^{-5}	4.412×10^{-5}
OH	5.183×10^{-4}	5.154×10^{-3}	4.397×10^{-3}	2.324×10^{-3}	1.397×10^{-3}	1.170×10^{-3}	1.067×10^{-3}
O_2	1.228×10^{-1}	3.241×10^{-2}	8.820×10^{-3}	1.354×10^{-3}	4.020×10^{-4}	2.731×10^{-4}	2.221×10^{-4}

Table E.2 Species Mass Flow Rates out of Reactor Elements of Run 5 (g/s)

SPECIES \ REACTOR	A	B	D1	D2	D3	D4
CO	1.112×10^{-2}	3.967×10^{-1}	6.655×10^{-1}	9.725×10^{-1}	1.078	1.117
CO_2	9.056×10^{-1}	3.759	4.362	4.314	4.257	4.229
H	3.081×10^{-5}	1.171×10^{-3}	1.226×10^{-3}	9.780×10^{-4}	6.692×10^{-4}	5.859×10^{-4}
H_2	9.229×10^{-5}	4.662×10^{-3}	8.966×10^{-3}	1.519×10^{-2}	1.747×10^{-2}	1.814×10^{-2}
H_2O	3.427×10^{-1}	1.548	1.895	2.019	2.047	2.053
N	2.571×10^{-10}	4.881×10^{-8}	1.672×10^{-7}	1.493×10^{-7}	1.235×10^{-7}	1.180×10^{-7}
NO	1.002×10^{-4}	1.167×10^{-3}	1.980×10^{-3}	2.230×10^{-3}	2.317×10^{-3}	2.375×10^{-3}
NO_2	4.565×10^{-8}	9.747×10^{-8}	2.192×10^{-7}	2.246×10^{-7}	2.456×10^{-7}	2.558×10^{-7}
N_2	8.129	1.842×10^{1}	1.842×10^{1}	1.842×10^{1}	1.842×10^{1}	1.842×10^{1}
N_2O	6.361×10^{-5}	8.336×10^{-6}	3.826×10^{-6}	1.783×10^{-6}	1.166×10^{-6}	9.851×10^{-7}
O	2.717×10^{-3}	2.659×10^{-2}	1.240×10^{-2}	3.072×10^{-3}	1.091×10^{-3}	7.784×10^{-4}
OH	3.322×10^{-3}	7.456×10^{-2}	6.761×10^{-2}	3.615×10^{-2}	2.181×10^{-2}	1.829×10^{-2}
O_2	1.481	8.824×10^{-1}	2.553×10^{-1}	3.964×10^{-2}	1.181×10^{-2}	8.035×10^{-3}

APPENDIX F: MOMENTUM AND KINETIC ENERGY OF CHAMBER INPUT STREAMS

In this appendix the momentum and kinetic energy of each chamber input stream will be calculated. The calculations will be based on the mass flow rates and inlet velocity as determined by the conditions used for the experimental work and the chamber geometry as shown in figure 5.2.

(a) Primary (atomising) air

The primary air mass flow rate of 4 g/s was maintained constant for each experimental run by varying the pressure between 2 bar and 2.3 bar. The velocity of the air jet will be assumed to vary between 330 m/s (sonic) and 385 m/s.

The momentum is therefore between $4 \times 330 = 1320$ g m/s

and $4 \times 385 = 1540$ g m/s

The kinetic energy is between $\frac{1}{2} \times 4 \times (330)^2 = 2.18 \times 10^5$ g m^2/s^2

and $\frac{1}{2} \times 4 \times (385)^2 = 2.96 \times 10^5$ g m^2/s^2

(b) Fuel

The fuel is fed through a tube of 1.25 mm diameter at a constant rate of 2 g/s. Density of the fuel is 0.835 g/cm^3, so that its velocity is approximately 2.0 m/s.

$\therefore$ momentum $= 2 \times 2 = 4.0$ g m/s

kinetic energy $= \frac{1}{2} \times 2 \times (2)^2 = 4.0$ g m^2/s^2 .

(c) Secondary air

The secondary air is divided between the forward and the reverse chamber casing. The flow to each of these is assumed to be divided equally between 30 and 38 nozzles respectively, each 3.175 mm in diameter. The total secondary air flow varies from 20 to 28 g/s depending on the overall equivalence ratio used, while variations in the ratio of forward to reverse flow rates lead to values of each ranging from 9 to 16 g/s.

From the above, assuming the air flows through the nozzles at STP, the velocity ranges for the nozzles in each half of the chamber are as follows:-

forward:	30.0	to	54.0 m/s
reverse:	24.0	to	42.5 m/s

However, as the air is used to cool the refractory over which it passes prior to entering the nozzles, it is considerably preheated. As a rough estimate, a temperature of 473°K will be assumed, which increases the above linear velocities by 73% to:-

forward: 52.0 to 93.5 m/s

reverse: 41.5 to 73.5 m/s

These velocities lead to respective momentum and kinetic energy ranges as follows:

forward: 468 to 1496 g m/s and 1.21 to 7.0 x 10^4 g m^2/s^2

reverse: 374 to 1176 g m/s and 0.775 to 4.32 x 10^4 g m^2/s^2

For every increment of 100 K in the secondary air temperature, the momentum figures should be increased by 36.6% and those relating to kinetic energy by 87%.

Table F.1 summarises the above results and clearly shows that the momentum and kinetic energy of the atomiser is greater than the total for the secondary forward nozzles and also than the secondary reverse nozzles. As the secondary air momentum and energy per nozzle is about one thirtieth that of the totals given, it is reasonable to conclude that the primary air/fuel spray jet is the major factor determining the chamber aerodynamics.

Table F.1: Summary of Momentum and Kinetic Energy of Chamber Input Streams

Stream	Momentum (g m/s)	Kinetic Energy (g m^2/s^2)
Primary air	1320 to 1540	2.18 to 2.96, x 10^5
Fuel	4.0	4.0
Forward secondary air		
total	468 to 1496	1.21 to 7.0, x 10^4
per nozzle	15.6 to 49.9	403 to 2333
Reverse secondary air		
total	374 to 1176	0.775 to 4.32, x 10^4
per nozzle	9.84 to 30.9	204 to 1137

APPENDIX G: OPERATION OF ELECTRONIC CIRCUIT USED TO CONTROL THE DYNAMIC INJECTION AND SAMPLING VALVES

The control box (designed and constructed by R. Wood of the Electronics Section) produces an injection solenoid drive signal at a constant but selectable repetition rate and drives the sample valve after a delay, selectable between 12 and 1112 ms. The circuit diagram shown in figure 6.5 is divided into three basic sections as follows:

(a) The Basic Timing Circuits [figure 6.5(a)].

The basic repetition rate generator consists of one XR220 integrated circuit delay timer (A) connected as an astable multivibrator. The multivibrator period is determined by the resistance values R1, R2 and capacitance C1 (chosen to produce repetition rates suitably longer than the mean residence time of the combustion chamber). The repetition rate is selectable by a switch at 1 or 2 cycles per second, and a stop/run switch is provided.

Two outputs are available from the XR220 timer. One is used to provide a pulse to start the "Advance TC7" digital counter/timer (used to check the delay time between injection and sampling value drive signals), which requires a start pulse of -4 volts into a load of 470 ohms. The other output is used to initiate the delay time generator and also the injection period timer (figure 6.5(c)).

The delay time generator consists of a further XR220 timer circuit (B) connected as a monostable vibrator. The monostable period is set by the resistor chain connected to pin 1 and the timing capacitor connected to pin 3. The total resistance is varied by means of the 10 turn potentiometer (resistance 100 Kohms) and by selecting part of the fixed resistor chain by means of the decade switch. The resistors were selected to match the exact value of the 100 Kohm potentiometer, and by means of padding the capacitor on pin 3 it was possible to obtain accurate delay periods. One output of the delay time generator is used to feed the stop line of the TC7 timer/counter whilst the other is fed to the gate of a solid state switch used as a 'slave' to drive the main solid state switch (figure 6.5(b)) of the sampling valve drive circuit.

(b) Injection Valve Drive Circuit [figure 6.5(c)].

A circuit similar to the delay time generator is used to time the energisation period of the injection valve. The timer is initiated by the repetition rate generator - the output on pin 12 going low when the circuit is triggered, thus turning on the 2N 1132 and MC140 transistors and energising the injection valve solenoid. At the end of the timing period (determined by the resistor on pin 1 and the capacitor on pin 3) the output on pin 12 goes to a high level and the valve solenoid is de-energised, ending the injection.

(c) Sampling Valve Drive Circuit [figure 6.5(b)].

The sampling valve is driven by the application of a short high current pulse obtained from a bank of high current capacity electrolytic capacitors. The two 1500 microfarad capacitors shown were found to be adequate. Initially the capacitors are charged from a mains derived low voltage supply. When the 'slave' solid state switch is triggered from the delay timer [figure 6.5(a)], the solid state switch SCR2 is driven into its conducting condition thus discharging the capacitors through the sample valve solenoid.

The value of the capacitor bank and the applied voltage were determined experimentally to product sufficient energy to operate the hammer of the sampling valve and yet allow the electrical circuit to be slightly underdamped. It should be noted that because the discharge circuit contains both inductance and capacitance, the discharge characteristic will be oscillatory if electrical damping is not too high. Thus, the first current reversal will cause the SCR to become reverse biassed and to revert to its non-conducting state. The capacitor bank recharges from the rectified supply and the cycle may continue. Should the oscillatory nature of the circuit be lost, due for example to the solenoid coils shorting, then the SCR will not "turn off" and the capacitor bank will not recharge. Under these conditions the fault condition has to be rectified before continuous cyclic operation can be maintained.

APPENDIX H: EXPERIMENTAL AND DERIVED RESULTS

The results of the stimulus response experiments will be presented in this appendix in tabular form, as summarised by the output of program LAPLACE (see Appendix I). Table H.1 gives the results of the input pulse measurement while Tables H.2 to H.8 give the results of Runs 1 to 7, with the transfer functions referring to the input in Table H.1. Table H.9 gives the results of a duplicate input pulse determination.

The unit of time in the data and the output is milliseconds. The area of the normalized curves has been made 1000 units. Gross time refers to the output, while net time refers to the difference between the output and the input. The net mean residence time of the non-plug flow part of the output is used as the value of TAU.

Additional details of the program and output are given in Appendix I.

Table H.1. Experimental and Derived Results for Run 0

SUMMARY OF RESULTS

RUN NUMBER 0

EXPERIMENTAL DATA

T	17.5	20.0	22.5	25.0	27.5	30.0	32.5	35.0	37.5	40.0	45.0	50.0	60.0	75.0	100.0	125.0
C	3.6	11.5	27.0	42.2	62.5	77.7	82.4	84.4	82.4	66.3	47.5	28.0	16.0	9.6	5.7	3.4

NORMALIZED SHIFTED RESIDENCE TIME FREQUENCY CURVE

T	0	1.3	3.8	6.3	8.8	11.3	13.8	16.3	18.8	21.3	23.8	28.8	33.8	43.8	58.8	83.8	108.8
C	0	1.40	4.46	10.48	16.37	24.25	30.15	31.97	32.75	31.97	25.72	18.43	10.86	6.21	3.72	2.21	1.32

PLUG FLOW DELAY TIME (MILLISECONDS) = 16.2 GROSS, 16.2 NETT

MEAN RESIDENCE TIME (MILLISECONDS) = 38.5 GROSS, 38.5 NETT

LAPLACE TRANSFORM OF NORMALIZED CURVE

S	.015	.030	.045	.060	.075	.090	.105	.120	.135	.150	.165	.180	.195	.210	.225
TAU.S	.578	1.155	1.733	2.310	2.888	3.465	4.043	4.620	5.198	5.775	6.353	6.930	7.508	8.085	8.663
TRANSFORM	.629	.443	.328	.251	.195	.155	.125	.102	.084	.070	.058	.049	.042	.036	.031

TRANSFER FUNCTION

G	.629	.443	.328	.251	.195	.155	.125	.102	.084	.070	.058	.049	.042	.036	.031
LN(G)/S	-30.88	-27.10	-24.74	-23.06	-21.77	-20.72	-19.83	-19.06	-18.38	-17.77	-17.21	-16.70	-16.23	-15.79	-15.38

Table H.2. Experimental and Derived Results for Run 1

SUMMARY OF RESULTS

RUN NUMBER 1

EXPERIMENTAL DATA

T	23.0	25.0	27.5	30.0	32.5	35.0	37.5	40.0	42.5	45.0	47.5	50.0	55.0	60.0	75.0	100.0	125.0	150.0
C	.3	2.5	10.4	22.6	33.1	50.4	63.0	70.0	73.8	73.0	65.5	56.0	36.9	21.0	11.6	8.4	5.6	4.0

NORMALIZED SHIFTED RESIDENCE TIME FREQUENCY CURVE

T	0	.2	2.2	4.7	7.2	9.7	12.2	14.7	17.2	19.7	22.2	24.7	27.2	32.2	37.2	52.2	77.2	102.2	127.2
C	0	.12	.97	4.02	8.74	12.80	19.49	24.36	27.06	28.53	28.22	25.32	21.65	14.27	8.12	4.48	3.25	2.17	1.55

PLUG FLOW DELAY TIME (MILLISECONDS) = 22.8 GROSS, 6.6 NETT

MEAN RESIDENCE TIME (MILLISECONDS) = 53.1 GROSS, 14.6 NETT

LAPLACE TRANSFORM OF NORMALIZED CURVE

S	.015	.030	.045	.060	.075	.090	.105	.120	.135	.150	.165	.180	.195	.210	.225
TAU.S	.219	.438	.657	.876	1.095	1.314	1.533	1.752	1.971	2.190	2.410	2.629	2.848	3.067	3.286
TRANSFORM	.564	.382	.275	.206	.157	.122	.097	.077	.063	.051	.042	.035	.030	.025	.022

TRANSFER FUNCTION

G	.896	.860	.838	.820	.804	.789	.775	.762	.750	.739	.728	.718	.708	.699	.691
LN(G)/S	-7.33	-5.01	-3.92	-3.31	-2.91	-2.63	-2.43	-2.26	-2.13	-2.02	-1.93	-1.84	-1.77	-1.70	-1.64

Table H.3. Experimental and Derived Results for Run 2

SUMMARY OF RESULTS

RUN NUMBER 2

EXPERIMENTAL DATA

T	25.0	27.5	30.0	32.5	35.0	37.5	40.0	42.5	45.0	47.5	50.0	55.0	60.0	67.5	85.0	100.0	125.0
C	1.9	5.6	11.5	20.0	28.8	44.0	59.1	67.0	68.0	66.3	56.9	45.5	32.8	20.8	11.5	8.8	5.7

NORMALIZED SHIFTED RESIDENCE TIME FREQUENCY CURVE

T	0	3.0	5.5	8.0	10.5	13.0	15.5	18.0	20.5	23.0	25.5	28.0	33.0	38.0	45.5	63.0	78.0	103.0
C	0	.74	2.18	4.48	7.79	11.21	17.13	23.01	26.09	26.48	25.82	22.16	17.72	12.77	8.10	4.48	3.43	2.22

PLUG FLOW DELAY TIME (MILLISECONDS) = 22.0 GROSS, 5.9 NETT

MEAN RESIDENCE TIME (MILLISECONDS) = 52.7 GROSS, 14.2 NETT

LAPLACE TRANSFORM OF NORMALIZED CURVE

S	.015	.030	.045	.060	.075	.090	.105	.120	.135	.150	.165	.180	.195	.210	.225
TAU.S	.214	.427	.641	.854	1.068	1.281	1.495	1.708	1.922	2.135	2.349	2.563	2.776	2.990	3.203
TRANSFORM	.540	.343	.233	.165	.120	.089	.067	.052	.040	.032	.026	.021	.017	.014	.012

TRANSFER FUNCTION

G	.858	.774	.710	.658	.613	.575	.541	.511	.484	.460	.439	.419	.402	.387	.372
LN(G)/S	-10.21	-8.55	-7.61	-6.98	-6.52	-6.16	-5.86	-5.60	-5.38	-5.18	-4.99	-4.83	-4.67	-4.53	-4.39

Table H.4. Experimental and Derived Results for Run 3

SUMMARY OF RESULTS

RUN NUMBER 3

EXPERIMENTAL DATA

T	23.0	25.0	30.0	35.0	40.0	45.0	50.0	55.0	60.0	75.0	100.0	125.0
C	1.0	2.4	13.1	39.4	50.7	57.5	49.8	20.0	14.7	10.0	6.1	4.5

NORMALIZED SHIFTED RESIDENCE TIME FREQUENCY CURVE

T	0	.7	2.7	7.7	12.7	17.7	22.7	27.7	32.7	37.7	52.7	77.7	102.7
C	0	.51	1.22	6.66	20.02	25.76	29.21	25.30	10.16	7.47	5.08	3.10	2.29

PLUG FLOW DELAY TIME (MILLISECONDS) = 22.3 GROSS, 6.1 NETT

MEAN RESIDENCE TIME (MILLISECONDS) = 52.0 GROSS, 13.5 NETT

LAPLACE TRANSFORM OF NORMALIZED CURVE

S	.015	.030	.045	.060	.075	.090	.105	.120	.135	.150	.165	.180	.195	.210	.225
TAU.S	.203	.406	.609	.811	1.014	1.217	1.420	1.623	1.826	2.029	2.232	2.434	2.637	2.840	3.043
TRANSFORM	.561	.375	.267	.197	.149	.115	.090	.071	.057	.046	.038	.031	.026	.022	.019

TRANSFER FUNCTION

G	.892	.845	.813	.786	.762	.740	.719	.699	.681	.664	.648	.633	.620	.607	.595
LN(G)/S	-7.64	-5.60	-4.60	-4.01	-3.62	-3.35	-3.14	-2.98	-2.84	-2.73	-2.63	-2.54	-2.45	-2.38	-2.31

Table H.5. Experimental and Derived Results for Run 4

SUMMARY OF RESULTS

RUN NUMBER 4

EXPERIMENTAL DATA

T	26.0	27.5	30.0	35.0	40.0	42.5	45.0	47.5	50.0	55.0	60.0	67.5	75.0	100.0	125.0
C	.5	1.3	4.6	12.5	30.3	36.0	40.5	45.0	47.5	43.2	31.7	15.7	10.8	7.0	4.6

NORMALIZED SHIFTED RESIDENCE TIME FREQUENCY CURVE

T	0	.6	2.1	4.6	9.6	14.6	17.1	19.6	22.1	24.6	29.6	34.6	42.1	49.6	74.6	99.6
C	0	.27	.69	2.45	6.66	16.14	19.17	21.57	23.97	25.30	23.01	16.88	8.36	5.75	3.73	2.45

PLUG FLOW DELAY TIME (MILLISECONDS) = 25.4 GROSS, 9.2 NETT

MEAN RESIDENCE TIME (MILLISECONDS) = 54.2 GROSS, 15.7 NETT

LAPLACE TRANSFORM OF NORMALIZED CURVE

S	.015	.030	.045	.060	.075	.090	.105	.120	.135	.150	.165	.180	.195	.210	.225
TAU.S	.235	.471	.706	.942	1.177	1.413	1.648	1.884	2.119	2.355	2.590	2.826	3.061	3.297	3.532
TRANSFORM	.535	.341	.233	.166	.122	.091	.070	.054	.043	.034	.028	.023	.019	.016	.013

TRANSFER FUNCTION

G	.851	.769	.710	.662	.622	.588	.559	.533	.511	.492	.476	.461	.449	.436	.429
LN(G)/S	-10.76	-8.74	-7.61	-6.87	-6.33	-5.90	-5.54	-5.24	-4.97	-4.72	-4.50	-4.30	-4.11	-3.93	-3.76

Table H.6. Experimental and Derived Results for Run 5

SUMMARY OF RESULTS

RUN NUMBER 5

EXPERIMENTAL DATA

T	25.0	27.5	30.0	32.5	35.0	37.5	40.0	45.0	50.0	55.0	60.0	75.0	100.0	125.0
C	6.3	14.2	25.9	41.0	61.0	83.5	109.0	102.2	70.0	42.1	31.5	17.0	11.3	7.6

NORMALIZED SHIFTED RESIDENCE TIME FREQUENCY CURVE

T	0	3.9	6.4	8.9	11.4	13.9	16.4	18.9	23.9	28.9	33.9	38.9	53.9	78.9	103.9
C	0	1.78	4.00	7.30	11.56	17.20	23.54	30.73	28.82	19.74	11.87	8.88	4.79	3.19	2.14

PLUG FLOW DELAY TIME (MILLISECONDS) = 21.1 GROSS, 4.9 NETT

MEAN RESIDENCE TIME (MILLISECONDS) = 52.6 GROSS, 14.1 NETT

LAPLACE TRANSFORM OF NORMALIZED CURVE

S	.015	.030	.045	.060	.075	.090	.105	.120	.135	.150	.165	.180	.195	.210	.225
TAU.S	.212	.424	.636	.848	1.060	1.272	1.484	1.696	1.908	2.120	2.332	2.544	2.756	2.968	3.179
TRANSFORM	.553	.363	.254	.184	.137	.104	.080	.062	.049	.040	.032	.026	.022	.018	.015

TRANSFER FUNCTION

G	.878	.818	.773	.735	.701	.670	.642	.616	.591	.569	.549	.530	.513	.498	.484
LN(G)/S	-8.65	-6.70	-5.71	-5.12	-4.73	-4.44	-4.22	-4.04	-3.89	-3.76	-3.65	-3.52	-3.42	-3.32	-3.23

Table H.7. Experimental and Derived Results for Run 6

SUMMARY OF RESULTS

RUN NUMBER 6

EXPERIMENTAL DATA

T	22.5	25.0	27.5	30.0	35.0	40.0	45.0	50.0	60.0	75.0	100.0	125.0
C	3.4	7.9	17.1	37.4	75.0	91.5	85.8	63.3	24.3	14.4	10.4	7.0

NORMALIZED SHIFTED RESIDENCE TIME FREQUENCY CURVE

T	0	1.1	3.6	6.1	8.6	13.6	18.6	23.6	28.6	38.6	53.6	78.6	103.6
C	0	1.02	2.37	5.13	11.22	22.49	27.44	25.73	18.98	7.29	4.32	3.12	2.10

PLUG FLOW DELAY TIME (MILLISECONDS) = 21.4 GROSS, 5.2 NETT

MEAN RESIDENCE TIME (MILLISECONDS) = 54.1 GROSS, 15.6 NETT

LAPLACE TRANSFORM OF NORMALIZED CURVE

S	.015	.030	.045	.060	.075	.090	.105	.120	.135	.150	.165	.180	.195	.210	.225
TAU.S	.233	.467	.700	.934	1.167	1.401	1.634	1.867	2.101	2.334	2.568	2.801	3.034	3.268	3.501
TRANSFORM	.559	.377	.272	.203	.155	.120	.095	.076	.062	.051	.042	.035	.030	.025	.022

TRANSFER FUNCTION

G	.889	.850	.827	.808	.792	.777	.763	.751	.739	.729	.719	.710	.702	.695	.688
LN(G)/S	-7.87	-5.40	-4.23	-3.55	-3.11	-2.80	-2.57	-2.39	-2.24	-2.11	-2.00	-1.90	-1.81	-1.74	-1.66

Table H.8. Experimental and Derived Results for Run 7

SUMMARY OF RESULTS

RUN NUMBER 7

EXPERIMENTAL DATA

T	22.5	25.0	27.5	30.0	35.0	40.0	45.0	50.0	55.0	60.0	75.0	100.0	115.0
C	1.3	5.3	13.0	27.8	70.0	112.0	115.0	101.7	66.1	47.5	23.2	14.4	11.0

NORMALIZED SHIFTED RESIDENCE TIME FREQUENCY CURVE

T	0	1.5	4.0	6.5	9.0	14.0	19.0	24.0	29.0	34.0	39.0	54.0	79.0	94.0
C	0	.30	1.23	3.02	6.46	16.27	26.03	26.73	23.64	15.36	11.04	5.39	3.35	2.56

PLUG FLOW DELAY TIME (MILLISECONDS) = 21.0 GROSS, 4.9 NETT

MEAN RESIDENCE TIME (MILLISECONDS) = 49.9 GROSS, 11.4 NETT

LAPLACE TRANSFORM OF NORMALIZED CURVE

S	.015	.030	.045	.060	.075	.090	.105	.120	.135	.150	.165	.180	.195	.210	.225
TAU.S	.170	.341	.511	.681	.851	1.022	1.192	1.362	1.532	1.703	1.873	2.043	2.213	2.384	2.554
TRANSFORM	.555	.358	.246	.176	.129	.096	.073	.057	.044	.035	.028	.023	.019	.016	.013

TRANSFER FUNCTION

G	.882	.808	.750	.702	.660	.623	.589	.559	.532	.507	.485	.465	.446	.429	.414
LN(G)/S	-8.38	-7.11	-6.38	-5.90	-5.54	-5.27	-5.04	-4.84	-4.67	-4.52	-4.38	-4.26	-4.14	-4.03	-3.92

Table H.9. Experimental and Derived Results for Run -3

SUMMARY OF RESULTS

RUN NUMBER -3

EXPERIMENTAL DATA

T	17.5	20.0	22.5	25.0	27.5	30.0	32.5	35.0	37.5	40.0	45.0	50.0	60.0	75.0	100.0	125.0
C	3.4	11.0	25.5	39.8	59.6	74.3	78.6	80.2	78.4	63.0	45.1	26.7	15.4	9.3	5.5	3.4

NORMALIZED SHIFTED RESIDENCE TIME FREQUENCY CURVE

T	0	1.5	4.0	6.5	9.0	11.5	14.0	16.5	19.0	21.5	24.0	29.0	34.0	44.0	59.0	84.0	109.0
C	0	1.37	4.45	10.31	16.09	24.17	30.03	31.77	32.42	31.69	25.47	18.23	10.79	6.23	3.76	2.22	1.37

PLUG FLOW DELAY TIME (MILLISECONDS) = 16.0 GROSS, 16.0 NETT

MEAN RESIDENCE TIME (MILLISECONDS) = 39.4 GROSS, 39.4 NETT

LAPLACE TRANSFORM OF NORMALIZED CURVE

S	.015	.030	.045	.060	.075	.090	.105	.120	.135	.150	.165	.180	.195	.210	.225
TAU.S	.592	1.183	1.775	2.366	2.958	3.550	4.141	4.733	5.324	5.916	6.508	7.099	7.691	8.282	8.874
TRANSFORM	.624	.438	.324	.246	.192	.152	.122	.099	.081	.067	.056	.048	.041	.035	.030

TRANSFER FUNCTION

G	.624	.438	.324	.246	.192	.152	.122	.099	.081	.067	.056	.048	.041	.035	.030
LN(G)/S	-31.41	-27.50	-25.07	-23.35	-22.03	-20.97	-20.07	-19.29	-18.60	-17.98	-17.42	-16.91	-16.43	-15.98	-15.57

APPENDIX I: COMPUTER PROGRAM TO CALCULATE LAPLACE TRANSFORMS AND TRANSFER FUNCTIONS FROM EXPERIMENTAL PULSE TEST INPUT/OUTPUT DATA

General Approach

Program LAPLACE accepts pulse test data in the form of discrete concentration-time co-ordinates with arbitrary spacing. It is assumed that both the input and output signals can be accurately fitted by fitting a cubic to four consecutive points and then using this cubic to characterize the curve in the region between the two inner points. Also it is assumed that the last three experimental points can be used to characterize the exponential decay of the tail region (the region past the last experimental point).

The cubic and exponential equations derived above are used to analytically calculate the area, first moment and Laplace transform of each region of the curve in turn, and these values are summed progressively until the complete curve (including the tail) are covered.

Multiple sets of data may be handled; the program assumes that the first set is the input and each subsequent set is an output relating to that input. The Laplace transform is calculated for fifteen values of the Laplace transform parameter, which are multiples of the first value read in as data.

A print-out of the program listing is given at the end of this appendix. The following is a description of the operations performed by the program.

Sequence of Operations

1. The first value of the Laplace parameter (S) is read in (as ES) and the subsequent fourteen values calculated and printed out.

2. The total number of data sets (NIZ) is read in, and the following operations are carried out for <u>each</u> run.

3. The run number (NRUN), number of experimental points (NE) and their co-ordinates (T, C; NE times) are read in and printed out. The first data set relates to the input pulse and is identified by having NRUN $\leq$ 0, so that ENRUN = NRUN - 0.1 is negative and may be used later in the program to identify the input data set from the subsequent output data sets.

4. The first three points of the data set are fitted by a parabola, the appropriate root of which is taken as the time lag (ALAG) before the actual response or signal begins to rise. If (exceptionally) the parabola has no roots, its axis is taken to be the time lag.

5. ALAG is subtracted from the time co-ordinates of each experimental point, shifting the curve, with the origin now considered as the first of NP(=NE+1) points. Figure I.1(a) illustrates steps 4 and 5.

6. Starting from the first point (i.e. the point at the origin), four points at a time are fitted by a cubic and the equation is used to describe the curve in a region as shown in figures I.1(b) and I.1(c). The cubic equation is then used in separate subprograms to calculate the area (A), first moment (WA) and Laplace transforms TR(NN) of the appropriate region, and these are each added to the respective running totals (SA, SWA, STR(NN)) for the previous regions considered.

   Each point, with the exception of the last three, is considered in turn as the first of four for the above procedure, thus covering the entire region of experimental measurement.

7. To characterize the tail of the curve (i.e. the region after the last experimental point) an exponential equation of the form c = exp(A + Bt) is fitted to the last three experimental points (see figure I.1(d)). This equation is used in separate subprograms to calculate the area (AL), first moment (WLA) and Laplace transforms TRL(NN) of the tail region and each of these values is returned to the main program where it is added to the respective totals for the experimental region, thus completing the summations for the entire curve. The following quantities have so far been calculated:

   (i) The time lag (ALAG) $\int_0^\infty C(T')dT'$

   (ii) The area, SA = T' = T - ALAG

   (iii) The first moment SWA = $\int_0^\infty T'C(T')dT'$

   (iv) The Laplace transform (for 15 different values of S)

   $$STR(NN) = \int_0^\infty C(T')\exp\{-T'.S(NN)\}dT'$$

First three experimental points are fitted by a quadratic, the solution of which becomes the initial point of the shifted curve.

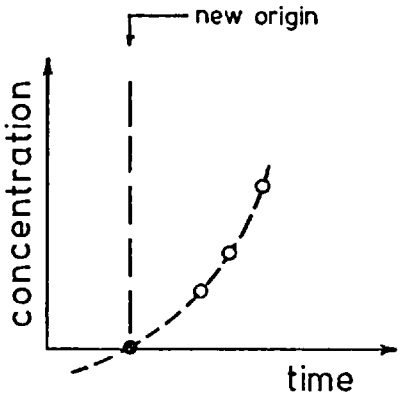

(a)

Cubic fit to four points is used to characterise region between two inner points.

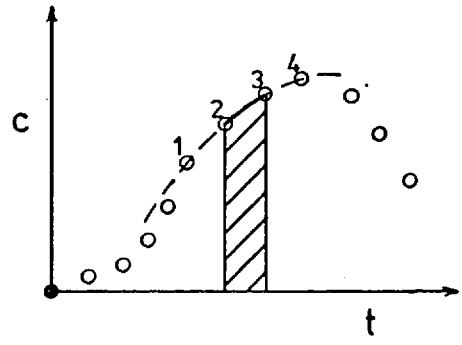

(b)

If first of four points is origin, cubic characterises region between first and third point.
Cubic fit to last four points is used to characterise region between last three points.

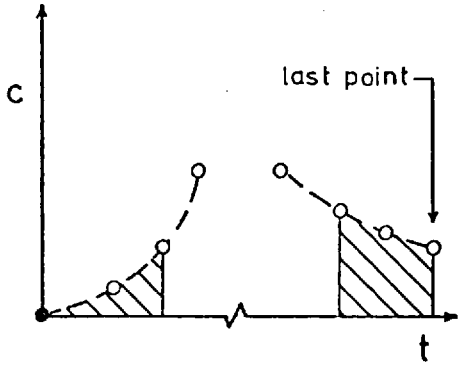

(c)

Exponential fit to last three points is used to characterise region past last point.

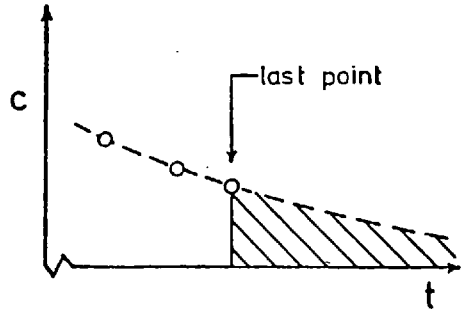

(d)

FIGURE I.1 Analysis of experimental data by program LAPLACE.

8. The mean time of the displaced curve is calculated from

$$TAUO = SWA/SA$$

9. The experimental curve is expressed in normalised form by adjusting the co-ordinates of each point as follows

$$TN = T'$$

$$CN = 1000 \cdot C/SA$$

so that the curve represented by (TN,CN) has unit area. The time read in is in milliseconds so that SA/1000 is the area in units of (mole-sec/m^3). The factor used is not important as long as both the input and output are treated similarly.

10. The Laplace transforms are adjusted to give the transform of a pulse of unit area

$$FTR(NN) = STR(NN)/SA$$

11. The information calculated above is then processed according to whether it relates to an input or output data set (as determined from the value of ENRUN).

ENRUN≤0 (INPUT)	ENRUN>0 (OUTPUT)
BLAG = ALAG	CLAG = ALAG-BLAG
CLAG = ALAG	TAU = TAUO-TAUI
TAUI = TAUO	
TAU = TAUO	

and for each value of S

FTRO(NN) = FTR(NN)	H(NN) = FTR(NN)/FTRO(NN)
H(NN) = FTR(NN)	$G(NN) = \frac{1}{S} \cdot \ln\{H(NN)\}$
$G(NN) = \frac{1}{S} \cdot \ln\{H/NN\}$	

BLAG, TAUI and FTRO are the time lag, mean residence time and Laplace transform of the input each of which is subtracted from or divided into (for the last) the corresponding quantity relating to the output to obtain the net time lag and mean residence time and the transfer function of the system being tested.

The value of G(s) as s approaches zero is equal to minus the mean residence time and can be used as a check of the value obtained from the first moment and area calculations.

The last two subprograms POLYA and POLYB (used to fit polynomials) are taken directly from the applications library of the Chemical Engineering Department at Imperial College and are included here for completeness. A write-up of these routines is available from the Department.

Examples of outputs from program LAPLACE are shown in Appendix H.

```
      PROGRAM LAPLACE(INPUT,OUTPUT,TAPE5=INPUT,TAPE6=OUTPUT)              MAIN  10
      DIMENSION X(4),Y(4),COR(4,2),TAB(4,2),G(4),P(4),R(2),Q(4),TR(15),  MAIN  20
     1TRL(15),STR(15),FTR(15),TAUS(15),CN(20),TN(20),ET(20),EC(20),H(15)MAIN  30
     2,GS(15),FTRO(15),NUM(10),NRUN(10)                                  MAIN  40
      COMMON/BL1/T(20),C(20)                                             MAIN  50
      COMMON/BL3/S(15)                                                   MAIN  60
C                                                                        MAIN  70
C         GENERATE VALUES OF LAPLACE PARAMETER S                         MAIN  80
C                                                                        MAIN  90
      READ (5,444) ES                                                    MAIN 100
  444 FORMAT(F10.4)                                                      MAIN 110
      DO 50 LL=1,15                                                      MAIN 120
        S(LL) = ES*FLOAT(LL)                                             MAIN 130
   50 CONTINUE                                                           MAIN 140
      WRITE(6,51) (S(I),I=1,15)                                          MAIN 150
   51 FORMAT(//,2X,*VALUES OF S USED*,/,15( X,F7.4),/)                   MAIN 160
C                                                                        MAIN 170
C     NIZ IS NUMBER OF RUNS TO BE CALCULATED                             MAIN 180
C                                                                        MAIN 190
       READ (5,555) NIZ                                                  MAIN 200
  555  FORMAT(I2)                                                        MAIN 210
      INDA = 0                                                           MAIN 220
      INDB = 0                                                           MAIN 230
      DO 999 IZ=1,NIZ                                                    MAIN 240
C                                                                        MAIN 250
C     NRUN IS THE RUN NUMBER                                             MAIN 260
C                                                                        MAIN 270
      READ(5,99) NRUN(IZ)                                                MAIN 280
      ENRUN = FLOAT(NRUN(IZ)) - 0.1                                      MAIN 290
   99 FORMAT(I2)                                                         MAIN 300
      WRITE(6,199) NRUN(IZ)                                              MAIN 310
  199 FORMAT(1H1,2/,20X,*RUN NUMBER *,I2)                                MAIN 320
C                                                                        MAIN 330
C         READ IN NUMBER OF POINTS AND THEIR VALUES                      MAIN 340
C     NE IS THE NUMBER OF EXPERIMENTAL POINTS                            MAIN 350
```

```
C                                                                       MAIN 360
      READ(5,100) NE                                                    MAIN 370
  100 FORMAT(I2)                                                        MAIN 380
      NP = NE + 1                                                       MAIN 390
C                                                                       MAIN 400
C          WRITE OUT INPUT DATA                                         MAIN 410
C                                                                       MAIN 420
      WRITE(6,151) NE                                                   MAIN 430
  151 FORMAT(///,5X,*NUMBER OF EXPERIMENTAL POINTS = *,I3,/,7X,*T*,9X,*CMAIN 440
     1*)                                                                MAIN 450
      DO 1 I=2,NP                                                       MAIN 460
       READ(5,101) T(I),C(I)                                            MAIN 470
  101 FORMAT(F5.1,5X,F5.1)                                              MAIN 480
      ET(I) = T(I)                                                      MAIN 490
      EC(I) = C(I)                                                      MAIN 500
      WRITE(6,154) T(I),C(I)                                            MAIN 510
  154 FORMAT(5X,F5.1,5X,F5.1)                                           MAIN 520
    1 CONTINUE                                                          MAIN 530
C                                                                       MAIN 540
C          FIT QUADRATIC TO FIRST THREE POINTS                          MAIN 550
C                                                                       MAIN 560
      DO 2 J=1,3                                                        MAIN 570
        X(J) = T(J+1)                                                   MAIN 580
        Y(J) = C(J+1)                                                   MAIN 590
    2 CONTINUE                                                          MAIN 600
      M = 2                                                             MAIN 610
      N = 3                                                             MAIN 620
      J1 = 3                                                            MAIN 630
      CALL POLYA(X,Y,N,XSC,XSH,M,J1,TAB,COR,G)                          MAIN 640
      SHIF = 0.0                                                        MAIN 650
      SCALE = 1.0                                                       MAIN 660
      CALL POLYB(P,SHIF ,SCALE,N,XSC,XSH,M,J1,TAB,COR,G)                MAIN 670
      WRITE(6,103) (P(K),K=1,3)                                         MAIN 680
  103 FORMAT(5X,*COEFFICIENTS OF QUADRATIC THROUGH FIRST THREE POINTS*,/MAIN 690
     1,5X,*C=*,E9.3,*+*,E9.3,*(T) + *,E9.3, 4HT**2)                     MAIN 700
```

```
C                                                                       MAIN 710
C          FIND ROOTS OF QUADRATIC, OR AXIS IF NO INTERCEPT             MAIN 720
C                                                                       MAIN 730
      R21 =      P(2)*P(2) - 4.0*P(3)*P(1)                            MAIN 740
      IF (R21) 70,71,71                                               MAIN 750
   71 R11 = SQRT(R21)                                                 MAIN 760
      R12 =  2.0*P(3)                                                 MAIN 770
      R1  = (-P(2) + R11)/R12                                         MAIN 780
      R2  = -(P(2) + R11)/R12                                         MAIN 790
      WRITE(6,104) R1,R2                                              MAIN 800
  104 FORMAT(/,5X,*ROOTS OF QUADRATIC ARE*,2(3X,E9.3))                MAIN 810
C                                                                       MAIN 820
C          FIND APPRORIATE ROOT                                         MAIN 830
C                                                                       MAIN 840
      IF (R1) 3,4,4                                                   MAIN 850
    4 IF (R2) 6,7,7                                                   MAIN 860
    7 IF (R1 - R2) 9,8,8                                              MAIN 870
    8 IF (R1 - T(2))6,3,3                                             MAIN 880
    9 IF (R2 - T(2))3,6,6                                             MAIN 890
    3 T(1) = R2                                                       MAIN 900
      GO TO 5                                                         MAIN 910
    6 T(1) = R1                                                       MAIN 920
    5 ALAG = T(1)                                                     MAIN 930
      C(1) = P(1) + P(2)*T(1) + P(3)*T(1)*T(1)                        MAIN 940
      GO TO 72                                                        MAIN 950
   70 T(1) = -P(2)/(2.0*P(3))                                         MAIN 960
      ALAG = T(1)                                                     MAIN 970
      C(1) = 0.0                                                      MAIN 980
   72 WRITE(6,105) T(1),C(1)                                          MAIN 990
  105 FORMAT(/,5X,*DELAY TIME =*,F6.2,*MILLISECS*,5X,*C(1)=*,E12.6)   MAIN1000
      EC(1) = 0.0                                                     MAIN1010
      ET(1) = ALAG                                                    MAIN1020
C                                                                       MAIN1030
C          SHIFT CURVE TO BEGIN AT ORIGIN                               MAIN1040
C                                                                       MAIN1050
```

```
      DO 10 M=1,NP                                                      MAIN1060
        T(M) = T(M) - ALAG                                              MAIN1070
   10 CONTINUE                                                          MAIN1080
      WRITE(6,106) (T(I),I=1,NP)                                        MAIN1090
  106 FORMAT(/,5X,*SHIFTED TIMES ARE*,/,20(X,F5.1))                     MAIN1100
      WRITE(6,2003) NP,(I,T(I),C(I),I=1,NP)                             MAIN1110
 2003 FORMAT(/,5X,I3,* POINTS USED FOR TRANSFER FUNCTION CALCULATION AREMAIN1120
     1*,/,25(2X,I2,2X,F5.1,2X,F5.1,/))                                  MAIN1130
C                                                                       MAIN1140
C        INITIATE REGISTERS FOR AREA, FIRST MOMENT AND LAPLACE TRANSFORMMAIN1150
C                                                                       MAIN1160
      SA  =  0.0                                                        MAIN1170
      SWA =  0.0                                                        MAIN1180
      DO 63 I=1,15                                                      MAIN1190
   63 STR(I) = 0.0                                                      MAIN1200
C                                                                       MAIN1210
C         SET UP REGIONS FOR FITTING, INTEGRATION, FIRST MOMENTS AND    MAIN1220
C         LAPLACE TRANSFORMATION                                        MAIN1230
C                                                                       MAIN1240
C     NE = NO. OF EXPERIMENTAL POINTS                                   MAIN1250
C     NP = NO. OF POINTS USED = NE + 1  EXTRA POINT IS ORIGIN.          MAIN1260
C     NF = NO. OF LAST EXPTL PT USED AS FIRST OF FOUR PTS FOR CUBIC FIT MAIN1270
C     N1 = LOWER BOUND OF REGION                                        MAIN1280
C     N2 = UPPER BOUND OF REGION                                        MAIN1290
C                                                                       MAIN1300
      NF  =   NP-3                                                      MAIN1310
      DO 1000 J=1,NF                                                    MAIN1320
          NI  = J                                                       MAIN1330
          AJ  = FLOAT(J)                                                MAIN1340
          IF (AJ - 1.1)12,12,13                                         MAIN1350
   12     N1  =1                                                        MAIN1360
          GO TO 14                                                      MAIN1370
   13     N1  = NI + 1                                                  MAIN1380
   14 ANF = FLOAT(NF)                                                   MAIN1390
      IF (ANF - AJ  - 0.1)15,15,16                                      MAIN1400
```

```
   16 N2 = NI + 2                                                    MAIN1410
      GO TO 18                                                       MAIN1420
   15 N2 = NI + 3                                                    MAIN1430
   18 CONTINUE                                                       MAIN1440
C                                                                    MAIN1450
C          CUBIC FITTING TO FOUR POINTS AT A TIME                    MAIN1460
C                                                                    MAIN1470
           CALL CUBFIT(NI,Q)                                         MAIN1480
C                                                                    MAIN1490
C          INTEGRATION, FIRST MOMENT AND LAPLACE TRANSFORM FOR REGION    MAIN1500
C          BETWEEN TWO INNER POINTS - EXCEPT FIRST REGION IN WHICH CASE  MAIN1510
C          INTERVAL CONSIDERED IS BETWEEN FIRST AND THIRD POINT, AND LASTMAIN1520
C          REGION , WHERE INTERVAL IS B/W SECOND AND FOURTH POINT    MAIN1530
C                                                                    MAIN1540
       CALL AREA(N2,N1,Q,A)                                          MAIN1550
           SA  = SA + A                                              MAIN1560
       CALL FSTM(N2,N1,Q,WA)                                         MAIN1570
       SWA  = SWA + WA                                               MAIN1580
       CALL TRANS(N2,N1,Q,TR)                                        MAIN1590
       DO 30 NN=1,15                                                 MAIN1600
           STR(NN) = STR(NN) + TR(NN)                                MAIN1610
   30 CONTINUE                                                       MAIN1620
 1000 CONTINUE                                                       MAIN1630
C                                                                    MAIN1640
C          EXPONENTIAL FITTING TO LAST THREE POINTS AND CALCULATION OF   MAIN1650
C          CONTRIBUTUION OF TAIL                                     MAIN1660
C                                                                    MAIN1670
       N3 = NP - 2                                                   MAIN1680
       CALL LOGFIT(R,N3)                                             MAIN1690
       CALL ALA(NP,R,AL)                                             MAIN1700
       SA = SA + AL                                                  MAIN1710
       CALL FSTML(NP,R,WLA)                                          MAIN1720
       SWA  = SWA + WLA                                              MAIN1730
       TAUO = SWA/SA                                                 MAIN1740
       TSA =  TAUO/SA                                                MAIN1750
```

```
      WRITE(6,107) SA                                                    MAIN1760
  107 FORMAT(////, 9X,*TOTAL AREA = *,E9.3,/)                            MAIN1770
      WRITE(6,120) SWA,TAUO                                              MAIN1780
  120 FORMAT(9X,*FIRST MOMENT OF CURVE IS *,E10.3,/,9X,*MEAN RESIDENCE TMAIN1790
     1IME = *,E10.3,/)                                                   MAIN1800
      DO 41 K=1,NP                                                       MAIN1810
      TN(K) = T(K)                                                       MAIN1820
   41 CN(K) = 1000.0*C(K)/SA                                             MAIN1830
C                                                                        MAIN1840
C          MANIPULATION OF TIME DOMAIN DATA                              MAIN1850
C                                                                        MAIN1860
C          IS DATA SET INPUT OR OUTPUT                                   MAIN1870
      IF(ENRUN)180,180,181                                               MAIN1880
  180 BLAG = ALAG                                                        MAIN1890
      CLAG = ALAG                                                        MAIN1900
      TAUI = TAUO                                                        MAIN1910
      TAU  = TAUO                                                        MAIN1920
      GO TO 182                                                          MAIN1930
  181 CLAG = ALAG - BLAG                                                 MAIN1940
      TAU  = TAUO - TAUI                                                 MAIN1950
  182 CONTINUE                                                           MAIN1960
      CALL TRANL(NP,R,TRL)                                               MAIN1970
      DO 31 NJ = 1,15                                                    MAIN1980
          STR(NJ) = STR(NJ) + TRL(NJ)                                    MAIN1990
C         DIVIDE BY PULSE AREA TO OBTAIN TRANSFORM OF UNIT PULSE         MAIN2000
          FTR(NJ) = STR(NJ)/SA                                           MAIN2010
C                                                                        MAIN2020
C          MANIPULATION OF LAPLACE DOMAIN DATA                           MAIN2030
C                                                                        MAIN2040
C          IS DATA SET INPUT OR OUTPUT                                   MAIN2050
      IF(ENRUN) 160,160,161                                              MAIN2060
C                                                                        MAIN2070
C     SET UP INPUT TRANSFER FUNCTION                                     MAIN2080
C                                                                        MAIN2090
  160 FTRO(NJ) = FTR(NJ)                                                 MAIN2100
```

```
      H(NJ) = FTRO(NJ)                                                  MAIN2110
      GO TO 32                                                          MAIN2120
C                                                                       MAIN2130
C     OVERALL TRANSFER FUNCTION = OUTPUT T.F./INPUT T.F.                MAIN2140
C                                                                       MAIN2150
  161 H(NJ) = FTR(NJ)/FTRO(NJ)                                          MAIN2160
   32 GS(NJ)= ALOG(H(NJ))/S(NJ)                                         MAIN2170
      TAUS(NJ) = TAU*S(NJ)                                              MAIN2180
   31 CONTINUE                                                          MAIN2190
C                                                                       MAIN2200
C        PRINT OUT SUMMARY OF RESULTS                                   MAIN2210
C                                                                       MAIN2220
      WRITE(6,140)                                                      MAIN2230
  140 FORMAT(1H1,2/,X,129(1H*),/,X,1H*,48X,*SUMMARY OF RESULTS*,61X,1H*,MAIN2240
     1/,X,1H*,127X,1H*)                                                 MAIN2250
      WRITE(6,139) NRUN(IZ)                                             MAIN2260
  139 FORMAT(X,8(1H*),* RUN NUMBER *,I2,106X,1H*,/,X,1H*,127X,1H*)      MAIN2270
      WRITE(6,141)                                                      MAIN2280
  141 FORMAT(X26H******** EXPERIMENTAL DATA,102X,1H*,/,X,1H*,127X,1H*)  MAIN2290
      WRITE(6,142) (ET(I),I=2,NP)                                       MAIN2300
  142 FORMAT(X,1H*,2X,*T*,4X,20(F5.1,X))                                MAIN2310
      WRITE(6,143) (EC(I),I=2,NP)                                       MAIN2320
  143 FORMAT(X,1H*,127X,1H*,/,X,1H*,2X,*C*,4X,20(F5.1,X))               MAIN2330
      WRITE(6,144)                                                      MAIN2340
  144 FORMAT(X,1H*,127X,1H*,/,X,58H******** NORMALIZED SHIFTED RESIDENCEMAIN2350
     2 TIME FREQUENCY CURVE,70X,1H*,/,X,1H*,127X,1H*)                   MAIN2360
      WRITE(6,145) (TN(K),K=1,NP)                                       MAIN2370
  145 FORMAT(X,1H*,2X,*T*,20(F5.2,X))                                   MAIN2380
      WRITE(6,146) (CN(K),K=1,NP)                                       MAIN2390
  146 FORMAT(X,1H*,127X,1H*,/,X,1H*,2X,*C*,20(F5.3,X))                  MAIN2400
      WRITE(6,147) ALAG,CLAG,TAUO,TAU                                   MAIN2410
  147 FORMAT(X,1H*,127X,1H*,/,X,47H******** PLUG FLOW DELAY TIME (MILLISMAIN2420
     1ECONDS) = ,F4.1,* GROSS, *,F4.1,* NETT*,60X,1H*,/,X,1H*,127X,1H*,/MAIN2430
     2,X,47H******** MEAN RESIDENCE TIME (MILLISECONDS)  = ,F4.1,* GROSSMAIN2440
     3, *,F4.1,* NETT*,60X,1H*,/,X,1H*,127X,1H*)                        MAIN2450
```

```
      WRITE(6,148) (S(K),K=1,15),(TAUS(K),K=1,15),(FTR(K),K=1,15)        MAIN2460
  148 FORMAT(X,47H******** LAPLACE TRANSFORM OF NORMALIZED CURVE ,81X,1HMAIN2470
     1*,/,X,1H*,127X,1H*,/,X,11H*     S    ,15(2X,F5.3),12X,1H*,/,X,1H*,MAIN2480
     2127X,1H*,/,X,11H* TAU.S    ,15(2X,F5.3),12X,1H*,/,X,1H*,127X,1H*,/MAIN2490
     3,X,11H* TRANSFORM,15(2X,F5.3),12X,1H*,/,X,1H*,127X,1H*)            MAIN2500
      WRITE(6,138) (H(IG),IG=1,15),(GS(JG),JG=1,15)                      MAIN2510
  138 FORMAT(X,26H******** TRANSFER FUNCTION,102X,1H*,/,X,1H*,127X,1H*,/MAIN2520
     1,X,    11H*     G    ,15(2X,F5.3),12X,1H*,/,X,1H*,127X,1H*,/,X,11HMAIN2530
     2*  LN(G)/S ,15( X,F6.2),12X,1H*,/,X,1H*,127X,1H*)                  MAIN2540
      WRITE(6,164)                                                       MAIN2550
  164 FORMAT(X,1H*,127X,1H*,/,X,129(1H*))                                MAIN2560
  999 CONTINUE                                                           MAIN2570
      STOP                                                               MAIN2580
        END                                                              MAIN2590


      SUBROUTINE CUBFIT(NI,Q)                                            CUFT  10
C         FITS A CUBIC TO FOUR POINTS                                    CUFT  20
      COMMON/BL1/T(20),C(20)                                             CUFT  30
      DIMENSION Q(4),X(4),Y(4),COR(4,2),TAB(4,2),G(4)                    CUFT  40
      M  = 3                                                             CUFT  50
      J1 = 4                                                             CUFT  60
      N  = 4                                                             CUFT  70
      DO 201 I=1,4                                                       CUFT  80
          NJ = NI + I - 1                                                CUFT  90
          X(I) = T(NJ)                                                   CUFT 100
          Y(I) = C(NJ)                                                   CUFT 110
  201 CONTINUE                                                           CUFT 120
      CALL POLYA(X,Y,N,XSC,XSH,M,J1,TAB,COR,G)                           CUFT 130
      SHIF = 0.0                                                         CUFT 140
      SCALE= 1.0                                                         CUFT 150
      CALL POLYB(Q,SHIF ,SCALE,N,XSC,XSH,M,J1,TAB,COR,G)                 CUFT 160
      RETURN                                                             CUFT 170
      END                                                                CUFT 180
```

```
      SUBROUTINE AREA(N2,N1,Q,A)                                        AREA  10
C         FINDS AREA UNDER SECTION OF A CUBIC                           AREA  20
      DIMENSION Q(4),B(2),D(2)                                          AREA  30
      COMMON/BL1/T(20),C(20)                                            AREA  40
      B(1) = T(N1)                                                      AREA  50
      B(2) = T(N2)                                                      AREA  60
      DO 401 I=1,2                                                      AREA  70
          W = Q(4)*B(I)/4.0 + Q(3)/3.0                                  AREA  80
          X = W*B(I) + Q(2)/2.0                                         AREA  90
          D(I) = (X*B(I) + Q(1))*B(I)                                   AREA 100
  401 CONTINUE                                                          AREA 110
      A  = D(2) - D(1)                                                  AREA 120
      RETURN                                                            AREA 130
        END                                                             AREA 140


      SUBROUTINE ALA(NP,R,AL)                                           ALA   10
C         FINDS AREA UNDER TAIL OF AN EXPONENTIALLY DECAYING CURVE      ALA   20
      COMMON/BL1/T(20),C(20)                                            ALA   30
      DIMENSION R(2),B(2),D(2)                                          ALA   40
      B(1) = T(NP)                                                      ALA   50
      B(2) = 1000.0                                                     ALA   60
      DO 501 I=1,2                                                      ALA   70
          D(I) = (EXP(R(1) + R(2)*B(I)))/R(2)                           ALA   80
  501 CONTINUE                                                          ALA   90
      AL = D(2) - D(1)                                                  ALA  100
      RETURN                                                            ALA  110
      END                                                               ALA  120
```

```
      SUBROUTINE FSTM(N2,N1,Q,WA)                                        FSTM  10
C         CALCULATES FIRST MOMENT OF A REGION UNDER A CUBIC EQUATION      FSTM  20
      COMMON/BL1/T(20),C(20)                                             FSTM  30
      DIMENSION Q(4),B(2),D(2)                                           FSTM  40
      B(1)  = T(N1)                                                      FSTM  50
      B(2)  = T(N2)                                                      FSTM  60
      W     = Q(4)/5.0                                                   FSTM  70
      X     = Q(3)/4.0                                                   FSTM  80
      Y     = Q(2)/3.0                                                   FSTM  90
      Z     = Q(1)/2.0                                                   FSTM 100
      DO 601 I=1,2                                                       FSTM 110
          DA  = W*B(I) + X                                               FSTM 120
          DB  = DA*B(I) + Y                                              FSTM 130
          DC  = DB*B(I) + Z                                              FSTM 140
          D(I)=DC*B(I)*B(I)                                              FSTM 150
  601 CONTINUE                                                           FSTM 160
      WA  = D(2) - D(1)                                                  FSTM 170
      RETURN                                                             FSTM 180
        END                                                              FSTM 190


      SUBROUTINE FSTML(NP,R,WLA)                                         FSTL  10
C         CALCULATES FIRST MOMENT OF EXPONENTIAL TAIL                     FSTL  20
      COMMON/BL1/T(20),C(20)                                             FSTL  30
      DIMENSION R(2),B(2),D(2)                                           FSTL  40
      B(1) = T(NP)                                                       FSTL  50
      B(2) = 1000.0                                                      FSTL  60
      DO 701 I=1,2                                                       FSTL  70
         X   = R(2)*B(I)                                                 FSTL  80
         D(I)= (X-1.0)*EXP(R(1)+X)/(R(2)*R(2))                           FSTL  90
  701 CONTINUE                                                           FSTL 100
      WLA = D(2) - D(1)                                                  FSTL 110
      RETURN                                                             FSTL 120
      END                                                                FSTL 130
```

```
      SUBROUTINE TRANS(N2,N1,Q,TR)                                      TRNS  10
C         CALCULATES LAPLACE TRANSFORM OF REGION OF CUBIC                TRNS  20
      COMMON/BL1/T(20),C(20)                                            TRNS  30
      COMMON/BL3/S(15)                                                  TRNS  40
      DIMENSION Q(4),B(2),D(2,15),TR(15)                                TRNS  50
      B(1) = T(N1)                                                      TRNS  60
      B(2) = T(N2)                                                      TRNS  70
      DO 801 I=1,15                                                     TRNS  80
        ES  = S(I)                                                      TRNS  90
          DO 802 J=1,2                                                  TRNS 100
          F  = B(J)                                                     TRNS 110
          BB = F*F                                                      TRNS 120
          BBB= BB*F                                                     TRNS 130
          ST = ES*F                                                     TRNS 140
          E  = EXP(-ST)                                                 TRNS 150
          A1 = -E/ES                                                    TRNS 160
          B1 = (-F*E  + A1)/ES                                          TRNS 170
          C1 = (-BB*E + 2.0*B1)/ES                                      TRNS 180
          D1 = (-BBB*E+3.0*C1)/ES                                       TRNS 190
          D(J,I) = A1*Q(1) + B1*Q(2) + C1*Q(3) + D1*Q(4)                TRNS 200
  802     CONTINUE                                                      TRNS 210
        TR(I)  = D(2,I) - D(1,I)                                        TRNS 220
  801 CONTINUE                                                          TRNS 230
      RETURN                                                            TRNS 240
      END                                                               TRNS 250
```

```
      SUBROUTINE TRANL(NP,R,TRL)                                        TRNL  10
C         CALCULATES LAPLACE TRANSFORM OF EXPONENTIAL TAIL               TRNL  20
      COMMON/BL1/T(20),C(20)                                            TRNL  30
      COMMON/BL3/S(15)                                                  TRNL  40
      DIMENSION R(2),B(2),D(2,15),TRL(15)                               TRNL  50
      B(1)  =  T(NP)                                                    TRNL  60
      B(2)  =  1000.0                                                   TRNL  70
      TT = T(NP)                                                        TRNL  80
      DO 901 I=1,15                                                     TRNL  90
          ES  =  S(I)                                                   TRNL 100
          TC = R(2) - ES                                                TRNL 110
          DUM = R(1) + TC*TT                                            TRNL 120
          TRL(I) = -EXP(DUM)/TC                                         TRNL 130
  901 CONTINUE                                                          TRNL 140
      RETURN                                                            TRNL 150
        END                                                             TRNL 160

      SUBROUTINE LOGFIT(R,N3)                                           LNFT  10
C         FITS AN EXPONENTIAL TO THREE POINTS                           LNFT  20
      DIMENSION R(2),X(4),Y(4),COR(4,2),TAB(4,2),G(4),E(20),F(20)       LNFT  30
      COMMON/BL1/T(20),C(20)                                            LNFT  40
      M  = 1                                                            LNFT  50
      J1 = 2                                                            LNFT  60
      N = 3                                                             LNFT  70
      DO 301 I=1,3                                                      LNFT  80
          NJ = N3 + I - 1                                               LNFT  90
          X(I) = T(NJ)                                                  LNFT 100
          Y(I) = ALOG(C(NJ))                                            LNFT 110
  301 CONTINUE                                                          LNFT 120
      CALL POLYA(X,Y,N,XSC,XSH,M,J1,TAB,COR,G)                          LNFT 130
      SHIF  = 0.0                                                       LNFT 140
      SCALE = 1.0                                                       LNFT 150
      CALL POLYB(R,SHIF ,SCALE,N,XSC,XSH,M,J1,TAB,COR,G)                LNFT 160
      RETURN                                                            LNFT 170
      END                                                               LNFT 180
```

```
      SUBROUTINE POLYA (X,Y,N,XSCALE,XSHIFT,M,J1,TAB,COR,G)              POLA  10
C         FITS A POLYNOMIAL                                              POLA  20
      DIMENSION COR(J1,2)                                                POLA  30
      DIMENSION TAB(N,2),X(N),Y(N),G(J1)                                 POLA  40
       XYZ = X(1)                                                        POLA  50
      XMIN = XYZ                                                         POLA  60
      XMAX=XYZ                                                           POLA  70
      DO 200 I = 2,N                                                     POLA  80
      IF(X(I) .LT. XMIN) XMIN = X(I)                                     POLA  90
      IF(X(I).GT.XMAX)XMAX=X(I)                                          POLA 100
      XYZ = XYZ + X(I)                                                   POLA 110
  200 CONTINUE                                                           POLA 120
      XSHIFT = XYZ / FLOAT(N)                                            POLA 130
      XSCALE=XSHIFT-XMIN                                                 POLA 140
      XMIN=XMAX-XSHIFT                                                   POLA 150
      IF(ABS(XMIN).GT.ABS(XSCALE))XSCALE=XMIN                            POLA 160
      DO 300 I = 1,N                                                     POLA 170
      X(I) = (X(I)- XSHIFT)/ XSCALE                                      POLA 180
  300 CONTINUE                                                           POLA 190
      M1 = M + 1                                                         POLA 200
      BETA = 0.                                                          POLA 210
      DO 10 I = 1,N                                                      POLA 220
      TAB(I,1) = 0.                                                      POLA 230
      TAB(I,2) = 1.                                                      POLA 240
   10 CONTINUE                                                           POLA 250
      SP1SQ = 0.                                                         POLA 260
      DO 700 I = 1,M1                                                    POLA 270
      SM1Y = 0.                                                          POLA 280
      SP2SQ = SP1SQ                                                      POLA 290
      SP1SQ = 0.                                                         POLA 300
      SP1SQX = 0.                                                        POLA 310
      DO 600 J = 1,N                                                     POLA 320
      XYZ = TAB(J,2)                                                     POLA 330
      SM1Y=XYZ*Y(J)      +SM1Y                                           POLA 340
      SP1S = XYZ * XYZ                                                   POLA 350
```

```
      SP1SQ = SP1S + SP1SQ                                              POLA 360
      SP1SQX=SP1S*X(J)      +SP1SQX                                     POLA 370
600   CONTINUE                                                          POLA 380
      GAMMA = SM1Y / SP1SQ                                              POLA 390
      G(I) = GAMMA                                                      POLA 400
      IF(I .EQ. M1) GO TO 700                                           POLA 410
      IF(I .EQ. 1) GO TO 950                                            POLA 420
      BETA = SP1SQ / SP2SQ                                              POLA 430
950   ALPHA = SP1SQX/ SP1SQ                                             POLA 440
      COR(I,1)=ALPHA                                                    POLA 450
      COR(I,2)= BETA                                                    POLA 460
      DO 500 J = 1,N                                                    POLA 470
      XYZ = (X(J) - ALPHA) * TAB(J,2) - BETA*TAB(J,1)                   POLA 480
      TAB(J,1) = TAB(J,2)                                               POLA 490
      TAB(J,2) = XYZ                                                    POLA 500
500   CONTINUE                                                          POLA 510
700   CONTINUE                                                          POLA 520
      DO 800 I = 1,N                                                    POLA 530
      X(I) = X(I) * XSCALE + XSHIFT                                     POLA 540
800   CONTINUE                                                          POLA 550
      RETURN                                                            POLA 560
      END                                                               POLA 570
```

```
      SUBROUTINE POLYB (C,SHIFT,SCALE,N,XSCALE,XSHIFT,M,J1,TAB,COR,G)   POLB  10
      DIMENSION TAB(N,2),G(J1),C(J1),COR(J1,2)                          POLB  20
      M1 = M + 1                                                        POLB  30
      XYZ = SCALE / XSCALE                                              POLB  40
      XMAX=(XSHIFT-SHIFT)/XSCALE                                        POLB  50
      DO 750 I = 1,M1                                                   POLB  60
      C(I) = 0.                                                         POLB  70
      DO 750 J = 1,2                                                    POLB  80
  750 TAB(I,J) = 0.                                                     POLB  90
      TAB(1,2) = 1.                                                     POLB 100
      C(1) = G(1)                                                       POLB 110
      I1 = 2                                                            POLB 120
      DO 751 I = 2,M1                                                   POLB 130
      IY = I1                                                           POLB 140
      I1 = 3-I1                                                         POLB 150
      ALPHA = COR(I-1,1) + XMAX                                         POLB 160
      BETA = COR(I-1,2)                                                 POLB 170
      JJ = I + 1                                                        POLB 180
      DO 752 J = 2,I                                                    POLB 190
      JJ = JJ-1                                                         POLB 200
      TAB(JJ,I1) = XYZ*TAB(JJ-1,IY)-ALPHA * TAB(JJ,IY)-BETA * TAB(JJ,I1)POLB 210
      C(JJ) = C(JJ) + G(I)*TAB(JJ,I1)                                   POLB 220
  752 CONTINUE                                                          POLB 230
      TAB(1,I1) = -ALPHA*TAB(1,IY) - BETA*TAB(1,I1)                     POLB 240
      C(1) = C(1) + G(I) * TAB(1,I1)                                    POLB 250
  751 CONTINUE                                                          POLB 260
      RETURN                                                            POLB 270
      END                                                               POLB 280
```

REFERENCES

1. Fraser, R.P.
"High intensity combustion in chemical engineering."
Trans. Inst. Chem. Engrs., 35 (1957) 219

2. Nieman, R.E., Fisher, D.G. and Seborg, D.E.
"A review of process identification and parameter estimation techniques."
Int. J. Control, 13 (1971) 209

3. Anderssen, A.S. and White, E.T.
"Parameter estimation by the transfer function method."
Chem. Engng. Sci., 25 (1970) 1015

4. Michelsen, M.L. and Østergaard, K.
"The use of residence time distribution data for estimation of parameters in the axial dispersion model."
Chem. Engng. Sci., 25 (1970) 583

5. Johnson, J.L., Fan, L.T. and Wu, Y.S.
"Comparison of moments, s-plane and frequency response methods for analyzing pulse testing data from flow systems."
Ind. Engng. Chem. Process Des. Develop., 10 (1971) 425

6. Danckwerts, P.V.
"Continuous flow systems: Distribution of Residence Times."
Chem. Engng. Sci., 2, (1953) 1

7. Levenspiel, O.
"Chemical Reaction Engineering."
John Wiley & Sons Inc., N.Y., 2nd Ed. (1972)

8. Hopkins, M.J., Sheppard, A.J., Eisenklam, P.
"The use of transfer functions in the evaluation of residence time distributions."
Chem. Engng. Sci., 24 (1969) 1131

9. Fraser, R.P.
"Liquid fuel atomisation."
Sixth Symposium (International) on Combustion
The Combustion Institute, Pittsburgh (1957). p.687.

10. Fraser, R.P. and Eisenklam, Paul.
"Liquid atomisation and the drop size of sprays."
Trans. Inst. Chem. Engrs., 34 (1956) 294

11. Mugele, R.A. and Evans, H.D.
"Droplet size distribution in sprays."
Ind. Engng. Chem., 43 (1951) 1317

12. Williams, A.
"The mechanism of combustion of droplets and sprays of liquid fuels."
Oxidation and Combust. Revs., 3 (1968) 1

13. Williams, A.
"Combustion of droplets of liquid fuels: A review."
Combust. and Flame, 21 (1973) 1

14. Hedley, A.B., Nuruzzaman, A.S.M. and Martin, G.F.
"Combustion of single droplets and simplified spray systems."
J. Inst. Fuel, 44 (1971) 38

15. Faeth, G.M. and Lazar, R.S.
"Bipropellant Droplet Burning Rates and Lifetimes in a Combustion Gas Environment."
NASA CR-72622 December 1, 1969

16. Sjogren, A.
"Soot formation by combustion of an atomized liquid fuel."
Fourteenth Symposium (International) on Combustion,
The Combustion Institute, (1973) p.919

17. Khan, I.M.
"Formation and combustion of carbon in a diesel engine."
Proc. Inst. Mech. Eng., 184 (3J), 22 (1969-70)

18. Bracco, F.V.
"Nitric oxide formation in droplet diffusion flames."
Fourteenth Symposium (International) on Combustion.
The Combustion Institute, (1973) p.831

19. Mellor, A.M.
"Simplified physical model of spray combustion in gas turbine."
Combust. Sci. & Technol., 8 (1973) 101

20. Mellor, A.M.
"Spray combustion from an air-assist nozzle."
Combust. Sci. & Technol., 9 (1974) 165

21. Williams, F.A.
"On the assumptions underlying droplet vaporization and combustion theories."
J. Chem. Phys., 33 (1960) 133

22. Wood, B.J., Rosser, W.A. and Wise, H.
"Combustion of fuel drops."
AIAA. Jnl., 1 (1963) 1076

23. Wood, B.J., Wise, H. and Inami, S.H.
"Heterogeneous combustion of multicomponent fuels."
Combust. & Flame, 4 (1960) 235

24. Eisenklam, Paul, Arunachalam, S.A. and Weston, J.A.
"Evaporation rates and drag resistance of burning drops."
Eleventh Symposium (International) on Combustion,
The Combustion Institute, Pittsburgh. (1967) p.715.

25. Wolfhard, H.G. and Parker, W.G.
"Evaporation processes in a burning kerosene spray."
J. Inst. Petrol.,35 (1949) 118

26. Hottel, H.C., Williams, G.C. and Simpson, H.C.
"Combustion of droplets of heavy liquid fuels."
Fifth Symposium (International) on Combustion.
Reinhold, N.Y. (1955) p.101

27. Spalding, D.B.
"Some Fundamentals of Combustion."
Gas Turbine Series, 2, Academic Press, N.Y. 1955

28. Shapiro, A.H. and Erickson, A.J.
"On the changing size spectrum of particle clouds undergoing evaporation, combustion or acceleration."
Trans. ASME, 79 (1957) 775

29. Williams, F.A.
"Combustion Theory."
Addison Wesley, N.Y., 1965

30. Hopkins, M.J. and Eisenklam, Paul
"On the theory of spray reactors."
Inst. Chem. Engrs. Symp. Series, 33, "CHEMECA" p.197 (1971)

31. Danckwerts, P.V.
"The effect of incomplete mixing on homogeneous reactions."
Chemical Reaction Engineering; 12th Meeting European Federation Chem. Eng., Amsterdam, 1957.

32. Zwietering, Th. N.
"The degree of mixing in continuous flow systems."
Chem. Engng. Sci., 11 (1959) 1

33. Pratt, D.T.
"Theories of mixing in continuous combustion."
Fifteenth Symposium (International) on Combustion.
The Combustion Institute, Pittsburgh (1974 p.1339

34. Heywood, J.B., Fay, J.A. and Linden, L.H.
"Jet aircraft air pollution production and dispersion."
AIAA paper No.70-115, January 1970

35. Fletcher, R.S. and Heywood, J.B.
"A model for nitric oxide emissions from aircraft gas turbine engines."
AIAA paper No.71-123, January 1971

36. Hammond, D.C. Jnr. and Mellor, A.M.
"Analytical calculations for the performance and pollutant emissions of gas turbine combustors."
AIAA paper No.71-711, June 1971

37. Gouldin, F.C.
"Controlling emissions from gas turbines - The importance of chemical kinetics and turbulent mixing."
Combust. Sci. & Technol., 7 (1973) 33

38. Corrsin, S.
"Simple theory of an idealized turbulent mixer."
A.I.Ch.E. Jnl., 3, (1957) 329

39. Swithenbank, J.
"Combustion Fundamentals."
Report No.HIC 150, University of Sheffield (1972)

40. Vranos, A.
"Turbulent mixing and NO_x formation in gas turbine combustors."
Combust. and Flame, 22, (1974) 253

41. Evangelista, J.J., Shinnar, R. and Katz, S.
"Effects of imperfect mixing on stirred combustion reactions."
Twelfth Symposium (International) on Combustion
The Combustion Institute, Pittsburgh (1969) p.901

42. Swithenbank, J.
"Flame Stabilization in High Velocity Flow."
Report No.HIC 155, University of Sheffield (1973)

43. Spielman, L.A. and Levenspiel, O.
"A Monte-Carlo treatment for reacting and coalescing dispersed phase systems."
Chem. Engng. Sci., 20 (1965) 247

44. Curl, R.
"Dispersed phase mixing - I."
A.I.Ch.E.Jnl., 9, (1963) 175

45. Sonnichsen, J.W. and Pratt, D.T.
"A Monte-Carlo model of turbulent mixing for the prediction of NO production in steady flow combustors."
Paper WSCI 72-8, Western States Section/The Combustion Institute (1972)

46. Bowman, B.R., Pratt, D.T. and Crowe, C.T.
"Effects of turbulent mixing and chemical kinetics on nitric oxide production in a jet stirred reactor."
Fourteenth Symposium (International) on Combustion.
The Combustion Institute, Pittsburgh (1973) p.819

47. Sorenson, S.C., Myers, P.S. and Uyehara, O.A.
"Ethane kinetics in spark ignition exhaust gases."
Thirteenth Symposium (International) on Combustion
The Combustion Institute, Pittsburgh (1971) p.451

48. Chinitz, W. and Baurer, T.
"An analysis of non-equilibrium hydrocarbon-air combustion."
Paper WSCI 65-19, Western States Section/The Combustion Institute (1965)

49. Mosier, S.A., Roberts, R. and Henderson, R.E.
"Development and verification of an analytical model for predicting emissions from gas-turbine engine combustors during low-power operation."
AGARD CP 125, paper 25, (1973)

50. Edelman, R.B., Fortune, O. and Weilerstein, G.
"Some observations on flows described by coupled mixing and kinetics."
'Symposium on Emissions from Continuous Combustion Systems.'
eds. W. Cornelius and W.G. Agnew. Plenum Press, N.Y., 1972. pp.55-90

51. Engleman, V.S., Edelman, R.B., Bartok, W. and Longwell, J.P.
"Experiments and theoretical studies of NO_x formation in a jet-stirred combustor."
Fourteenth Symposium (International) on Combustion
The Combustion Institute, Pittsburgh (1973) p.755

52. Hammond, D.C. Jnr. and Mellor, A.M.
"Analytical calculations for the performance and pollutant emissions of gas turbine combustors."
Combust. Sci. & Technol., 4 (1971) 101

53. Kretschmer, D. and Odgers, J.
"Modelling in gas turbine combustors. - A convenient reaction rate equation."
Trans. ASME, J. Engng. Power, 94A (1972) 173

54. Swithenbank, J., Poll, I., Vincent, M.W. and Wright, D.D.
"Combustion Design Fundamentals."
Fourteenth Symposium (International) on Combustion
The Combustion Institute, Pittsburgh (1973) p.627

55. Grout, P.D.
"Combustion of Residual Fuel Oil: Modelling and Optimization of a Two Stage System."
Ph.D. Thesis, University of London (1970)

56. Marteney, P.J.
"Analytical study of the kinetics of formation of nitric oxide in hydrocarbon-air combustion."
Combust. Sci. & Technol., 1, (1970) 461

57. Bowman, C.T.
"Kinetics of nitric oxide formation in combustion processes."
Fourteenth Symposium (International) on Combustion
The Combustion Institute, Pittsburgh (1973) p.729

58. Lavoie, G.A., Heywood, J.B. and Keck, J.C.
"Experimental and theoretical study of nitric oxide formation in internal combustion engines."
Combust. Sci. & Technol., 1 (1970) 313

59. Appleton, J.B. and Heywood, J.B.
"The effects of imperfect fuel-air mixing in a burner on NO formation from nitrogen in the air and fuel."
Fourteenth Symposium (International) on Combustion
The Combustion Institute, Pittsburgh (1973) p.777

60. Fletcher, R.S.
"The prediction of nitric oxide formation in combustion systems."
Combustion Institute European Symposium, ed. F.J. Weinberg.
Academic Press (1973) p.445

61. Malte, P.C. and Pratt, D.T.
The role of energy releasing kinetics in NO_x formation: fuel lean, jet stirred CO-air combustion."
Combust. Sci. & Technol., To be published (1975)

62. Caretto, L.S.
"Modelling pollutant formation in combustion processes."
Fourteenth Symposium (International) on Combustion.
The Combustion Institute, Pittsburgh (1973) p.803

63. Bragg, S.L.
"Application of reaction rate theory to combustion chamber analysis."
Aeronautical Research Council 16170, CF272 (September 1953)

64. De Zubay, E.A.
"A comparative investigation of a homogeneous combustion chamber with a two stage combustion chamber."
Jet Propulsion, 26 (1956) 77

65. Hardcastle, J.W.
"A theoretical analysis of multi-stage reaction rate controlled systems."
Seventh Symposium (International) on Combustion
The Combustion Institute, Pittsburgh (1959) p.697

66. Beer, J.M. and Lee, K.B.
"The effect of residence time distribution on the performance and efficiency of combustors."
Tenth Symposium (International) on Combustion
The Combustion Institute, Pittsburgh (1965) p.1187

67. Vulis, L.A.
"Thermal Regimes of Combustion."
McGraw Hill, N.Y. (1961)

68. Priem, R.J. and Heidmann, M.F.
"Propellant Vaporization as a Design Criterion for Rocket Engine Combustion Chambers."
NASA TR R-67 (1960)

69. Spalding, D.B.
"A one-dimensional theory of liquid fuel rocket combustion."
Aeronautical Research Council 20175 CP. No.445 (1958)

70. Williams, F.A.
"Spray combustion theory."
Combust. & Flame, 3 (1959) 215

71. Nuruzzaman, A.S.M., Siddall, R.G. and Beer, J.M.
"The use of a simplified mathematical model for prediction of burn out of non-uniform sprays."
Chem. Engng. Sci., 26 (1971) 1635

72. Courtney, W.G.
"Combustion intensity in a heterogeneous stirred reactor."
American Rocket Soc. J., 30 (1960) 357

73. Mellor, A.M.
"Current kinetic modelling techniques for continuous flow combustors."
'Symposium on Emissions from Continuous Combustion Systems.'
Eds. W. Cornelius and W.G. Agnew. Plenum Press, N.Y. (1972). pp.23-53.

74. Odgers, J.
"Current theories of combustion within gas turbine chambers."
Fifteenth Symposium (International) on Combustion.
The Combustion Institute, Pittsburgh (1975). p.1381

75. Burgoyne, J.H. and Cohen, L.
"The effect of drop size on flame propagation in liquid aerosols."
Proc. Roy. Soc. 'A', 225 (1954) 375

76. Pratt, D.T.
"PSR - A computer program for calculation of steady flow, homogeneous combustion reaction kinetics."
Bulletin 336, Engineering Extension Service, Washington State University, Pullman, Washington, 99163 (1974)

77. Jones, A. and Prothero, A.
"The solution of the steady state equations for an adiabatic stirred reactor."
Combust. & Flame, 12 (1968) 457

78. Gordon, S. and McBride, B.J.
"A Computer Program for Calculation of Complex Chemical Equilibrium Compositions, Rocket Performance, Incident Shocks and Chapman Jouget Detonations." NASA SP-273 (1971)

79. Treleaven, C.R. and Tobgy, A.H.
"Conversion in reactors having separate reactant feed streams. The state of maximum mixedness."
Chem. Engng. Sci., 26 (1971) 1259

80. Schefer, R.W., McLean, W.J. and Sawyer, R.F.
"Dispersion in combustion gas sampling probes."
Combust. & Flame, 19 (1972) 267

81. Lewis, J.D.
"A Proposed Method for Continuously Recording Mixture Ratio in HC-O_2 Combustion Systems."
Rocket Propulsion Establishment, Tech. Memo No.180 (1959)

82. Aldridge, R.H.
Private Communication.
C.A.V. Ltd., Acton, London

83. Pratley, G., Swanton, W.T. and Whyman, B.H.F.
"The Design, Construction and Performance of a High Speed Sampling Valve for Engine Studies. Part 2."
B.P. Research Centre, Sunbury on Thames, Middlesex.
Report No. 10141 (s) 14/2/1967

84. Garner, F.H., Grigg, G.H., Morton, F. and Reid, W.D.
"Pre-flame reactions in diesel engines."
J. Inst. Petrol., 42 (1956) 69

85. Dushman, S.
"Scientific Foundations of Vacuum Technique."
John Wiley and Sons, Inc., N.Y. Second edition. 1966

86. Honig, R.E.
"Gas flow in the mass spectrometer."
J. Appl. Phys., 16 (1945) 646

87. Zemany, P.D.
"Free molecular flow in the sample inlet to the mass spectrometer."
J. Appl. Phys., 23 (1952) 924

88. Anon.
"Metrosil in glass porous plug leaks."
Technical Information Sheet V48, AEI Limited, Manchester.
July 1966

89. Gibilaro, L.G. and Drinkenburg, A.A.H.
"Numerical evaluation of mean and variance from the Laplace transform."
Chem. Engng. Sci., 27 (1972) 444

90. Pratt, D.T., Bowman, B.R., Robertus, R.J. and Crowe, C.T.
"Comparison of homogeneous gas-phase reaction kinetics for complete segregation and complete micromixing."
Paper WSCI 72-6, Western Section/ The Combustion Institute. (1972)

91. Baulch, D.L., Drysdale, D.D., Home, G.G. and Lloyd, A.C.
"Critical Evaluation of Rate Data for Homogeneous Gas Phase Reactions of Interest in High Temperature Systems. Part 4."
Department of Chemistry, The University, Leeds. December 1969

92. Heywood, J.B. and Mikus T.
"Parameters controlling nitric oxide emissions from gas turbine combustors."
AGARD Conference Proceedings, No.125, paper 21 (1973)